SYNTHESIS AND CHARACTERISATION OF HOLLOW MONODISPERSE SILICA-TITANIA NANOSTRUCTURES FOR POTENTIAL USE IN TARGETED DELIVERY OF DRUGS/VACCINES/GENES

MD REDUANUL HOSSAIN

A thesis submitted in partial fulfilment of the requirements
of the University of Greenwich for the Degree of Master of
Philosophy

October 2016

DECLARATION

"I certify that this work has not been accepted in substance for any degree, and is not concurrently being submitted for any degree other than that of Master of Philosophy being studied at the University of Greenwich. I also declare that this work is the result of my own investigations except where otherwise identified by references and that I have not plagiarised the work of others".

Candidate's Name : Md Reduanul Hossain

Signature : __________________________

Date : __________________________

First Supervisor : Professor Peter Charles Griffiths

Signature : __________________________

Date : __________________________

Second Supervisor : Dr Simon Richardson

Signature : __________________________

Date : __________________________

ACKNOWLEDGEMENTS

First of all, I would like to express my sincere gratitude to my supervisor Professor Peter Griffiths for his endless support and guidance throughout my research journey. His insights into and patient endurance throughout this project have been a true blessing. I would also like to thank him for his quality research training and for introducing me to the research world.

I am especially grateful to Dr Bruce Alexander for his suggestion and help in the lab with his expert solution and for training me in the several instruments.

I would like to convey my gratitude to Professor David Wray for his training in BET instrument and help in surface area measurements.

I am very much thankful to Dr Ian Slipper and Andrew Hutt for their continuous help in SEM lab. I am really grateful to Dr Slipper, who did not stop helping me even at his serious medical condition.

I am also thankful to my fun loving research group (Beatrice, Omar, Marvet, Leesa) for making me enjoy every moment we spent together in research office. I especially want to thank Dr Beatrice Cattoz and Dr Omar for their valuable suggestions and technical advice throughout my project.

I would like to thank my university colleagues, friends, housemate and well-wishers for their support and advice.

Finally I very much grateful to my parents and other family members for their support and encouragements for pulling me up to this stage of life.

ABSTRACT

In recent years, there has been a continuous growth in pharmaceutical formulations based on nanoparticle technology. Although a large number of nanocarriers have been studied, most of them are limited by their ability to carry sufficiently viable therapeutic loads, toxicity, and target specific delivery etc. There is, therefore, an urgent need to develop novel, smart nanocarriers which avoid the above limitations. Hollow nanoparticles with their hollow cavity and favourable surface modification, offer a great deal of promise in drug delivery applications. However, a good understanding and thorough characterisation of these nanoparticulate systems is crucial.

In this thesis, (solid) silica nanoparticles, silica-titania core-shell nanoparticles (STCSNP) and silica-titania hollow nanoparticles (STHNP) were synthesized using literature procedures. A series of analytical techniques were used to characterize the three different nanoparticles, including dynamic light scattering, scanning transmission electron microscopy, nitrogen physisorption, energy dispersive X-ray spectroscopy and X-ray diffraction technique. Furthermore, the stabilization and purification of these nanoparticle dispersions were carried out using two different procedures (dialysis and centrifugation). Dialysis was found to be the more sophisticated procedure for the purification of these nanoparticle dispersions, *i.e.* without inducing aggregation.

This thesis also demonstrates the versatility of solvent relaxation NMR to study silica-titania hollow nanoparticles (STHNP), along with the bare silica nanoparticles and silica-titania core-shell nanoparticles (STCSNP). The possibility of conducting porosity measurements on complex structures like mesoporous hollow nanoparticles by NMR spectroscopy was explored. NMR spectroscopy was sensitive to both the inner and outer surfaces of the hollow nanoparticles, with some sensitivity to STHNP, as well as from the transition metal (titania) present. Two relaxation rates for water were observed at low concentrations for the hollow nanoparticles, which disappeared at higher particle concentration. However, only single exponential decay curves were observed for the solid nanoparticles (silica nanoparticles and core-shell nanoparticles) as expected.

Polymers are common excipients in pharmaceutical formulations, especially in nanoparticulate systems for establishing steric stability. Relaxation NMR experiments along with light scattering, revealed interactions between polymer at titania and silica-titania mixed interfaces. In this study, poly(vinyl pyrrolidone) (PVP) was used to investigate the polymer-particle interaction using solvent relaxation NMR spectroscopy. PVP was observed to adsorb on the silica nanoparticle surfaces however, only poor adsorption was observed on the pure titania (core-shell nanoparticles) and silica-titania mixed surfaces.

CONTENTS

List OF FIGURES

LIST OF TABLES

Aims

The aims of this project are to synthesize monodisperse hollow silica-titania nanoparticles with controllable sizes and characterizing the hollow nanoparticles to understand their potential as a drug delivery system, mainly by solvent relaxation NMR. The aims also include the quantification of shell porosity of hollow nanoparticles upon polymer adsorption.

Project overview

The first chapter of this thesis provides a general overview of nanotechnology pertaining to drug delivery applications and evaluates the potential for hollow nanoparticles as a drug delivery vehicle.

The second chapter describes the overall synthesis process and characterization of silica nanoparticles, silica-titania core-shell nanoparticles and silica-titania hollow nanoparticles. This chapter also discusses the formation of core-shell nanoparticles and hollow nanoparticles and describes the characterization used to study the morphology of hollow nanoparticles.

The third chapter describes the adsorption of polyvinylpyrrolidone (PVP) on the silica surface, the titania surface and the silica-titania mixed surface of silica nanoparticles, silica-titania core-shell nanoparticles and silica-titania hollow nanoparticles respectively. Two different techniques were used to study the adsorption behavior of polymer on three different surfaces. Solvent relaxation nuclear magnetic resonance spectroscopy measured the polymer train concentration on particle surfaces, and dynamic light scattering technique provided the size of the polymer-particle system.

Chapter four contains general conclusions and recommendation for future work.

Chapter-1:

Introduction

1.1 Drug Delivery Systems

Drug delivery systems embody the engineered process and structures for formulating and carrying drugs, pharmaceuticals or other biomolecules to the expected site of action and therby exerting pharmacological effects that achieve desired therapeutic goals. In this case, pharmacokinetics and pharmacodynamics are the main factors to be considered when delivering the drug [1] [2].

In the human race, drugs have been used for a long time to improve the quality and prolong life. But delivering drugs with severe side effects or other therapeutics, especially protein- and gene-based drugs, to the body have been the single hardest obstacle to clinical translation of these therapeutics [3]. In the past few decades, the practice of drug delivery has improved markedly but much more significant improvements are needed. Biomedical and chemical engineers have contributed considerably to drug delivery system development, not only limited to understanding physiological barriers to effective drug delivery (transportation of drug through circulatory systems, drugs penetration through cells and tissues) but also efforts to design different types of smart delivery vehicles. However, with all of this progress, most of the drugs, even those found utilizing most progressive molecular biology strategies, possess undesirable adverse effects and systemic toxicity. There are several factors that contribute to these physiological effects and limit the drug efficiency, however, most of those factors can be attributed to the pharmacodynamics and pharmacokinetics characteristics of the drugs or biomolecules. These factors can be listed as an off-target activity that lower the therapeutic index, the hydrophobicity of drugs that causes low aqueous solubility, and more include unwanted tissue accumulation, rapid clearance, and widespread metabolism of drugs [4]. These unacceptable effects of drugs constrain our capability to treat several life-threatening diseases, for example, cancer, neurodegenerative disease, and other infectious diseases.

Drug delivery systems improve the delivery of the drug through two fundamental mechanisms without causing unwanted toxicity to the body: either by controlling the release rate of the drug in a desired manner and/or by providing the target-specific drug release action to the body [5] [6] [7] [8]. Target-specific drug delivery is a well-known therapeutic approach which refers to specific delivery of small drug molecules or therapeutic biomolecules (gene, protein) to the target of interest based on the establishment of nanoscale devices or other reliable platforms [9] [10] [11]. Although different molecular strategies for developing such delivery systems have been established, the utilization of nanostructures or nanometer sized vehicles is the most common form to achieve target specific drug delivery into the body. But extent of success of such nanotherapeutic delivery strategies are dependent on the combination of three crucial physiological processes, where the steps are: a) target specific binding of cell surface receptors and ligands of nanocarriers, b) cell penetration of drug-loaded nanomaterials by targeted cells, c) realising active form of drugs in controlled manner [12] [13]. And to achieve these goals, a smart technology of delivery strategy is crucial which is not only compatible with the drug molecules but also provides biocompatibility to the physiological barrier of the body. Nanotechnology for drug delivery applications offers a great collection of uniquely suited delivery approaches for improving the therapeutic profiles of currently available potential drugs especially chemotherapeutic agents [14].

1.2 Nanotechnology in Drug Delivery Systems

The applications of nanotechnology in the field of drug delivery system is widely expected to change the scenario of pharmaceutical and biotechnology industries. Literally, nanotechnology refers to the functional systems that engineered at the molecular level. Such systems involve different interdisciplinary fields ranging from materials science to biomedicine and characterization of such system is based on their characteristic physical, chemical, optical and electronic properties. One of the vital research fields of nanotechnology is nanomedicine where nanotechnology is applied to design methodology for the prophylaxis, diagnosis, and treatment of diseases [15] [16]. There are a considerable amount of research have been attributed in nanomedicine during few decades. Most of them are now translating into the commercial products in the global market and more products are still in pipeline. Nowadays, nanomedicine is extensively dominated by drug delivery systems and according to the US National Science Foundation, around $1 trillion of product sale has been achieved [17]. In term of size, nanomaterials used in the drug delivery applications are similar to protein and other macromolecular structure found inside the body living cells. And such nanomaterials are well balanced to promote the delivery of drugs by taking the advantages of existing cellular components. When the drugs are encapsulated, dispersed, absorbed or conjugated with the nanoparticles (NPs), NPs with their unique properties, can sustain excellent performance of the drugs in a variety of dosage forms. In addition, such nanoparticulate formulations facilitate the smooth interaction of the drug with the biological system and also offer excellent stability, solubility, rapid dissolution of drugs which finally accelerate the improved onset of action and bioavailability. Furthermore, due to their highly functional surface, nanostructures increase the loading and target specific delivery of cargos (therapeutic drugs, proteins, and genetic materials). And it is possible to tune the NPs surface with ligands, such as an antibody, folic acid, peptides. This conjugation of the ligands with nanoparticles provides both active and passive drug targeting into the body organelles and reduce the drug dose needed to achieve desired therapeutic goals. Thus create the scope of highly efficient delivery of the drug, which, in turn, would lower the cost and/or reduce the side effects.

Implementation of new developing drug delivery system is a demand of time for expansion of global drug markets. Such a plan would be applied to nanotechnology therapeutic products that validate the improvement of previously approved drugs. Furthermore, nanotechnology creates a scope for academics and industrial investigators to revisit the pharmaceutically suboptimal but biologically active new molecular entities those were previously banned or rejected for their unfavourable bio-physicochemical properties when formulated through conventional approaches. And it is expected that the ability of nanotechnology can be increased to develop and commercialize the new class of bioactive macromolecular species (siRNA or microRNA) those facilitate the RNA interference pathways and require an accurate intracellular delivery strategy for providing therapeutic actions [9] [18]. However, all of these approaches will not mount in successful platform until the targeted delivery theory come in reality. Most of the clinically approved nanotechnology products are suffering from poor active targeting or triggered drug release manner. Scientists are exploring the possible successful ways and narrated three key points need to come in consideration: A) selection of biocompatible drug delivery vehicles that optimum for the product development B) Drug itself, that possesses compatible bio-physicochemical properties for the active targeting C) Selection of diseases and indications for which targeted delivery systems to be designed [9]. With the recent scientific advances and correct combination of these three components, significant improvement of targeted drug delivery system in nanotechnology platform is expected to be substantial. In past recent years, the pace of scientific discovery in the field of nanotechnology has gained considerable thrust. Recently, Li Liu *et al* synthesized polymeric NPs based on the amphiphilic and biodegradable ternary copolymer conjugated with folate for efficient and tumour specific siRNA delivery in cancer treatment [19]. In near future, it is foreseeable that emergence of nanotechnology will likely to have a significant impact on drug delivery applications.

1.3 Nanocarriers as Drug Delivery Systems

Nanosized structures can be formed as several shapes which include the spherical nanoparticles, nanotubes, and nanorods. They can function as versatile nanocarrier platforms that have a potential usage and also well known for their novel properties. They have been extensively analysed as a target specific delivery vehicles for therapeutics and diagnostic aids in outlining the cancer treatment, as well as other inflammatory and infectious diseases [20] [21]. In present studies, different classes of such nanocarriers have been stated in the literature which includes inorganic-based nanoparticles (NPs) such as silica NPs, gold NPs, iron oxide NPs, and nanotube (carbon nanotubes); organic-based NPs such as a dendrimer, liposome and polymer-based NPs such as micelles, PLGA NPs [12].

The physicochemical characteristics of these nanocarriers are unique from each other in terms of their size, shape, synthesis procedure, surface functionality and modification, core-shell structure and hollow architecture. In the development of drug delivery vehicles based on these nanostructures, it is important to understand their physicochemical properties as well as their interactions with the body physiological systems, as a small number of these nanocarriers have been proved to cause severe intrinsic toxicities or immunogenicities to the body [22] [23]. For instance, a nanoparticle with cationic surfaces has shown cytotoxicity as they cause disruption of cellular membranes [24]. However, this kind of unwanted effects could be masked by modifying the surface functionality of cationic nanoparticles which is also an important fact to bear in mind when developing drug delivery systems. Thus the diverse approaches are necessary when designing drug delivery vehicles [12].

However, in terms of interaction with the body physiological systems, nanocarriers with the elevated bio-physicochemical properties can penetrate through cells more easily than the larger molecules. This size-dependent advantage made the nanocarriers as a successful delivery tool for the currently available therapeutics compounds. The strategy of drug conjugation with nanocarriers and their targeting is extremely important fact for a targeted therapy. When added, a drug usually adsorbed or attached through the covalent link at the nanostructure surfaces or in some cases encapsulated into it. Covalent linking is more favourable than other ways of attachment since it involves controlling the number of drug molecules conjugated to nanostructure surfaces. Furthermore, intracellular targeting strategies of nanotechnology therapeutics can be categorized into the active or passive mechanism. Active targeting depends on extravasation of the drug within the target tissues which involves the conjugation of nanocarriers with the target of action by using appropriate ligands. The active mechanism also accomplished by tuning the physical properties (e.g. temperature, pH). On the other hand, passive targeting relies on the enhanced permeability and retention effect (EPR) caused by the vascularization of the leaky vasculature and poor lymphatic drainage which is the characteristics of solid tumors. The EPR effect is a unique phenomenon where nanocarriers tend to extravasate passively from the blood flow to tumors rather than the healthy tissues. After the successful transport of nanocarrier-conjugates to the target tissues, it releases its therapeutic cargo. It is also possible to achieve the controlled release of therapeutics through engineered approaches, where nanocarrier release it's cargo only when subjected to the changes of the physiological environment such as temperature, pH, osmolality, or via an enzymatic activity. However, passive targeting is a totally coincidental process where targeting approaches depend on the defective blood vessels, additionally defective lymphatic drainage. Therefore, active targeting has been the main focus in the drug delivery field since it facilitates the targeting in molecular level.

1.3.1 Virus- like particles

Virus-like particle (VLP) is multi-protein nanostructure that resembles virus but non-infectious, ranging from 0.1 nm to 100nm in the spatial dimension. They are self-assembled virus mimicking nanostructures constructed during expression of viral structural proteins, such as envelop or capsid. VLPs are excellent cargo, they can transport not only protein/peptides or other therapeutic agents but also possess the ability to encapsulate or attach genetic materials and thus can be used as delivery systems for gene and therapeutics [25]. Due to their favourable EPR effect, it has been shown *in vitro* that they can effectively target and accumulate into the cancer cells [26]. Bacteriophage MS2 is a self-assembled VLPs with a nucleic acid which has been experimented in the delivery of selective chemotherapeutic agents, siRNA mixtures, and protein toxins to human hepatocellular carcinoma (HCC). Upon modification with the SP94 peptides, VLPs have shown outstanding results in targeting these particular cells and delivering their loads [27]. VLPs formulated with doxorubicin, cisplatin, and 5-fluorouracil have found to eradicate the Hep3B cells, a HCC cell line. VLP is also found to deliver siRNA cocktail, which suppresses the expression of cyclin and facilitates the inhibition of growth and apoptosis of Hep3B cells. There are lots of such results have been discussed in the literature to prove the VLPs are superb nanocarriers for encapsulating a variety of cargos but it needs to be stated that none of those experiment conducted *in vivo*. A few numbers of oncolytic viruses have been studied in clinical trials over last few years but none of those has reached in the commercial market. Recently, VLPs are being used in the treatment of hepatitis, HIV, rotavirus infection and improving the bioavailability of several antibiotics used for cancer treatment [28]. The main drawbacks associated with VLPs drug delivery systems include biosafety and cytocompatibility concerns.

1.3.2 Organic Platform

Organic nano cargos include a wide variety of natural and synthetic composites delegated for targeted or non-targeted delivery of drugs. They can be broadly categorized into drug conjugates, lipid-based carriers, protein carriers, polymer carriers. Although drug conjugates made their way towards successful clinical efforts, only tentative progress have achieved to develop nanocarriers based on lipids, proteins, or polymers into clinical practice.

1.3.2.1 Drug-conjugate

At present time, drug conjugates have been the most successful nanomedicine therapeutics in clinical practice specifically in cancer care. They can be described as a nanotherapeutics due to their formulation with the active pharmaceutical ingredients in nanosized range. The therapeutics are usually linked through a covalent bond with targeted antibodies, peptides or polymers to synthesize mono- or oligomeric drug conjugates. The conjugates improve the target specific drug delivery without influencing the physicochemical properties of the drugs. In contrary, nanocarriers based on other organic platforms as well as the inorganic compounds usually encapsulate the drugs where they don’t need to link with drugs covalently. Antibody-drug conjugates such as trastuzumab-emtansine and brentuximab-vedotin have been proved to be effective against the HER2-overexpressing breast cancer and CD30-positive Hodgkin lymphoma, anaplastic large-cell lymphoma respectively [29] [30]. Several other antibody-drug conjugates are in clinical trials and more advanced research is going on toward the designing multi-structural next generation antibody-drug conjugates for drug delivery applications [29].

Another potential group of nanocarrier systems (ranging from 5-20nm) for drug delivery is the polymer-drug conjugate which acquires the ability to improve the pharmacokinetic profile of drugs [31]. They can effectively accumulate in the tumor sites through EPR effect. More than 15 anticancer conjugates are in research pipeline for their clinical development based on the polymer-drug conjugates strategy. Although there is a broad selection of novel drug targets and tunable advanced chemistry exists, only a few polymers and drugs have been used to develop drug-conjugates. The HPMA copolymer-doxorubicin conjugate PK1 is an excellent example of a novel anti-cancer agent having less cardiotoxicity and alopecia than those are acquired by free doxorubicin. In addition, several more commercial products are in pipeline waiting for their clinical trials, e.g., PGA-PTX (Xyotax™, CT-2103; Cell Therapeutics Inc. /Chugai Pharmaceutical Co. Ltd.), PGA-camptothecin (CT2106; Cell Therapeutics Inc.) [18]. However, the polymer-drug conjugates based nanocarriers remain the model of excellence in the field of drug delivery, they are restricted by their non-biodegradability and ultimate outcome of polymers after *in vivo* studies.

1.3.2.2 Polymeric nanoparticles (NPs)

Polymeric NPs are the colloidal dispersion of particles with a diameter ranging from 10-1000 nm. They have been synthesized from a variety of synthetic and natural polymers, such as polylactide–polyglycolide copolymers, polyacrylates and polycaprolactones, albumin, gelatin, alginate, collagen and chitosan [32]. Drugs can be attached on the surface or encapsulated into the structure by the polymerization reaction. In anticancer therapy, they can be used as a cargo to release the therapeutics either by diffusion, desorption or degradation of NPs in the vicinity of target tissues. Furthermore, they can be used as a parenteral drug delivery system to carry the therapeutic agents to bone marrow, spleen, and liver [33]. Upon modification of their surfaces, polymeric NPs can deliver the drug by both passive and active targeting to the tumour cells. They are also applied in radiotherapy or diagnostic purpose and can be served as stimuli-responsive drug delivery systems. In general, a successful drug delivery system requires the safe elimination from the body after completing its desired mission. Therefore most of the drug delivery systems are developed from the biodegradable natural or synthetic macromolecules. It is well-known that the first biodegradable NPs were synthesized from the natural polymer followed by the application of synthetic polymers, e.g., poly(alkyl cyanoacrylate) or poly(orthoester) [34]. Many hydrophobic drugs, including taxols, doxorubicin, rapamycin, or camptothecin formulated with the biodegradable polymers (albumin, polyethylene glycol, poly(lactic-co-glycolic acid)), have been reached in clinical trials. Furthermore, more sophisticated nanoparticulate system are in pipeline for preclinical evaluation or under development for the *in vivo* studies [35].

1.3.2.3 Lipid-based nanocarriers

Liposome was the first lipid-based nanocarrier employed as a drug delivery system. They are artificial vesicles developed from the self-assembly of phospholipids and steroids in nanoscale confinements ranging from 50-300nm size. The vesicles are basically composed of spherical lipid bilayer surrounding an aqueous core domain. This lipid bilayer is the mimics the features those found in the biological membranes. Liposomes are the most clinically established nanocarriers for their rich biological properties which include biocompatibility, biodegradability, and ability to carry both hydrophobic and hydrophilic drugs. Their efficiency has already been reported in improving bio-physicochemical properties of several drugs [36] [37]. Furthermore, a number of successful liposomal products are already in the market owing higher efficacy and lower toxicity, e.g. AmBisome® Doxil®, Daunoxome®, Depocyt®, used for cancer and Lymphomatous meningitis treatment [37]. Recently specially modified liposomes called stealth liposomes, have been experimented to show excellent pharmacokinetics profiles in the delivery of genetic drugs for gene therapy applications [38]. However, liposomes are also suffering from some limitations which include low cargo efficiency, the unfavourable release of drug in extracellular fluid, instability during storage and lack of tunable triggers for drug release. As such, to overcome these limitations many efforts are being devoted to improving their bio-physicochemical properties [36].

Solid-lipid nanoparticles (SLN) are nanosized carrier synthesized from a cocktail of solid and lipid matrix, surfactants, and water/solvents. Lipids used in SLN synthesis are usually highly purified triglycerides, complex glycerides mixture or waxes stabilized with surfactants [39]. They have been used for the drug delivery applications through several routes, such as parenteral, pulmonary, peroral, dermal, ocular and rectal [40]. The main advantages of SLN comprise the good stability, controlled drug release profile, good tolerability, and defence of encapsulated drugs against degradation. However, conventional SLN is not free from drawbacks which include the low drug loading capacity due to limited solubility of the drugs in the solid lipid and their unfavourable structure and polymorphic states, crystallization followed by drug expulsion and reasonably high water content of the system [41]. Therefore, a few smart SLN systems have been come in front side to minimize these disadvantages, for example, nanostructured lipid carriers (NLC) and lipid drug conjugates (LDC) which are literally the modification of lipid-based nanoparticles. NLC are synthesized by mixing solid and liquid lipids owing increased capacity of carrying therapeutic cargos and disallowed the drug expulsion [42]. And LDC are insoluble drug-lipid conjugates and prepared by homogenisation of lipid matrix, drug, and surfactants through the formation of salt or covalent binding. LDC offer a lipid-based carrier for lipophobic drug molecules with increased applicability [43].

1.3.3 Inorganic platforms

Inorganic-based nanoparticles have achieved massive attraction on their various applications in the field of drug delivery, or radiotherapy and active tumour targeting [44]. A variety of inorganic nanostructure is being developed as excellent drug vehicles based on their favourable nanostructure construction, tunable properties, and controlled drug-release profiles. Furthermore, nanosized inorganic drug vehicles have shown superb compatibility and sustained release profiles of hydrophobic drugs and in addition to DNA, RNA and protein therapeutics [45]. Functional inorganic nanostructures with mesoporosity, distinctive size, shape, and composition-dependent physicochemical properties exhibit luminescent, magnetic, and excellent surface properties. And these unique features lift up them as attractive materials for delivery of drug and therapeutics and for diagnostics applications. Super-paramagnetic iron oxide nanoparticles are generally used for diagnostic applications and some iron oxide formulations have been studied in the clinical stage for

MRI (magnetic resonance imaging) testing of tumours. NanoTherm® is a ferrofluid- an aqueous colloidal dispersion of iron oxide nanoparticles that reacts with the presence of magnetic field. When administered into the tumour, NanoTherm® therapy kill, sensitize or disable tumor cells through hypothermia and thermoablation processes depending on the duration and temperature. The pioneer studies with NanoTherm® have shown robust results against glioblastoma, the most frequent and malignant of brain tumours [46]. This inorganic based nanomedicine has acquired remarkable attention in the European countries.

Recently, hafnium oxide nanoparticle has entered in clinical trials. This nanoparticle has experimented as a radiosensitizer in patients with soft tissue sarcoma [47]. Although there is a great possibility exist, but no inorganic nanocarriers have gained therapeutic approval. Some of them are still facing initial clinical trials, such as silica nano-vehicles for peptide delivery [48] and pegylated-gold nanoparticles in cancer treatment [49].

1.4 Hollow Nanoparticles as Drug Delivery Systems

Hollow nanoparticles are the novel class of engineered nano-architectures with void space inside the shell and/or porous shell structure, excellent applicants for drug delivery systems. They have secured their places in both fundamental research and practical applications due to their morphology and physicochemical properties, such as shell porosity, high surface-volume ratio, low density, and low coefficients of thermal expansion. Hollow nanoparticles with different chemistry have been synthesized and applied for drug delivery vehicles, for example, hollow mesoporous silica, hollow polymeric nanostructures, and yolk-shell hollow nanoparticles. These hollow nanostructures have shown their efficiency in loading several antibiotics and chemotherapeutic agents. Several other hollow nanocarriers, for example, hollow magnetite shells, hollow carbon shells, polymer capsules, are stated to be a proper carrier for loading and releasing enzymes, proteins, or DNA, and other small molecules. Hollow liposomes, [50] hollow DNA assembly, [51] hollow manganese oxide [52] have also come in the frontline as delivery carriers of siRNA. Recent studies have highlighted the advances in biomedical applications of hollow iron oxide and gold nanoparticles in terms of drug delivery and hyperthermia cancer therapy [53] [54].

1.5 Necessity of Hollow Nanoparticles as Drug Delivery Systems

The application of nanomaterials in diagnostic or therapeutics fields can be termed as nanomedicine which has extended rapidly in recent decades. For nanomedicine applications, accuracy and precision are crucial in designing and synthesis of nanosized architecture. Particularly, multifunctional drug delivery (MDD) systems with their versatile functionality have received massive attraction for diagnosis and treatment of several infectious diseases. These multifunctional delivery systems facilitate the target and treatment specificity of drugs through non-invasive particle accumulation at tumour sites. MDD systems can incorporate two or more components and hence, can provide an important strategy to understand the full potential of the next-generation therapeutics [55]. Hollow nanoparticles with their favourable interior architecture can be employed to design these MDD systems with different chemistry depending on the bio-physicochemical properties of the therapeutics. Recently J. Lee *et al* fabricated double-shelled hollow nanostructures based on the silica-titania composites which shows the possibility of designing MDD systems for delivery of several therapeutics at a time [56].

Furthermore, scientists have identified one of the major hindrances in cancer chemotherapy is the multidrug resistance or simply MDR. And several studies have been done to overcome this problem, for example, delivery of siRNA with anticancer drugs [57] to knock down the protein (P-glycoprotein, Bcl-2) responsible for MDR in cancer cells [58]. Hence, the drug-gene co-delivery has been the promising research topic in improving the cancer treatment. To facilitate this drug delivery strategy, the demand of an excellent and efficient nanocarrier has gradually increased. Earlier, Mesoporous silica nanoparticles (MSNPs) has come in the frontline for their intrinsic bio-physicochemical properties, such as high surface area, tunable particle size, large pore volume and ease of surface modification, for favouring the drug loading and gene attachment [59]. Although MSNPs has shown their biocompatibility with less toxicity, but their dosage- dependent toxic effects are now major safety issues in biological systems [60]. Thus, it will be great efforts if it is possible to increase the MSNPs capacity in the delivery of drug-gene conjugates, in other words, if a small amount of silica nanoparticles would be enough to deliver an efficient amount of therapeutics for achieving desired therapeutic actions with less toxicity. Here, hollowing the MSNPs would be the great alternative to address this challenge since they have got void cores that could carry the extra load of drug storage [61]. Subsequently, the hollow carrier provides the highly porous shell with a higher surface area for gene attachments compare to the same amount of bare silica used. As a result, the hollow nanostructure can offer enhanced delivery of genetic materials. Xing Ma *et al* designed and fabricated the pH-responsive hollow nanocarriers for co-delivery of doxorubicin-siRNA where folic acid conjugates were utilized for targeted and controlled intracellular delivery of drug-gene conjugates. According to their findings, these multifunctional delivery systems improve not only efficient loading of drugs with less toxicity but also enhance siRNA ability to bind with the tumour cells [62].

With the supports of recent scientific and technological advances, scientists are dedicating their efforts and knowledge in discovering new opportunities in drug delivery field. For example, researchers are looking for alternative treatment strategies to conventional cancer chemotherapy, for example, photodynamic therapy (PDT). PDT employs light-sensitive dyes termed as a photosensitizer which is sensitive to the specific wavelength of light and produces free radicals to facilitate the cell deaths at tumour sites [63]. Hollow nanoparticles could be the excellent carrier of photosensitizer for their large cavity that can carry the efficient amount of photosensitive dyes. Moreover, due to their higher mesoporosity, visible light can easily enter through the hollow nanoparticles thus can sensitize the photosensitizer inside the hollow cavity and can cause tumour cell death. Y. Jang *et al* utilized the folic acid conjugated hollow silica-titania nanoparticles to encapsulate Protoporphyrin IX inside the hollow cavity. They carried *in vitro* studies against human breast cancer cells where they found the hollow nanoparticles could be the new platform for PDT in cancer treatment [64].

1.6 Conclusion

Nanomedicine is denoted as one of the promising research areas and employed as an excellent platform for the drug delivery systems. Several nanomedicine platforms have been identified and extensively researched for biomedical applications. All of them possess both advantages and disadvantages in terms of their bio-physicochemical characteristics. Among them, hollow nano-architectures have been able to draw the attention of researchers in the drug delivery applications for their fascinating properties, ability to carry a wide range of drugs, for designing multifunctional drug delivery systems to avoid multidrug resistance and achieving the target specific delivery. Since it is a new nano-platform for delivery of therapeutics, no nanomedicine based on the hollow nanoparticles has come in the market. Although increasing amount of research works are going on with hollow carriers, none of them even reached in clinical phase as well. So, hollow nanoparticles leave a great scope and possibility to researchers in terms of their biomedical applications, especially in the field of drug delivery systems.

Bibliography

[1] "Nature.com, Drug Delivery Definition," [Online]. Available: http://www.nature.com/subjects/drug-delivery. [Accessed 22 07 2016].

[2] "Reference. MD; Drug Delivery System Definition," [Online]. Available: http://www.reference.md/files/D016/mD016503.html. [Accessed 22 07 2016].

[3] E. R. Lorden, H. M. Levinson and K. W. Leong, "Integration of Drug, Protein, and Gene Delivery Systems with Regenerative Medicine," *Drug delivery and translational research,* vol. 5, no. 2, pp. 168-186, 2015, April.

[4] C. M. Taniguchi, S. R. Armstrong, L. C. Green, D. E. Golan and A. H. T. Jr, "Drug Toxicity," in *Principles of pharmacology: the pathophysiologic basis of drug therapy*, Philadelphia, Lippincott Williams & Wilkins, 2008, pp. 63-73.

[5] W. D. Jong and P. Borm, "Drug delivery and nanoparticles: applications and hazards," *International Journal of Nanomedicine,* vol. 3, no. 2, pp. 133-149, 2008.

[6] K. Park and R. J. Mrsny, "Controlled Drug DeliVery: Designing Technologies for the Future," *ACS Symposium Series, American Chemical Society: Washington, DC.,* vol. 752, pp. i-v, 2010.

[7] V. P. Torchilin, "Recent Approaches to Intracellular Delivery of Drugs and DNA and Organelle Targeting," *Annu Rev Biomed Eng,* vol. 8, pp. 343-75, 2006.

[8] N. Larson and G. Hamidreza, "Polymeric Conjugates for Drug Delivery," *Chem. Mater.,* vol. 24, p. 840−853, 2012.

[9] O. C. Farokhzad and R. Langer, "Impact of Nanotechnology on Drug Delivery," *ACS Nano,* vol. 3, no. 1, p. 16−20, 2009.

[10] R. V. J. Chari, "Targeted Cancer Therapy: Conferring Specificityto Cytotoxic Drugs," *Acc. Chem. Res.,* vol. 41, p. 98−107, 2008.

[11] I. Ojima, "Guided molecular missiles for tumor-targeting chemotherapy--case studies using the second-generation taxoids as warheads," *Acc Chem Res.,* vol. 41, no. 1, pp. 108-19, 2008.

[12] P. T. Wong and S. K. Choi, "Mechanisms of Drug Release in Nanotherapeutic Delivery Systems," *Chem. Rev.,* vol. 115, no. 9, p. 3388–3432, 2015.

[13] E. M. M. d. Valle, M. A. Gala´n and R. G. Carbonell, "Drug Delivery Technologies: The Way Forward in the New Decade," *Ind. Eng. Chem. Res.,* vol. 48, p. 2475–2486, 2009.

[14] D. Peer, J. M. Karp, S. Hong, O. C. Farokhzad and R. Margalit, "Nanocarriers as an emerging platform for cancer therapy," *Nat. Nanotechnol.,* vol. 2, no. 12, p. 751−760, 2007.

[15] M. Lobatto, V. Fuster, Z. Fayad and W. Mulder, "Perspectives and opportunities for nanomedicine in the management of atherosclerosis," *Nat. Rev. Drug Discov.,* vol. 10, no. 11, p. 835–852, 2011.

[16] K. Riehemann, S. Schneider, T. Luger, B. Godin, M. Ferrari and H. Fuchs, "Nanomedicine – challenge and perspectives," *Angew. Chem. Int. Ed. Engl.,* vol. 48, no. 5, p. 872–897, 2009.

[17] "Market report on emerging nanotechnology now available," US National Science Foundation, 25 February 2014. [Online]. Available: https://www.nsf.gov/news/news_summ.jsp?cntn_id=130586. [Accessed 03 August 2016].

[18] S. Bamrungsap, Z. Zhao, T. Chen, L. Wang, C. Li, T. Ting and W. Tan, "Nanotechnology in Therapeutics," *Nanomedicine.,* vol. 7, no. 8, pp. 1253-1271, 2012.

[19] L. Liu, M. Zheng, D. Librizzi, T. Renette, M. Merkel and T. Kissel, "Efficient and Tumor Targeted siRNA Delivery by Polyethylenimine-graft-polycaprolactone-block-poly(ethylene glycol)-folate (PEI–PCL–PEG–Fol)," *Mol. Pharmaceutics,* vol. 13, no. 1, p. 134–143, 2016.

[20] P. S. Low, W. A. Henne and D. D. Doorneweerd, "Discovery and Development of Folic-Acid-Based Receptor Targeting for Imaging andTherapy of Cancer and Inflammatory Diseases," *Acc. Chem. Res. ,* vol. 41, pp. 120-129, 2008.

[21] I. J. Majoros, C. R. Williams, B. A. Becker and J. R. J. Baker, "Methotrexate Delivery via Folate Targeted Dendrimer-Based Nanotherapeutic Platform," *Wiley Interdiscip. Rev.: Nanomed. Nanobiotechnol,* vol. 1, p. 502−510, 2009.

[22] A. Sood, S. Salih, D. Roh, L. L. L., M. Parry, B. Hardiman, R. Keehan, R. Grummer, W. E., G. P.J., P. W. Andrews, A. C., F. K., W. M., J. D. Aplin, I. E., P. I., B. M. and L. J., "Signalling of DNA damage and cytokines across cell barriers exposed to nanoparticles depends on barrier thickness," *Nat. Nanotechnol.,* vol. 6, p. 824−833, 2011.

[23] L. A. Mitchell, F. T. Lauer, S. W. Burchiel and J. D. McDonald, "Mechanisms for how inhaled multiwalled carbon nanotubes suppress systemic immune function in mice," *Nat. Nanotechnol.,* vol. 4, pp. 451-456, 2009.

[24] S. Hong, P. R. Leroueil, E. K. Janus, J. L. Peters, M.-M. Kober, M. T. Islam, B. G. Orr, J. R. Baker and M. M. B. Holl, "Interaction of Polycationic Polymers with Supported Lipid Bilayers and Cells: Nanoscale Hole Formation and Enhanced Membrane Permeability," *Bioconjugate Chem.,* vol. 17, pp. 728-734, 2006.

[25] H. Petry, C. Goldmann, O. Ast and W. Lüke, "The use of virus-like particles for gene transfer," *Current Opinion in Molecular Therapeutics,* vol. 5, no. 5, pp. 524-528, 2013.

[26] F. A. Galaway and P. G. Stockley, "MS2 viruslike particles: A robust, semisynthetic targeted drug delivery platform," *Mol. Pharm.,* vol. 10, p. 59–68, 2013.

[27] C. Ashley, E. Carnes, G. Phillips, P. Durfee, M. Buley, C. Lino, D. Padilla, B. Phillips, M. Carter, C. Willman, C. Brinker, J. C. Caldeira, B. Chackerian, W. Wharton and D. Peabody, "Cell-specific delivery of diverse cargos by bacteriophage MS2 virus-like particles," *ACS Nano,* vol. 5, p. 5729–5745. , 2011.

[28] Z. Michał and C. Jadwiga, "Virus-like particles as drug delivery vectors," *Acta Biochim Pol,* vol. 63, pp. 1-5, 2016.

[29] S. Verma, D. Miles, L. Gianni, I. Krop, M. Welslau, J. Baselga and e. al., "Trastuzumabemtansine for HER2-positive advanced breast cancer," *N. Engl. J. Med.,* vol. 367, pp. 1783-1791, 2012.

[30] A. Younes, N. Bartlett, J. Leonard, D. Kennedy, C. Lynch, E. Sievers and e. al, "Brentuximab vedotin (SGN-35) for relapsed CD30-positive lymphomas," *N. Eng lJ. Med. ,* vol. 363, p. 1812–1821, 2010.

[31] N. Larson and H. Ghandehari, "Polymeric Conjugates for Drug Delivery," *Chem. Mater.,* vol. 24, no. 5, p. 840–853, 2012.

[32] J. Panyam and V. Labhasetwar, "Biodegradable nanoparticles for drug and gene delivery to cells and tissue," *Adv. Drug Deliv.Rev.,* vol. 55, p. 329–347, 2003.

[33] H. Hillaireau and P. Couvreur, "Polymeric nanoparticles as drug carriers," in *Polymers in Drug Delivery; Uchegbu, I. F., Schätzlein, A. G., Eds.*, Boca Raton, CRC Press Taylor & Francis Group, 2006, pp. 101, Chapter 8.

[34] U. Karel, H. Kateřina, S. Vladimir, B. Aristides, T. Jiří and Z. Radek, "Targeted Drug Delivery with Polymers and Magnetic Nanoparticles: Covalent and Noncovalent Approaches, Release Control, and Clinical Studies," *Chem. Rev.,* vol. 116, no. 9, p. 5338–5431, 2016.

[35] A. Wicki, D. Witzigmann, V. Balasubramanian and J. Huwyler, "Nanomedicine in cancer therapy: Challenges, opportunities, and clinical applications," *J. Controlled Release,* vol. 200, p. 138−157, 2015.

[36] V. Torchilin, "Recent advances with liposomes as pharmaceutical carriers," *Nat. Rev. Drug Discov.,* vol. 4, p. 145–160, 2005.

[37] T. M. Allen and P. R. Cullis, "Liposomal drug delivery systems: From concept to clinical applications," *Advanced Drug Delivery Reviews ,* vol. 65, p. 36–48, 2013.

[38] S. P. Bhushan, V. V. Chupin and V. P. Torchilin, "New Developments in Liposomal Drug Delivery," *Chem. Rev.,* vol. 115, no. 19, p. 10938–10966, 2015.

[39] A. Kovacevic, S. Savic, G. Vuleta, R. Müller and C. Keck, "Polyhydroxy surfactants for the formulation of lipid nanoparticles (SLN and NLC): Effects on size, physical stability and particle matrix structure," *Int J Pharm,* vol. 406, pp. 163-172, 2011.

[40] A. Z. Wilczewska, K. Niemirowicz, K. H. Markiewicz and H. Car, "Nanoparticles as drug delivery systems," *Pharmacological Reports,* vol. 64, pp. 1020-1037 , 2012.

[41] S. Wissing, O. Kayser and R. Müller, "Solid lipid nanoparticles for parenteral drug delivery," *Adv Drug Deliv Rev,* vol. 56, p. 1257–1272., 2004.

[42] R. Müller, R. Petersen, A. Hommoss and J. Pardeike, "Nanostructured lipid carriers (NLC) in cosmetic dermal products," *Adv Drug Deliv Rev,* vol. 59, p. 522–530, 2007.

[43] R. Müller and C. Keck, "Challenges and solutions for the delivery of biotech drugs – a review of drug nanocrystal technology and lipid nanoparticles. 2004,," *J Biotechnol,* vol. 113, pp. 151-170, 2004.

[44] H.-C. Huang, S. Barua, G. Sharma, S. Dey and K. Rege, "Inorganic nanoparticles for cancer imaging and therapy, 155 (2011)," *J. Control. Release,* vol. 155, p. 344–357, 2011.

[45] J. Guo, L. Bourre, D. Soden, G. O'Sullivan and C. O'Driscol, "Can non-viral technologies knockdown the barriers to siRNA delivery and achieve the next generation of cancer therapeutics," *Biotechnol. Adv. ,* vol. 29, p. 402, 2011.

[46] P. Rivera Gil, D. Hühn, L. L. del Mercato, D. Sasse and P. W. J., "Nanopharmacy: inorganic nanoscale devices as vectors and active compounds," *Pharmacol. Res.,* vol. 62, p. 115–125, 2010.

[47] L. Maggiorella, G. Barouch, C. Devaux, A. Pottier, E. Deutsch and J. Bourhis, "Nanoscale radiotherapy with hafnium oxide nanoparticles," *Future Oncol.,* vol. 8, pp. 1167-1181, 2012.

[48] M. Kovalainen, J. Mönkäre, M. Kaasalainen, J. Riikonen, V.-P. Lehto and J. Salonen, "Development of porous silicon nanocarriers for parenteral peptide delivery," *Mol. Pharm. ,* vol. 10, p. 353–359, 2013.

[49] S. Libutti, G. Paciotti, A. Byrnes, H. Alexander, W. Gannon and M. Walker, "Phase I and pharmacokinetic studies of CYT-6091, a novel PEGylated colloidal gold-rhTNF nanomedicine," *Clin. Cancer Res. ,* vol. 16, p. 6139–6149, 2010.

[50] Y. Tao, J. Han and H. Dou, "Brain-targeting gene delivery using a rabies virus glycoprotein peptide modulated hollow liposome: biobehavioral study," *Mater. Chem,* vol. 22, p. 11808−11815, 2012.

[51] K. L. Young, A. W. Scott, L. Hao, S. E. Mirkin, G. Liu and C. A. Mirkin, "Hollow Spherical Nucleic Acids for Intracellular Gene Regulation Based upon Biocompatible Silica Shells. . 2012,," *Nano Lett,* vol. 12, p. 3867−3871, 2012.

[52] K. H. Bae, K. Lee, C. Kim and T. G. Park, "Surface functionalized hollow manganese oxide nanoparticles for cancer targeted siRNA delivery and magnetic resonance imaging," *Biomaterials,* vol. 32, pp. 176-184, 2011.

[53] K. Cheng and S. Sun, "Recent advances in syntheses and therapeutic applications of multifunctional porous hollow nanoparticles," *Nano Today ,* vol. 5, p. 183−196, 2010.

[54] J. You, G. Zhang and L. Chun, "Exceptionally High Payload of Doxorubicin in Hollow Gold Nanospheres for Near-Infrared Light-Triggered Drug Release," *ACS Nano,* vol. 4, no. 2, p. 1033–1041, 2010.

[55] Y. Zhang, H. F. Chan and K. W. Leong, "Advanced materials and processing for drug delivery: The past and the future," *Adv. Drug Deliv. Rev.,* vol. 65, p. 104, 2013.

[56] J. Lee, S. H. Hwang, J. Yun and J. Jang, "Fabrication of SiO2/TiO2 Double-Shelled Hollow Nanospheres with Controllable Size via Sol−Gel Reaction and Sonication-Mediated Etching," *ACS Appl. Mater. Interfaces ,* vol. 6, p. 15420−15426, 2014.

[57] H. Meng, W. X. Mai, H. Zhang, M. Xue, T. Xia, S. Lin, X. Wang, Y. Zhao, Z. Ji, J. I. Zink and A. E. Nel, "Codelivery of an Optimal Drug/siRNA Combination Using Mesoporous Silica Nanoparticles To Overcome Drug Resistance in Breast Cancer in Vitro and in Vivo," *ACS Nano,* vol. 7, p. 994 – 1005, 2013.

[58] R. I. Pakunlu, Y. Wang, W. Tsao, V. Pozharov, T. J. Cook and T. Minko, "Enhancement of the Efficacy of Chemotherapy for Lung Cancer by Simultaneous Suppression of Multidrug Resistance and Antiapoptotic Cellular Defense," *Cancer Res.,* vol. 64, p. 6214 – 6224, 2004.

[59] T. L. ,. D. C. Fangqiong, "Mesoporous Silica Nanoparticles: Synthesis, Biocompatibility and Drug Delivery," *Adv. Mater.,* vol. 24, no. 12, p. 1504–1534, 2012.

[60] P. Amirali, H. Sandy Budi, S. Frances, L. Jian, Q. Shi Zhang and L. Gao Qing (Max), "Mesoporous silica nanoparticles for bioadsorption, enzyme immobilisation, and delivery carriers," *Nanoscale,* vol. 3, pp. 2801-2818, 2011.

[61] J. Yunfeng, G. Jia, S. Shun, C. Baisong, Z. Yahong, J. Xinguo and Y. Wuli, "Synthesis of discrete and dispersible hollow mesoporous silica nanoparticles with tailored shell thickness for controlled drug release," *J. Mater. Chem.,* vol. 22, pp. 17636-17643, 2012.

[62] M. Xing, Z. Yun, N. Kee Woei and Z. Yanli, "Integrated Hollow Mesoporous Silica Nanoparticles for Target Drug/siRNA Co-delivery," *Chem. Eur. J.,* vol. 19, p. 15593 – 15603, 2013.

[63] J. Nordberg and S. Arnér E., "Reactive oxygen species, antioxidants, and the mammalian thioredoxin system," *Free Radicals Biol. Med., 2001, 31, .,* vol. 31, p. 1287, 2001.

[64] J. Yoonsun, K. Sojin, O. Wan-Kyu, K. Chanhoi, Inkyu and J. Jyongsik, "A folic acid conjugated silica–titania porous hollow nanosphere for improved topical photodynamic therapy," *Chem. Commun.,* vol. 50, pp. 15345--15347, 2014.

Chapter-2:

Synthesis and stabilization of silica-titania hollow nanoparticles

2.1 Introduction

Hollow nanoparticles based on silica-titania composite have gained potentiality as drug delivery vehicles because of their (hollow) interior structure and favourable behaviour within the systems comprising the human body [1] [2] [3] [4] [5]. These nanoparticles offer sizeable cavities that can carry a large amount of therapeutic agent and to release these at specified target sites upon conjugation with appropriate linkers or targeting moieties- on the particle surface [6]. Since hollow nanoparticles can carry more therapeutic cargo rather than solid particles at the same concentration, the side effects of toxicity in the human body are greatly reduced in the case of hollow nanoparticles [7]. Furthermore, experimental approaches have been developed with two accessible sites of hollow nanoparticles (inner and outer) for combination therapy (drug-gene) [8].

The morphology of hollow nanoparticles is crucial since it influences the drug diffusion and release behaviour in the system. Most importantly, drug diffusion and release rates directly control the efficiency of drug action. Since the size of the nanoparticles influences the cellular uptake and cytotoxicity of the nanoparticles, it is important to control their size from a minimum level so that the maximum uptake of nanoparticles by cells can be achieved. Additionally, the shell porosity and thickness of the hollow nanoparticles affect the drug loading capacity, transport efficiency and release rate [9] [10].

There have been several approaches detailed in literature for synthesizing hollow nanoparticles. Amongst those approaches, the hard templating method was applied initially here to synthesize core-shell particles followed by the selective removal of core [2]. Silica nanoparticle was chosen as the core due to their facile synthesis. For forming a shell on core surface, titania was selected for its compact structure and chemical stability. Here silica nanoparticles were synthesized by Stober process [11] and titania on the silica surface was formed through sol-gel reaction to form core-shell nanostructure. Then the sonication and re-deposition process was applied to remove the core silica and allowed to redeposit on the shell surface [12]. The particle size distribution and polydispersity were measured by dynamic light scattering (DLS), scanning TEM (STEM). The crystallinity of hollow nanoparticles was characterized by X-ray diffraction (XRD) and composition was analyzed by energy dispersive X-ray spectroscopy (EDS). The nitrogen physisorption data were extracted from gas adsorption-desorption isotherms and used for the surface area and porosity measurement.

2.2 Experimental

2.2.1 Chemicals:

Tetraethyl orthosilicate (TEOS, 98.0%), titanium isopropoxide (TTIP, 97.0%) were purchased from Sigma-Aldrich, Dorset, UK. Acetonitrile (ACN, 99.8%), ammonium hydroxide (35.0%), ethanol (99.5%) were purchased from Fisher Chemical, UK. Dialysis tubing was purchased from Sigma-Aldrich, UK and washed as stated in the product literature.

2.1.2 Synthesis of Silica-Titania hollow nanoparticles:

Silica-titania hollow nanoparticles (STHNP) were synthesized from silica-titania core-shell nanoparticles (STCSNPs) through a step by step process where silica nanoparticles act as the precursor. Firstly, monodispersed mesoporous silica nanoparticles were synthesized according to the Stöber process [11]. Here, the size of the silica nanoparticles was controlled by tuning the temperature of the system. To prepare 640ml colloidal silica solution, 592ml of ethanol, 19.2ml of ammonium hydroxide and 4.8ml of deionized water were mixed initially. Then 24ml of tetraethyl orthosilicate was added slowly to the mixture to initiate the sol-gel reaction. The colloidal silica solution results after the vigorous stirring of the total mixture at 40°C for 6hr. Then, 18ml of titanium isopropoxide mixed with 90ml ethanol and 30ml acetonitrile was slowly added to the colloidal silica solution, again with vigorous stirring at 4°C, and maintained for a further 6hrs to synthesize porous STCSNP. Next, the silica-titania hollow nanoparticles prepared by sonicating the STCSNP for 2.5hrs at room temperature in presence of 100mM ammonium hydroxide solution [12]. The final solution was then dialyzed against deionized water (resistivity of 18 $M\Omega cm^{-1}$).

2.2.3 Purification and stabilization of STHNPs:

The stability of the purified STHNP was assessed by repeated dialysis and centrifugation to remove unreacted chemical species, observing their polydispersity and aggregation behaviour via light scattering and electron microscopy.

2.2.3.1 Purification and stabilization experiments by dialysis:

STHNPs were dialyzed against deionized water. The dialysis tubing used in the dialysis process was rinsed with 50ml of deionized water for 2hours to remove the humectants. The dialysis was continued for three consecutive days, the counter medium (contaminated water) was changed every 12 hours with fresh deionized water. The procedure was continued until the wash water had low conductivity. Then the dialyzed samples were characterized by size, zeta potential, and polydispersity measurements.

2.2.3.2 Purification and stabilization experiments by centrifugation:

A 15 ml sample of STHNPs dispersions were centrifuged at 13000 g for 30 minutes (Sorvall® RC-5B). After centrifugation finished, the pellet was separated from supernatant and re-dispersed in ethanol. The step was repeated two more times. Finally, the pellet was redispersed in deionized water and the final step was repeated two more times. The procedure was continued until the wash water had low conductivity. Then the samples were characterized by size, zeta potential, and polydispersity measurements.

2.3 Characterization

To monitor the size distribution of silica nanoparticles, STCSNP and STHNP, scanning transmission electron microscopy, (Hitachi SU8030) was used. The energy dispersive X-ray (EDX) was conducted with Thermo-Noran NSS System 7 ultra-dry X-ray detector for elemental analysis. For those observations, each sample was diluted with ethanol and a single drop of diluted sample was deposited on the carbon-coated copper grid and then imaged directly followed by vacuum drying. Nanoparticle sizes were also measured by photon correlation spectroscopy using zetasizer Nano ZS (Malvern Instruments). For size measurement by zetasizer, samples were diluted with deionized water, sonicated for 2mins and filtered through a microfilter. X-ray powder diffraction measurements were taken using D8 Advance X-ray diffractometer (Bruker, Germany) in theta–theta Bragg–Brentano geometry using reflection mode. The diffractograms were collected between 2 and 40° 2θ, with a step size of 0.006° and a counting time of 0.5 s per step using Cu Kα radiation. Nitrogen gas sorption isotherms were measured from Micromeritics 3FLEX instrument at liquid nitrogen temperature. Before running the experiments, samples were degassed for 24 hours at 120°C in vacuum compartment. The BET surface area, pore volume distribution as the function of pore size (diameter) and a specific inner cavity volume of STHNP were calculated from sorption data as will be discussed in result and discussion section.

2.4 Theoretical Platforms

2.4.1 Dynamic light scattering:

Light scattering technique is an easy and cost-effective technique for measuring the size and polydispersity index of nanoparticles. During Brownian motion, particles diffuse irregularly through a solution at a constant rate which is directly linked to the particles' hydrodynamic size. According to the Stokes- Einstein equation:

$$R_h = \frac{k_B T}{6\pi\eta D}$$

where R_h is the particle hydrodynamic radius, T is the temperature, k_B is the Boltzmann constant, η is the viscosity of the solvent, and D is the diffusion coefficient of nanoparticles. The denominator is the inverse of particle mobility and is also denoted as the drag coefficient. In the dynamic light scattering technique, the scattered light is detected by a single photon receiver and is monitored over time. The intensity of signal fluctuations varies with the particles mobility through the system, and the information contained in the correlation function:

$$\mathrm{G}\,(\tau) = \int_0^\infty I(t)(t+\tau)dt$$

where I is the intensity, G (τ) is the correlation coefficient, t is the time and τ is the delay time. If the particles show no movement, then the correlation is 1. Usually, the correlation between the primary and subsequent scattering signal varies as the particles diffuse through the screening window and dependent on the rate and extent of change, information regarding particle diffusion coefficient (which is correlated to particle size through the Stokes-Einstein equation) can be found. More particularly, it is not possible to measure the constant intensity correlation function directly; however, it can be estimated by distinct points obtained with a summation over the experiment period, as illustrated by the following equation:

$$G_k(\tau k) = \sum_{i=0} I(t)(t + \tau k)$$

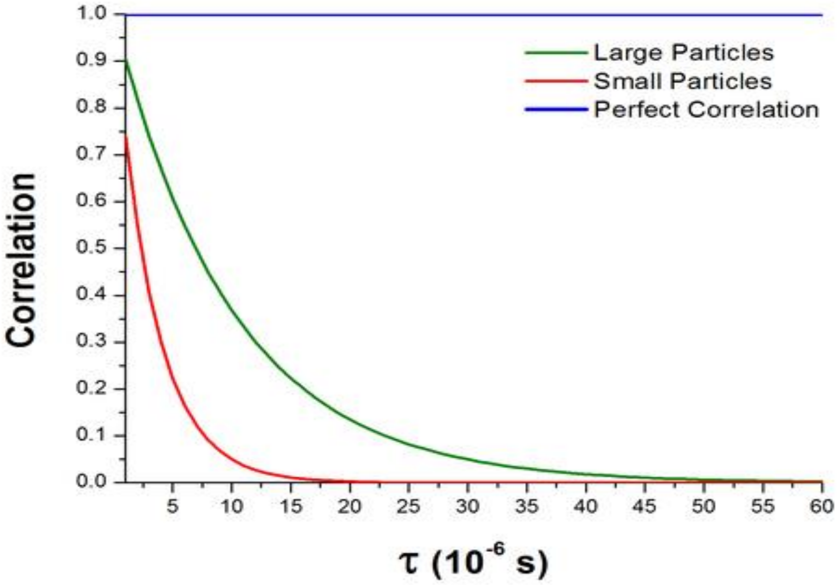

Figure 2. 1: Typical correlograms from a sample. As can be seen, the rate of decay for the correlation function is related to particle size as the rate of decay is much faster for small particles than it is for large. Adapted from [13].

The intensity signal collected by the photon collector and correlator, at time *t*, and then a short time later, *t+δt*, would be very identical, or strongly correlated. After a further period of time, *t+2δt*, there would be still a good correlation, however not as strong as at *t+δt.* And the particles continuously diffuse away from their original point at time *t* as the time passes to *t+3δt, t+4δt, t+5δt,* etc and the signal intensity is lower and there is no good correlation exists as compare to its initial value. Therefore, as the time running out the correlation is decreased exponentially. The time that requires the correlation function to lessen to zero is in the range of 1 to 10s of milliseconds. The expression *δt* used is designated on the range of microseconds or nanoseconds. The duration of time requires for the signal to remain correlated is less, since smaller particles have the ability to diffuse more rapidly, rather than larger particles that shift more slowly.

2.4.2 Scanning transmission electron microscopy:

The scanning transmission electron microscope (STEM) is a precious instrument for the characterization of nano-architectures, offering a variety of different imaging modes with the facility to generate the information on elemental conformation. Literally, STEM mimics the same principle as the typical scanning electron microscope (SEM), by generating a focused beam of electrons that used for sample scanning while some desired signal is detected to produce an image [14]. The difference with SEM is that thin specimen are made during sample preparation so that platform for transmission modes of imaging are also available. STEM can employ secondary or backscattered electron beams for imaging as in the SEM, but higher signal levels and better spatial resolution can also be achieved by detecting transmitted electrons. The key advantages of STEM include the simultaneous application of multiple detectors in extracting maximum information from each scan. The dark field detectors eliminate the transmitted beam resulting dark images of holes. In contrary, a bright field detector produces bright images since it includes the transmitted beam. Each detector generates a different and harmonizing view of the specimen. The maximum benefits can be achieved from STEM instruments by increasing the accelerating voltage of typical SEM instruments working at relatively low voltages when installed with transmitted electron detectors. STEM also comes with spectroscopic technology called electron energy loss spectroscopy (EELS). It is able to show individual atoms of high atomic number, either on surfaces or inside bulk materials. It is even possible to identify single atoms spectroscopically and analyze their local electronic environment by STEM-EELS technology.

2.4.3 Nitrogen physisorption method:

The existence of hierarchical microporous and mesoporous structure of hollow nanoparticles leaves the demand of their fine characterization using sorption-based techniques [15]. Here, the nitrogen sorption method was applied to obtain morphological data of porous nanoparticles as well as hollow mesoporous nanostructures those synthesised here. Different analytical approaches have been developed to analyse nitrogen sorption isotherms which provide information about the specific surface area, pore volume, and size distribution, in some case micropore volume and size distribution of nanoparticles. Here the terms mesopores (2-50nm) define the holes across the shell, micropores to define the pore size less than 2nm, macropores define the pores having the size range > 50nm (Fig: 2.2a). In principle, sorption method related to the adsorption process upon introducing the gas to the nanoparticulate systems and desorption process upon withdrawing or reducing the gas. In adsorption process, when the external gaseous systems are applied, all accessible pores of the surface are become exposed to the low pressure of the adsorptive gas and initiate monolayer formation. However, it needs to be realised that micropores in the nanoparticles shell are filled long before monolayer is formed. Therefore, at higher pressure, the mesopores are being filled. As relative pressure continues to increase, beyond that requires to fill up micropores and mesopores, adsorption takes place in multilayer formation as additional gas molecules are adsorbed.

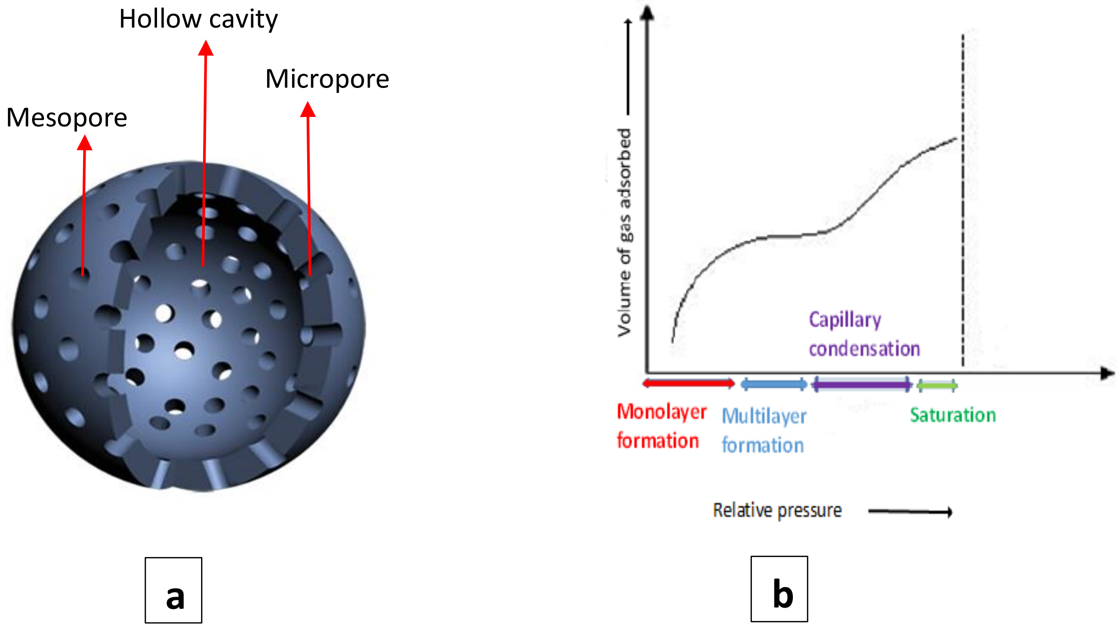

Figure 2. 2: a) A depiction of a hollow nanoparticle; adapted from S. Kim et al [18] b) Schematic representation of different areas of nitrogen sorption isotherm (BET model); adapted from S. Brunaur et al [19].

As the gas pressure is further increased the micropores are filled with liquid condensate due to capillary condensation process to occur (Fig:2.2b). In the meantime, the gas layer is diffused to the hollow inner cavity through micropores via diffusion process and the thickness of gas layer continues to increase. Finally, the liquid condensate of nitrogen fills the mesopores followed by hollow cavity at higher pressure. The desorption process is almost inverse of the adsorption process at high and low pressure. Because of the large cavity inside the hollow nanoparticles, as the vapour pressure decreases desorption branch is followed by delayed evaporation of the adsorptive gas through the pores. This delayed evaporation is facilitated by the pore-blocking mechanisms where liquid condensate is blocked in the micropores area and gives rise to hysteresis loop [16] [17].

To analyse the physisorption data, different analytical approaches have been applied, such as BET (Brunauer-Emmett-Teller) method, t-plot method, and spherical pore model of Kelvin equation which are used for measuring specific surface area, volume and diameter of micropores and pore volume distribution respectively.

The BET method [20]involves the measurement of surface area. It is literally the method for determination of the adsorptive gas required to fill the accessible entire pore space of a solid with a complete monolayer formation. The adsorptive is physically adsorbed at the bare surfaces through the van-der-Waals forces followed by desorption process at reduced pressure and the same temperature. Furthermore, at equilibrium where the rates of evaporation and condensation are balanced, the surface area covered by the monolayer thickness does not fluctuate. However, the monolayer capacity can be calculated from adsorption isotherm by applying the BET equation [20]-

$$\frac{1}{V_a\left(\frac{p}{p_o}-1\right)} = \frac{C-1}{V_m\, C} \times \frac{p}{p_o} + \frac{1}{V_m\, C}$$

where *P* is the partial vapour pressure of nitrogen gas in equilibrium, *P0* is the saturated pressure of nitrogen gas, *Va* is the amount of nitrogen adsorbed at standard pressure and temperature, Vm is the volume of nitrogen at (STDP) to produce an apparent monolayer on the nanoparticles surfaces and c is the dimensionless constant that is related to the enthalpy of adsorption of the nitrogen gas on the powder sample. In other words, C is related to the affinity of the solid with the adsorbate (the N2 molecules), and so to the heat of adsorption. The higher the value of C, the higher the interaction. In any case, BET equation is generally only used to give an apparent surface area related to the adsorption capacity of the solid. At low pressure, BET diagram is plotted between P/*Va*(*P0-P*) and *P*/ *P0* which gives rise to a straight line. From the slope and intercept of linear regression, it is possible to calculate the value of Va and c respectively. The specific surface area is then calculated from the monolayer capacity by evaluating the value for the average area occupied by each complete monolayer formation.

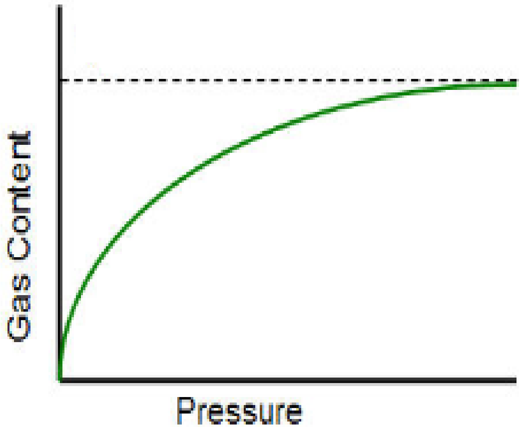

Figure 2. 3: Langmuir adsorption isotherm model. Adapted from [21].

Another model for surface area measurement is Langmuir's model [22]. Usually, this model is more applicable to chemisorption isotherm but it can be often applied to the physisorption isotherm of type I (IUPAC nomenclature) and related to monolayer formation of observed molecules. A convenient expression of Langmuir equation is:

$$\frac{P_a}{V} = \frac{1}{K_{La}V_m} + \frac{P_a}{W_m}$$

where, P_a is the adsorbate equilibrium pressure; V is the adsorbed volume and the V_m is the volume of maximum amount of adsorbate to form monolayer; K_{La} is a constant representing the strength with which the solute is bound to the substrate (Langmuir adsorption constant). In the adsorption system where Langmuir's model is followed, the plot $\frac{P_a}{V}$ versus P_a should give a straight line with $\frac{1}{V_m}$ as slope and $\frac{1}{K_{La}V_m}$ as intercept. Assuming the all adsorption sites are homogenous and knowing the approximate contact area of an adsorbate molecule, surface area of adsorbent could be calculated using following equation:

$$S_A = \frac{V_m N A_x}{M}$$

where, S_A is the surface area, N is the Avogadro's number, M is the molecular weight of the adsorbate and A_x is the contact surface area by each molecule. Although Langmuir's model is applied to the type I adsorption isotherm which is found in the microporous materials, a good understanding about the pore filling mechanism is not possible by this model [21].

Both the Langmuir equation and the Brunauer Emmett Teller (BET) equation model represent the adsorption behavior of a gas (on the surface of a solid) in terms of the monolayer capacity (and hence both can be used for surface area measurement based on that assumption). However, the Langmuir equation is derived around the monolayer being the limit of adsorption (and thus cannot be exceeded - which is known to be incorrect in real physisorption systems with a freely accessible surface), whereas the BET equation models partial and multilayer adsorption in terms of the monolayer (at least up to a point). Therefore, when applying the Langmuir equation to data which is not strictly limited to a monolayer, e.g. "type II" or "IV" isotherm - and not a "type I" (IUPAC nomenclature) it is not surprising that the Langmuir can over-estimate the surface area. This is often very evident by the lack of linearity in the Langmuir plot if using the same calculation range as BET. Yet for many materials, one can find reasonable agreement if the relative pressure (P/Po) points used for the Langmuir are taken at much lower P/Po than for the BET. One can perhaps appreciate the difference between the two approaches from the equations themselves. At first, they do not appear to be so different since both are of the form

$A = B + D$, or more exactly

$A = 1/kV_m + (k'/V_m)(P/Po)$

where $A = (P/Po)/V$ (Langmuir) or $1/V((Po/P)-1)$ (BET). This is the simple expression of the data pairs V (amount adsorbed) and P/Po. In the right side of the equation, the term B is effectively the same, being proportional to $1/ V_m$, V_m being the monolayer quantity, k being related to the heat of adsorption. However, the second term on the right, 'D' is where the difference lies. In the Langmuir equation $k' = 1$, but in the BET equation $k' = (k-1)/k$. In the BET equation, k is usually given the symbol C.

Therefore, the Langmuir equation only considers the heat of adsorption in the B term, not in both B and D, and that's basically the difference between monolayer (Langmuir; figure 2.3) and monolayer-multilayer (BET; figure 2.2b) models.

The t-plot method is usually applied to determine the microporous/mesoporous volumes and the surface area outside the micropores in porous materials including hollow nanostructures [23] [24]. This method was postulated earlier by De Boer and co-workers [25]. This method is based on the use of standard sorption isotherm i.e. t-curve which involves the statistical adsorbed layer thickness on the nanoparticle surfaces as the function of pressure. Several theoretical models or empirical equations are available to describe this function. The semiempirical equation by Harkins-Jura (HJ), for instance, describes the value of the layer thickness without accounting for adsorbate-adsorbent interactions [26].

$$log_{10}\left(\frac{p}{p_o}\right) = 0.034 - 13.99/t^2$$

where t is in Å. If the t-plot of a nanoparticulate system is a straight line, all linear regimens of t-plot provide the evidence that micropores filling with liquid condensate are taken place at specific pressure range. Above this pressure range, multilayer adsorption on mesopores walls continues to occur and a linear relationship is observed between the increase in adsorbed volume and layer thickness. Therefore, a straight line is fitted in the linear region of t-curve, obtained from t-plot. The slope of the straight line gives the value of the surface area outside the micropores and the intercept of the linear fit in the low-pressure range is classically taken as the microporous volume.

Several methods have been developed to understand adsorption, principally at high relative pressures where hysteresis is observed, in terms of pore distribution and capillary condensation. The radii of cylindrical capillaries or spherical pores which fill at a given partial pressure may be calculated by means of the Kelvin equation:

$$r_K = -\frac{2\gamma V_m}{R_o T \ln\left(\frac{p}{p_o}\right)}$$

Here, V_m is the molar volume of liquid nitrogen at temperature T, r_K is the Kelvin radius, γ is the surface tension of nitrogen gas and R_o is nitrogen gas constant. The Kelvin equation relates the effect of the curvature at liquid-vapour interfaces i.e. a meniscus with radius to the equilibrium vapour pressure of a liquid during capillary condensation. The equation also demonstrates that the rate of evaporation is much higher for the smaller droplet liquids than that of the larger droplets since the surface tension and the surface being larger than the volume [27]. Capillary condensation occurs as a result of the adsorption of vapour in small channels that creates the liquid surface with a tiny radius of curvature. The vapour pressure of liquids being lower than that of the same liquid with flat surface is a consequence of the radius being positioned in the vapour phase. The condensation is then started to occur when the actual vapour pressure is greater than the vapour pressure of the curved surface (calculated by using the Kelvin equation). The actual vapour pressure for a flat surface may possibly be lower than its saturation vapour pressure. Once the capillary condensation is started to occur, a meniscus is formed instantly at the liquid-vapour interfaces. The formation of meniscus depends on the liquid’s surface tension and occurs at the pressure below the equilibrium saturation pressure. At low vapour pressure, the unsaturated vapour condenses in a smaller radius of the capillary. Subsequently, as the vapour pressure increases, condensation of the liquid then fill the larger radius of the capillary that causes the radius of the meniscus to increase (capillary become full with condensate). The Kelvin equation implies that the radius of curvature will also further expand towards the opening of the capillary as the ratio of vapour and saturation pressure arise, resulting the flatter surface. Thus, the vapour condensation would occur in a smooth way over the range of vapour pressures. In a parallel manner, the vapour condensation would likely to occur more quickly in case of constant radius height of the capillary present in the system, reaching the equilibrium radius (Kelvin radius, r_K), as soon as possible. This dependency of curvature and pore geometry would result in the formation of hysteresis in the porous system [28] [29]. However, condensation in diverse sized pores follows at different pressure since r_K and t depend on pressure. In principle, calculation for inner radii size distribution starts at saturation pressure (designated as experimental step n = N) and takes reverse sequence to the beginning of the isotherm, i.e. from n = N to n = 1 [30]. Due to diversity of several approaches for calculating pore volume distribution for spherical pores, a modified equation has been proposed based on the Barrett-Joyner-Halenda (BJH) algorithm [31] considering the capillary condensation is ruled by the formation of spherical meniscus [32].

$$\Delta V_p = \left(\frac{\overline{r_{p,n}}}{\overline{r_{p,n}} - \bar{t_n}}\right)^3 . \left(\Delta V_n - \Delta t_n \sum_{i=n+1}^{N} \frac{3\Delta V_{p,i}}{\overline{r_{p,\iota}}} + \Delta t_n . \bar{t_n} . \sum_{i=n+1}^{N} \frac{6\Delta V_{p,i}}{\left(\overline{r_{p,\iota}}\right)^2} \right. \\ \left. - \Delta t_n . (\bar{t_n})^2 . \sum_{i=n+1}^{N} \frac{3\Delta V_{p,i}}{\left(\overline{r_{p,\iota}}\right)^3}\right)$$

Here, $r_{p,n}$ is the radius of pore experiencing condensation, ΔV_n is the change in the measured adsorbed volume detected at point n and ΔV_p is the pores volume for radius $r_{p,n}$. The contribution from ΔV_nat any specific step n<N comes from radius of pores experiencing condensation as well as from layer thickness adsorbed on the pore walls larger than radius $r_{p,n}$.

2.4.4 Colloidal Stability and the DVLO Theory

The DLVO (Derjaguin–Landau–Verwey–Overbeek) theory was introduced by Derjaguin and Landau [33] in 1941 and Verwey and Overbeek [34] in 1948 for describing the stability of the colloidal dispersion. The theory suggests that the particle stability in solution is dependent upon its total potential energy function, *E*. This theory recognises that *E* combines the effect of the several competing contributions:

$$E = E_A + E_R + E_S$$

E_S is the potential energy due to the solvent, it usually only makes a marginal contribution to the total potential energy over the last few nanometers of separation. But, the balance between E_A (the attractive contribution) and E_R (the repulsive contribution) is much more important. They potentially are much larger and operate over a much larger distance.

$$E_A = -A/(12\pi D^2)$$

where A is the Hamaker constant and D is the particle separation. The repulsive potential, E_R is a far more complex function.

$$E_R = 2\pi\varepsilon\, a\delta^2 \exp(-kD)$$

where a is the particle radius, π is the solvent permeability, k is a function of the ionic composition and δ is the zeta potential. According to DVLO theory, the stability of a colloidal system can by determined by the sum of these van-der-Waals attractive (E_A) and electrical double layer repulsive (E_R) forces that exist between particles as they approach each other due to the Brownian motion they are undergoing. This theory suggests that an energy barrier resulting from the repulsive force prevents two particles approaching one another and adhering together (Figure 2.4). But if the particles collide with sufficient energy to overcome that barrier, the attractive force will pull them into contact where they adhere strongly and irreversibly together. Therefore if the particles have a sufficiently high repulsion, the dispersion will resist flocculation and the colloidal system will be stable. However if a repulsion mechanism does not exist then flocculation or coagulation will eventually take place.

When the surface charges are reduced or the concentration of the electrolyte solutions is increased, a small secondary minimum in the potential energy curve appears. Colloid particles may undergo a reversible flocculation due to the secondary minimum because of its weak energy barrier [36], resulting in slow particle aggregation for the surface with a low charge density (Figure 2.3). These weak flocs are sufficiently stable not to be broken up by Brownian motion but may disperse under an externally applied force such as mechanical agitation.

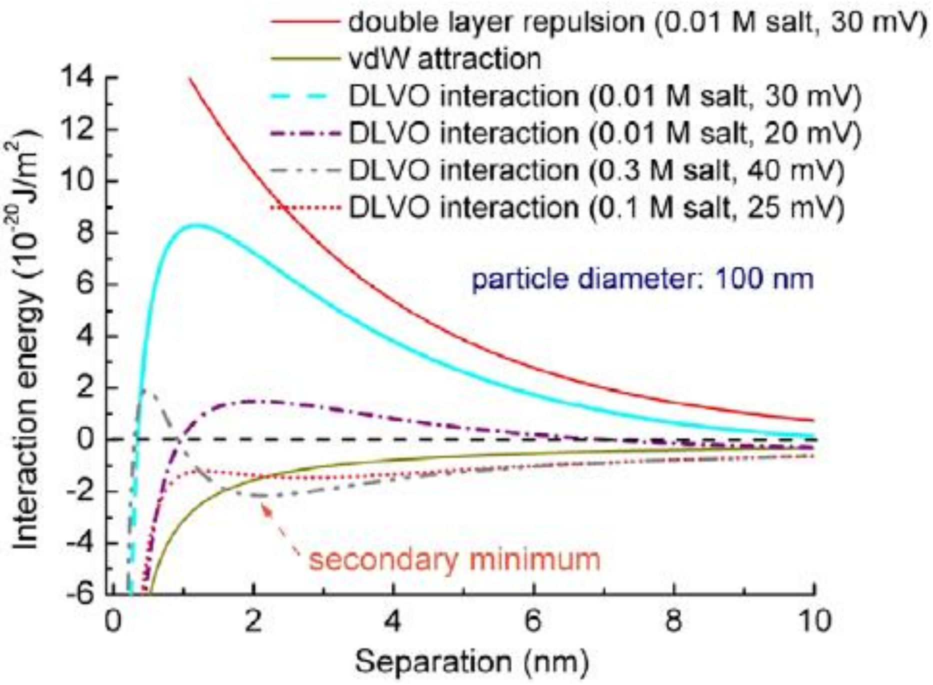

Figure 2. 4: Schematic plot of the DLVO interaction potential energy, E of model nanoparticles (diameter: 100 nm and surface potential: 20–40 mV) which are dispersed in aqueous salt solutions. Adapted from [35]'

Therefore to retain the stability of the colloidal system, the repulsive forces must be dominant. There are two fundamental mechanisms that influence colloidal stability (Figure 2.5): steric repulsion and electrostatic stabilization. Steric repulsion involves the addition of polymers into the system that adsorbs onto the particle surface and prevents the particle surfaces coming into close contact. When sufficient amount of polymer adsorbs, the thickness of the coating is enough to keep particles separated by steric repulsions between the polymer layers, and at those separations, the van der Waals forces are too weak to cause the particles to adhere. And, electrostatic or charge stabilization is the effect on particle interaction due to the distribution of charged species in the system [36].

2.4.5 Powder X - ray diffraction

X - ray diffraction (XRD) is a versatile, non - invasive technique that provides detailed information about the chemical composition and crystallographic structure of natural and synthetic materials. XRD is an advanced technology to examine the crystallinity of a resultant material, whether the material has amorphous or crystalline nature. In crystalline materials, the

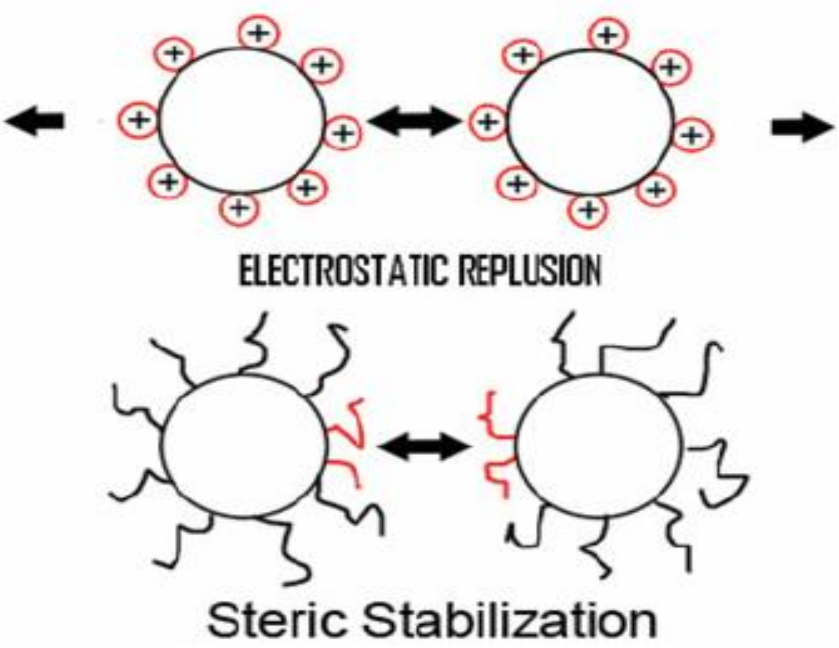

Figure 2. 5: Steric and electrostatic stabilization mechanisms of colloidal dispersions. Adapted from [37]

constituents of the solid (atoms, ions or molecules) are arranged in a regular pattern and in amorphous materials, the constituents are arranged in a random way similar to the disorder that is found in a liquid. When x-rays interact with a crystalline substance, the XRD provides the diffraction pattern which further identifies the actual structure of a material. In the present work, XRD patterns were recorded using D8 advance X-ray diffractometer (Bruker, Germany) in theta–theta Bragg–Brentano geometry using reflection mode.

The principle basis of the X-ray diffraction is the constructive interference of monochromatic X-rays beam and a crystalline sample. X-ray diffractometer consists of an X-ray tube, a sample holder, and an X-ray detector. The X-rays are emitted by X-ray tube, filtered to produce a monochromatic radiation and then focused on the sample. The interaction of the focused X-ray beam with the plans of atoms within the sample produces constructive interference (and a diffracted ray) when conditions follow Bragg's Law ($n\lambda=2d \sin \theta$) [38]. This law relates the wavelength of electromagnetic radiation to the diffraction angle and the lattice spacing in a sample. These diffracted beams are then detected, processed and counted.

X-rays are generated in a cathode ray tube by heating a filament to produce electrons, accelerating the electrons toward a target by applying a voltage, and bombarding the target material with electrons. When the incident electrons have the certain characteristic energy they

can eject the inner shell electrons of the target material and the characteristic X-ray spectra are emitted by the target atom. These spectra consist of several components- the most common being Kα and Kβ. Kα is further divided in Kα1 and Kα2. Kα2 has a slightly larger wavelength and thus possesses the weaker intensity than Kα1. Different target materials (Cu, Fe, Mo, Cr) have specific wavelengths. For filtration of the X-rays, a crystal monochromator is used to produce monochromatic X-rays needed for diffraction. Kα1and Kα2 are sufficiently close in wavelength such that a weighted average of the two is used. Copper is the most common target material for single-crystal diffraction, with CuKα radiation = 1.5418Å. These X-rays are collimated and directed onto the sample. As the sample and detector are rotated, the intensity of the reflected X-rays is recorded. When the geometry of the incident X-rays impinging of the sample follows the Bragg Equation, constructive interference is produced and a peak in intensity arises. A detector records and processes this X-ray signal and converts the signal to a count rate which is then output to a device such as a printer or a computer monitor. The geometry of an X-ray diffractometer is such that the sample rotates in the path of the collimated X-ray beam at an angle θ while the X-ray detector is mounted on an arm to collect the diffracted X-rays and rotates at an angle of 2θ. The instrument used to maintain the angle and rotate the sample is termed as a goniometer. For typical powder patterns, data is collected at 2θ from ~5° to 70°, angles that are preset in the X-ray scan.
By scanning the sample through a range of 2θangles, all possible diffraction directions of the lattice should be attained due to the random orientation of the powdered material. Conversion of the diffraction peaks to d-spacings allows identification of the mineral because each mineral has a set of unique d-spacings. Typically, this is achieved by comparison of d-spacings with standard reference patterns.

2.5 Results and Discussion

2.5.1 Synthesis of hollow nanoparticle

Silica-titania hollow nanoparticles (STHNPs) were synthesized by etching and redeposition process through sonication [12]. The minute representation of overall synthetic procedure is illustrated in figure-2.6. The hollow nanoparticles were successfully fabricated from the silica-titania core-shell nanoparticles (STCSNP) which were formed by formation of titania layer on bare Stöber silica surfaces through a sol-gel process. When sonication was applied to the

STHNP in presence of ammonia solution, the silica core of STCSNP was etched and re-deposited on titania shell surface and this reversible process continues until the hollow

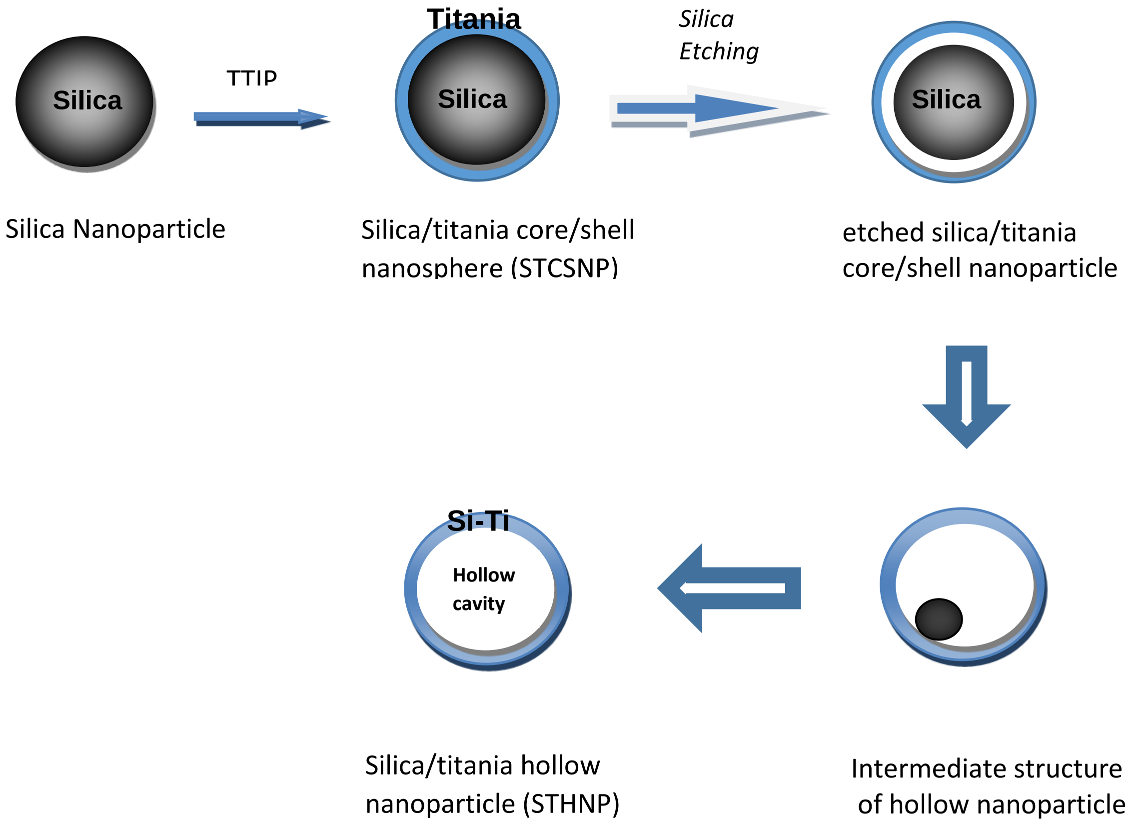

Figure 2. 6: Schematic representation of the formation of hollow nanoparticle from bare silica nanoparticle. The experimental evaluation of hollow nanoparticle formation has been optimized and discussed better here [12].

nanoparticles were evolved. In figure-2.7, the scanning-TEM is showing the images of uniform sized silica, STCSNP, and STHNP which are separated from each other with diameter of ca. 30nm, 50nm and 50nm respectively. The images have revealed the successful formation of titania on silica surface and a hollow inner cavity in hollow nanoparticles. The formation of titania embedded hollow nano-architecture was also confirmed from scanning-TEM/energy dispersive X-ray (STEM-EDX) spectra. Figure-2.9 and 2.10 show the different atomic ratio of silica-titania for STCSNP (75:25) and STHNP (50:50) due to maximum dissolution of silica

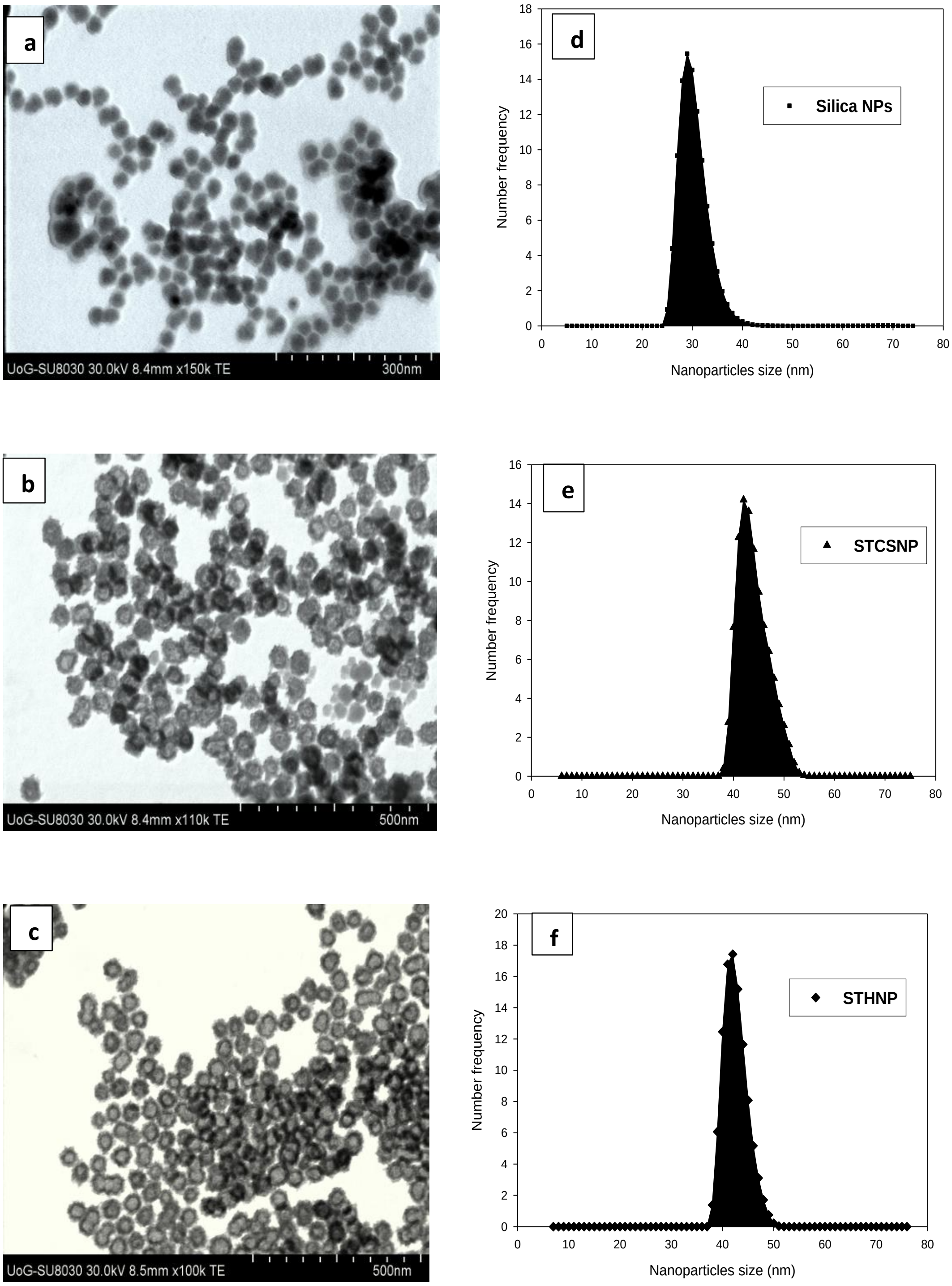

Figure 2. 7: Size distribution of silica, STCSNP, and STHNP. STEM images of a) silica; b) STCSNP; c) STHNP and size measurements of d) silica; e) STCSNP f) STHNP by DLS.

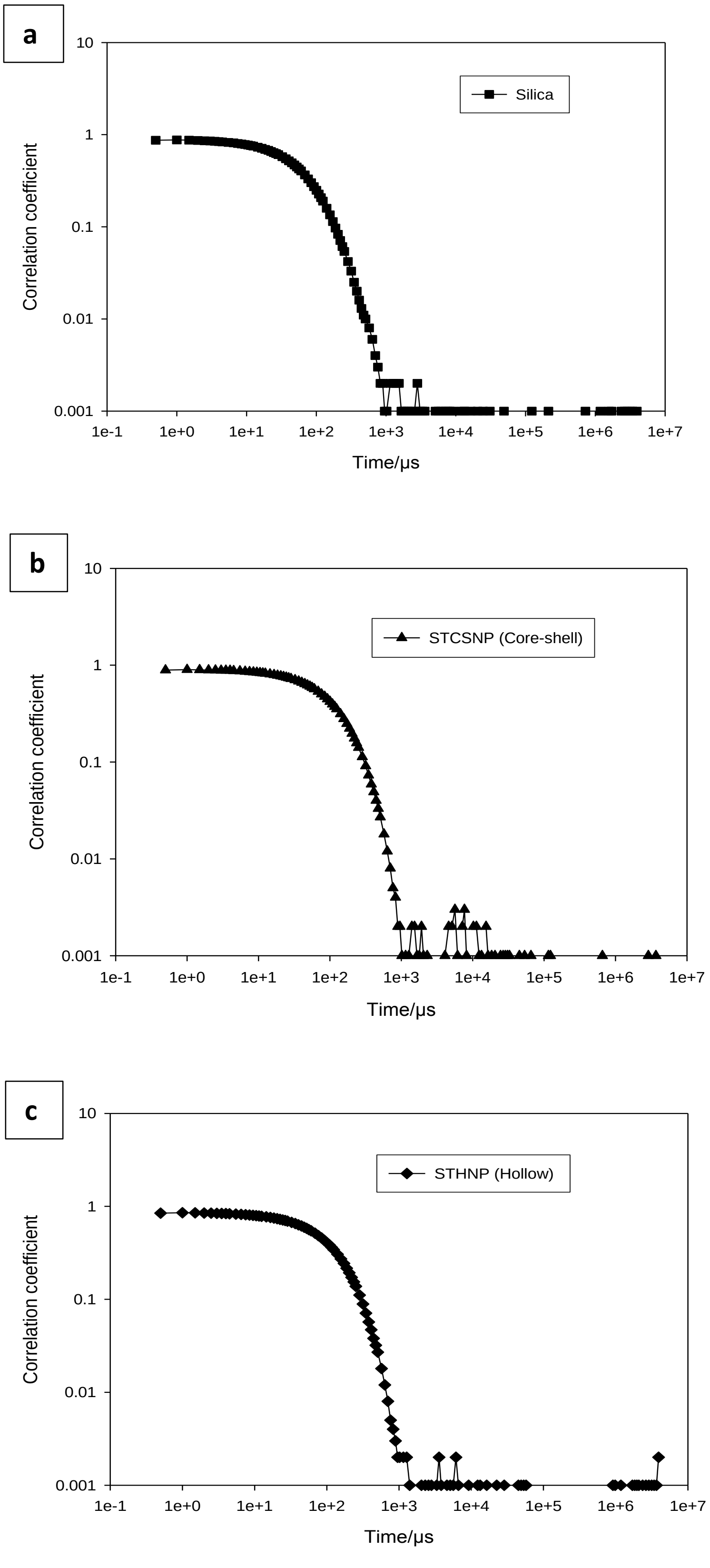

Figure 2. 8: Autocorrelation function for a) Silica b) STCSNP c) STHNP.

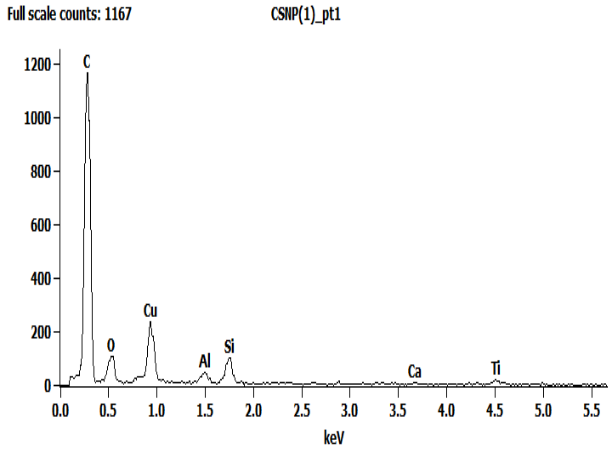

Element Line	Element wt%	Wt% Error	Atom %	Atom % Error
Si K	62.2	± 4.4	73.8	5.2
Ti K	37.8	± 7.5	26.2	5.4
Total	100			

Figure 2. 9: Energy-dispersive X-ray (EDX) spectra and extracted data for the silica/titania core-shell nanoparticle (STCSNP).

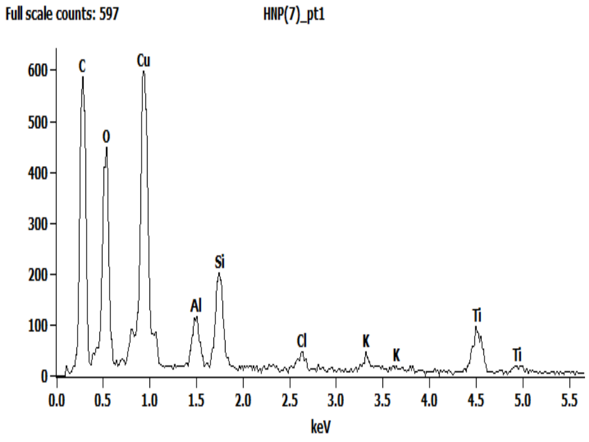

Element Line	Element wt%	Wt% Error	Atom %	Atom % Error
Si K	38.9	± 2.6	52.1	3.5
Ti K	61.1	± 4.2	47.9	3.3
Total	100			

Figure 2. 10: Energy-dispersive X-ray (EDX) spectra and extracted data for the silica/titania hollow nanoparticle (STHNP).

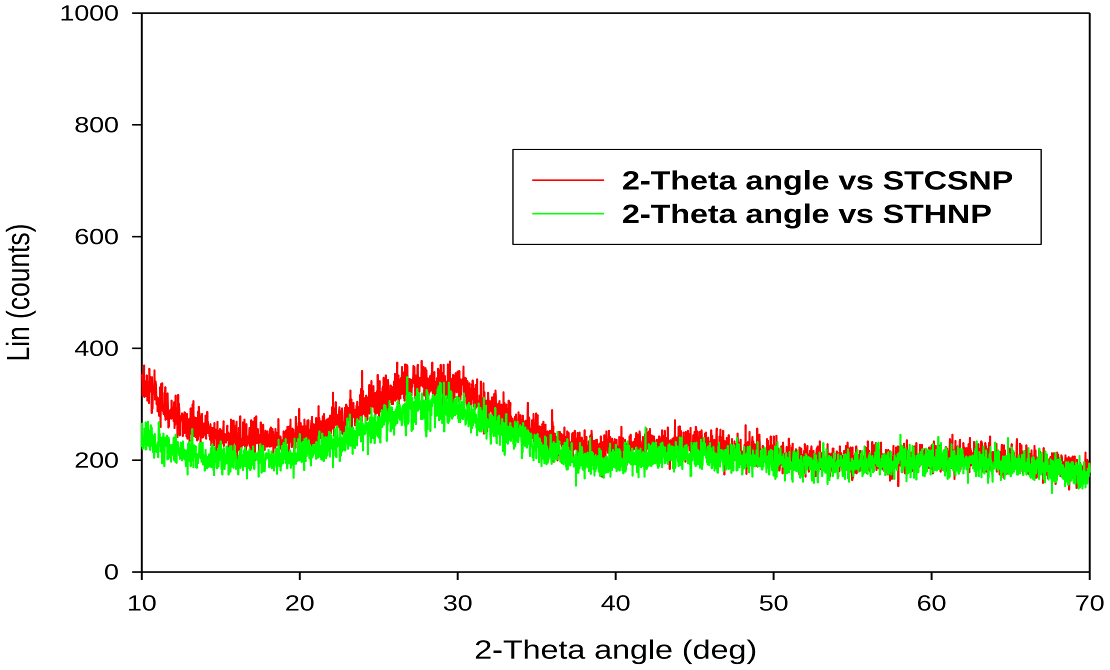

Figure 2. 11: Crystalline state of STCSNP and STHNP.

core under the experimental conditions where titania was partially dissolved owing to their chemical stability. Figure 2.11 shows the crystallinity state of STCSNP and STHNP from X-ray diffraction (XRD) patterns. There were no crystalline peaks observed from XRD results which confirm the amorphous character of STCSNP and STHNP.

The formation of hollow nanoparticles was also confirmed by nitrogen sorption analysis. Figure-2.12 shows the characteristic type IV (IUPAC nomenclature) adsorption isotherm of mesoporous materials and indicates the presence of mesopores [39] [40]. The adsorption-desorption isotherm curve also exhibits an important hysteresis loop of type H2, which are the indication of the complex pore structures or ink-bottle cavity is present in the particles. In complex mesopore system, different sized and shaped of cavities are interconnected to each other by constricted pathways; that is, some wider portion of the pore network are accessible to the bulk gas through a narrow constriction. In such system, a smooth adsorption step and a steep desorption branch are observed, which are the characteristic features of the hysteresis loop of type H2. The evaporation of liquid condensate takes place either through pore-blocking/percolation in a narrow range of pore necks or by cavitation-induced evaporation [41]

[42]. And also the considerable volume of micropores (0.056 cm^3/g) was also observed in STHNPs which contributes to higher pore volume of hollow nanoparticles up to around $0.3cm^3/gm$. Furthermore, the higher BET surface area was calculated for STHNP (around $295m^2/gm$) rather than STCSNPs (around $180m^2/gm$) and silica (around $90m^2/gm$). The cavity size of hollow nanoparticles was found around 32 nm from STEM size measurement. Specific volume of hollow cavity of 0.39 was calculated from step height of desorption isotherm. The details of specific volume calculation for hollow nanoparticles were better

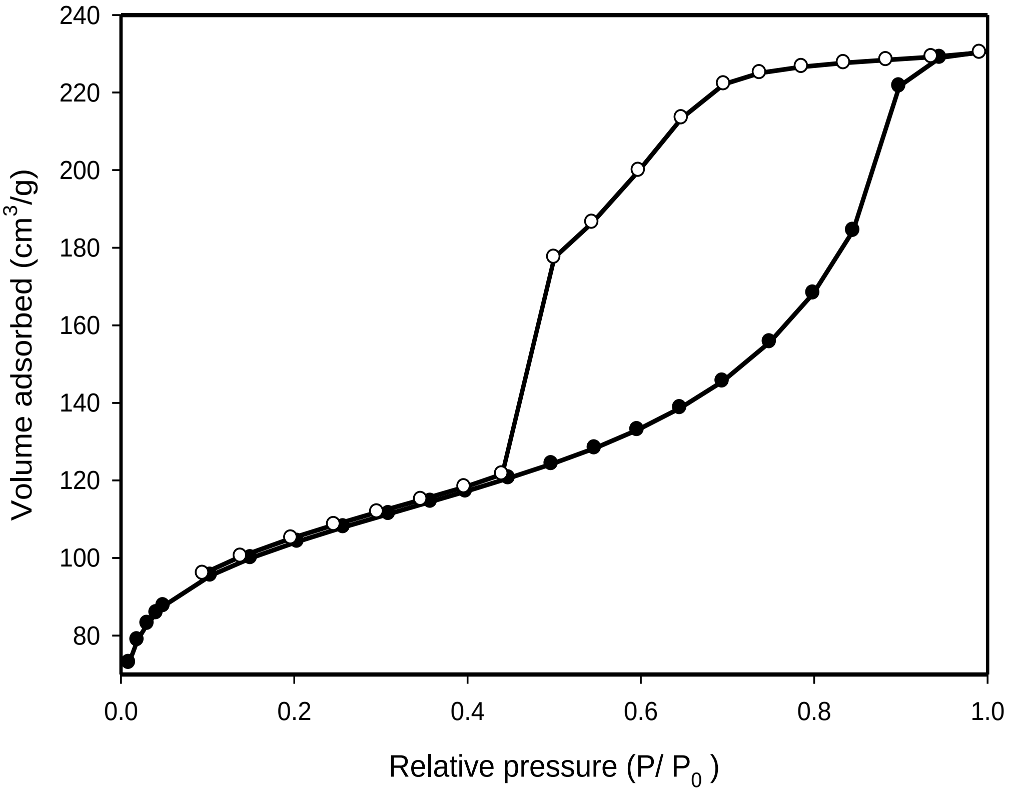

Figure 2. 12: Nitrogen adsorption (●) and desorption (○) isotherm of hollow nanoparticle; surface area of 295 m2/gm.

explained here [30] [43]. The textural properties as well as the amorphous characteristic of STHNP provide the potential capability of higher therapeutic loads in their cavity in case of drug delivery applications. STEM-EDX data indicated that the atomic ratio between silica and titania was changed from about 75:25 (silica-titania core-shell nanoparticles) to 50:50 (hollow nanoparticles) due to the etching of silica core and redeposition process (Figure 2.9 and 2.10). During STCSNP formations, titania shell was formed through the stepwise sol-gel reaction.

Here the ammonium ion used in the Stober process in silica nanoparticles synthesis played an important role in the formation of titania layer on the silica surfaces by overcoming the weak repulsive force and attracting the negatively charged Ti species. When TTIP added to the colloidal silica solution along with the ethanol, TTIP undergoes the hydrolysis reaction in presence of ammonia and results in the Ti hydrolysates. The TTIP molecules and their hydrolysates are highly soluble in ethanol which results in the weaker diffusion of TTIP and their Ti hydrolysates on the silica surfaces and increase the possibility of secondary Ti particles formation in presence of the excess ethanol. On the other hand, acetonitrile used in this experiment has weaker interaction to TTIP molecules and their hydrolysates and there is a weaker interaction between Ti species and ethanol when the acetonitrile mixed with the ethanol. Therefore, an appropriate volume ratio of ethanol and acetonitrile (3:1) during the synthesis procedure has an important impact on diffusing Ti species on the silica surfaces rather than the formation of individual titania particles [44]. Once the Ti species diffused on the silica surfaces, the core-shell structure was then formed followed by the condensation of Ti species by catalysis of ammonia ion on the silica surfaces. Then the STCSNP (core-shell nanoparticles) were subjected to sonication for the synthesis of STHNP (hollow nanoparticles). During the initial stage of STHNP formation, the silica in the silica-titania interfaces of the STCSNP tends to be etched in agreement with sol-gel reaction. Under basic solution (ammonia), the partial dissolution of the silica core is followed by weakening the siloxane bonds and coordinating the hydroxide ions to Si atoms. In contrast, titania was not etched at this stage due to its chemical inertness under same experimental condition [12] [45]. When the sonication is started, a highly rigorous energy is induced through the partially silica etched STCSNPs and initiates the erosion of titania. Further sonication causes continuous etching of silica core and partial etching of titania. According to M. Choi et al, these etched silica and titania species are then dissolved into the solution and redeposit on the titania shell through condensation in accordance with Ostwald ripening. This reversible process continues until developing the hollow void inside the core-shell nanoparticles. Titania on the STCSNP shell is assumed to be compact and still less sensitive to the same rate of sonication (2.5 hours) and ammonia treatment than silica.

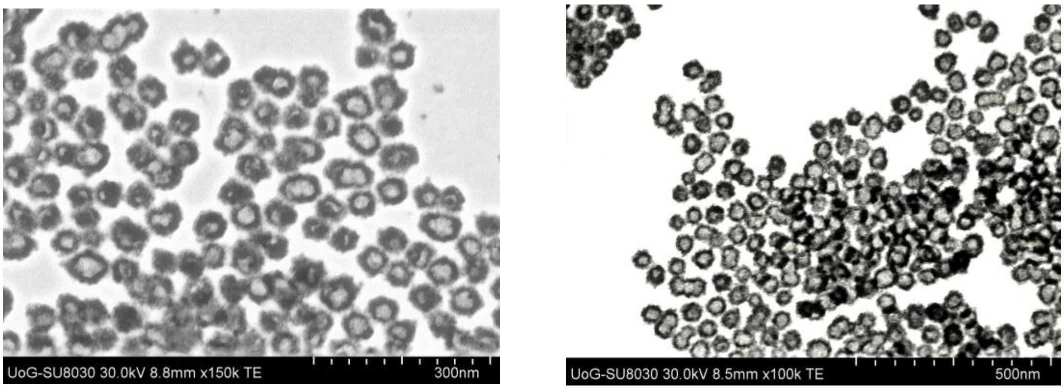

1 hour **2.5 hours**

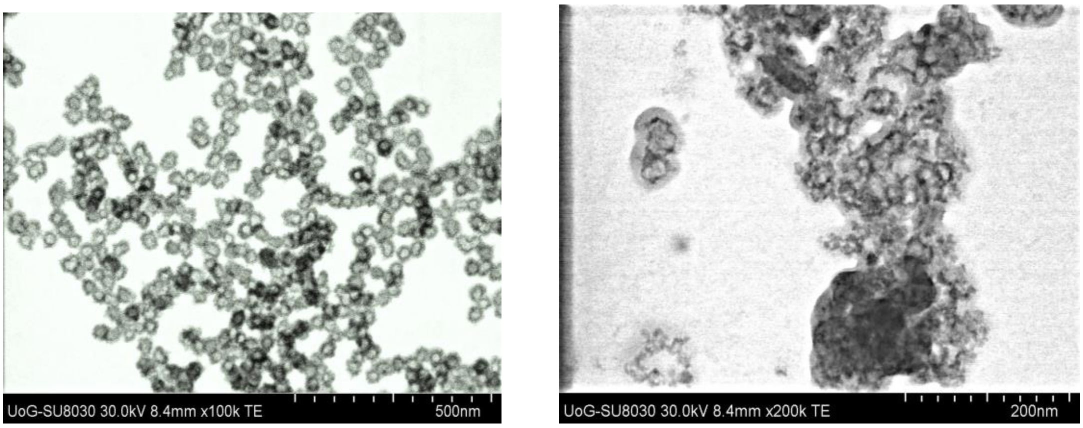

5 hours **7.5 hours**

Figure 2. 13: Evolution of hollow nanoparticles as the function of treatment time (under sonication) in presence ammonia solution.

Figure-2.13 represents the conformational change of STCSNP to STHNP as a function of sonication time in presence of 100mM ammonia solution. After sonication for 1hour, the reduced silica core was observed but cavity between silica core and titania shell interface was generated. In the 2.5 hours treatments, the well-defined cavity was observed within the nanoparticles without aggregation. After 5 hours and 7.5 hours treatment time the nanoparticles conformational change became worse and the hollow nanoparticles started to aggregate. This may be due to the over redeposition of etched silica or titania on the titania shell of the hollow nanoparticles. Therefore, 2.5 hours treatment time is the appropriate time for fabricating silica-titania hollow nanoparticles.

2.5.2 Stabilization of silica-titania hollow nanoparticles:

The purification and stabilization of purified STHNP were compared between that purified by dialysis and centrifugation. After dialyzing, the samples were found really stable, well dispersed in water. In contrary, the compact pellet of nanoparticles was observed when purified by centrifugation. Those pellets were hard to re-disperse in water of the same volume of supernatant. Indeed, even strong agitation was applied using a vortex machine for 20 minutes to break down the pellets. After agitation, the pellets were mixed through the system for short period of time after what they just went down and formed sedimentation. Figure 2.8 shows the size distribution data of dialyzed and centrifuged samples found from light scattering technique and STEM images. Table 2.1 shows the value of polydispersity index (PDI), zeta potential and also size measurement of purified after dialysis and centrifugation. STEM images show the aggregated particles in centrifuged sample and monodisperse particles can be seen in the dialyzed sample (Figure 2.14). This agreement is well matched with the value found by the light scattering technique as well where PDI of centrifuged samples is higher than the dialyzed samples and zeta potential value considerably dropped from -54 (dialyzed sample) to -22 (centrifuged sample) (Table 2.1). Moreover, there is an additional peak can be seen from the

Table 2. 2: Light scattering data of STHNP found after dialysis and centrifugation.

STHNP purification process	Average Size (nm) from DLS measurement	Polydispersity index (PDI)	Zeta potential (mV)
Dialysis	50 ± 0.67	0.096	-54
Centrifugation	95 ± 0.98	0.776	-22

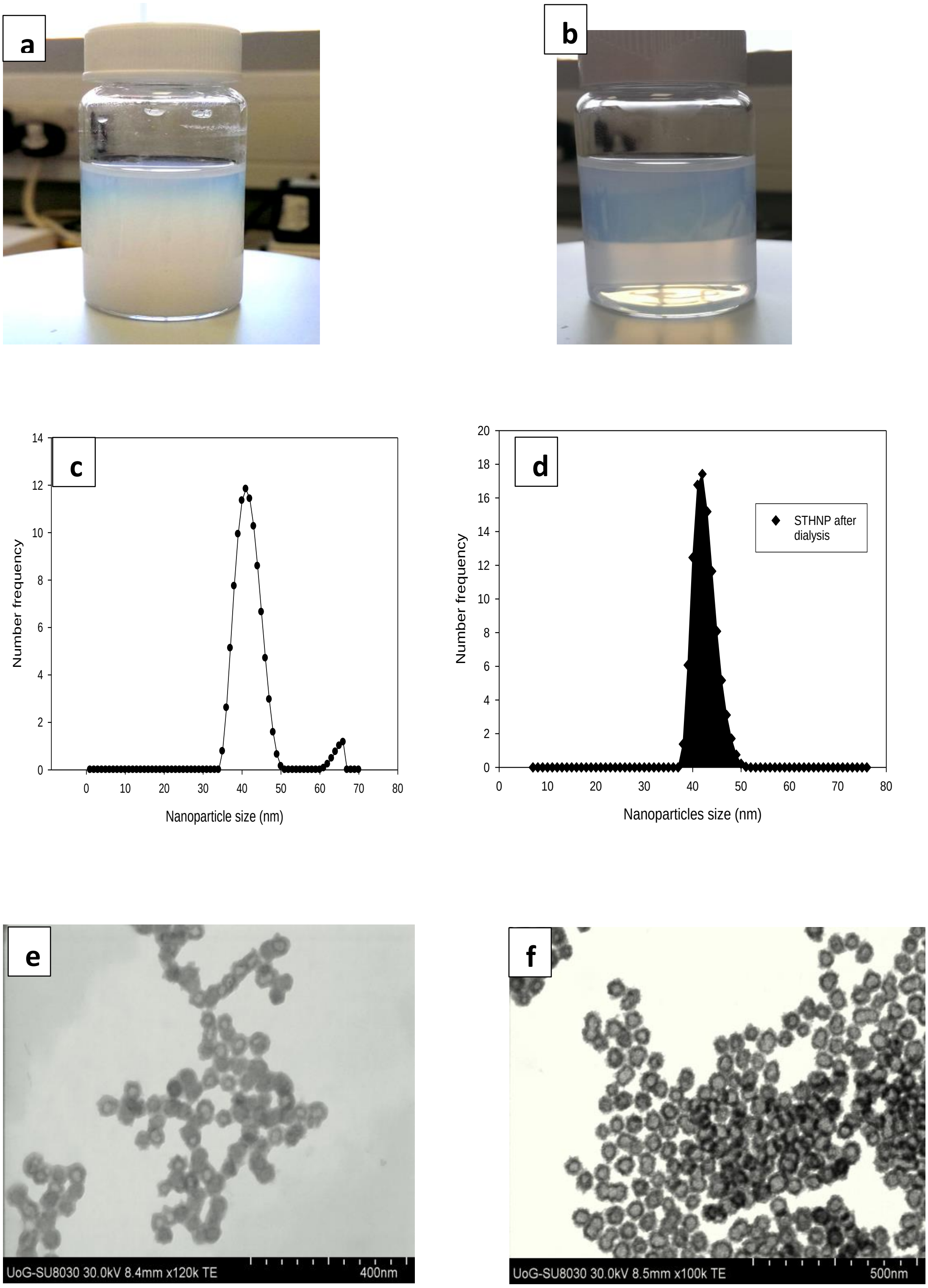

Figure 2. 14: Characteristics of STHNP purified and stabilized by dialysis and centrifugation where a, c, e are the dispersion image, light scattering measurement and STEM image of STHNP from centrifugation process. And b, d, f figures for STHNP from dialysis process.

size distribution of centrifuged sample and this is due to the presence of agglomerate in pellets found after centrifugation. Although the size distribution of hollow nanoparticles after dialysis and centrifugation were found quite similar (except the additional peak) but complete re-dispersion of nanoparticles pellets was not possible. These characteristics are the consequences of the fact that centrifugation method generates a gradient osmotic pressure in the sediment [46].

2.6 Conclusion

In this part of the project, monodisperse silica and silica-titania core-shell nanoparticles were initially synthesized by the sol-gel process. Then uniformly sized of hollow nanoparticles were prepared by sonication and re-deposition method. The potentiality of hollow nanoparticles as a drug delivery carrier was justified by series of characterization technique. The formation of the hollow cavity was shown by STEM image and nitrogen sorption data. STEM-EDX data confirmed the chemical composition of the STCSNP (core-shell nanoparticles) and STHNP (hollow nanoparticles) with mixed silica-titania surface (hollow nanoparticles). The experiments also suggested that the dialysis is superior process than centrifugation for purification of hollow nanoparticles. The synthesized silica, core-shell nanoparticles, and hollow nanoparticles were purified for further studies with solvent relaxation NMR.

Bibliography

[1] Y. Jang, S. Kim, W.-K. Oh, C. Kim, I. Lee and J. Jang, "A folic acid conjugated silica–titania porous hollow nanosphere for improved topical photodynamic therapy," *Chem. Commun. ,* vol. 50, pp. 15345--15347, 2014.

[2] X. Wang, J. Feng, Y. Bai, Q. Zhang and Y. Yin, "Synthesis, Properties, and Applications of Hollow Micro-/Nanostructures," *Chem. Rev.,* vol. 116, no. 18, p. 10983–11060, 2016.

[3] S. Kim, Y. Jang, W.-K. Oh, C. Kim and J. Jang, "Fabrication of Barium- and Strontium-Doped Silica/Titania Hollow Nanoparticles and Their Synergetic Effects on Promoting Neuronal Differentiation by Activating ERK and p38 Pathways," *Adv. Healthcare Mater. ,* vol. 3, no. 7, p. 1097–1106, 2014.

[4] W.-K. Oh, S. Kim, M. Choi, C. Kim, Y. S. Jeong, B.-R. H. J.-S. Cho and J. Jang, "Cellular Uptake, Cytotoxicity, and Innate Immune Response of Silica−Titania Hollow Nanoparticles Based on Size and Surface Functionality," *ACS Nano,* vol. 4, no. 9, p. 5301–5313, 2010.

[5] C. Kim, S. Kim, W.-K. Oh, M. Choi, Jang and Jyongsik, "Efficient Intracellular Delivery of Camptothecin by Silica/Titania Hollow Nanoparticles," *Chem. Eur.,* vol. 18, p. 4902 – 4908, 2012.

[6] Y. Jang and J. Jang, "CPT Encapsulated Silica-titania Hollow Nanoparticle Targeting SK-BR-3 Cells for efficient Anticancer treatment," *Mater. Res. Soc. Symp. Proc. ,* vol. 1725, 2015.

[7] X. W. Lou, L. A. Archer and Z. Yang, "Adv. Mater.," *Hollow Micro-/Nanostructures: Synthesis and Applications,* vol. 20, p. 3987–4019, 2008.

[8] M. Xing, Z. Yun, N. Kee Woei and Z. Yanli, "Integrated Hollow Mesoporous Silica Nanoparticles for Target Drug/siRNA Co-delivery," *Chem. Eur. J.,* vol. 19, p. 15593 – 15603, 2013.

[9] Z. Z. Li, L. X. Wen, L. Shao and J. F. Chen, "Fabrication of Porous Hollow Silica Nanoparticles and Their Applications in Drug Release Control," *Control. J. Controlled Release,* vol. 98, p. 245−254, 2004.

[10] B. Yu, D. A. Wang, Q. Ye, F. Zhou and W. M. Liu, "Robust Polydopamine Nano/Microcapsules and Their Loading and Release Behavior," *Chem. Commun. ,* vol. 44, pp. 6789-6791, 2009.

[11] W. Stöber and A. Fink, "Controlled growth of monodisperse silica spheres in the micron size range," *J. Colloid Interface Sci.,* vol. 26, pp. 62-69, 1968.

[12] C. Moonjung, K. Chanhoi, J. Soon, Y. Kyoung, L. Jun and J. Jyongsik, "Synthesis of titania embedded silica hollow nanospheres via sonication mediated etching and re-deposition," *Chem. Commun., 2011, 47, ,* vol. 47, p. 7092–7094, 2011.

[13] B. Nail, "LibreTexts," 3 September 2014. [Online]. Available: http://chem.libretexts.org/Core/Analytical_Chemistry/Instrumental_Analysis/Microscopy/Dynamic_Light_Scattering. [Accessed 17 January 2017].

[14] A. V. Crewe, J. Wall and J. Langmore, "Visibility of Single Atoms," *Science,* vol. 168, no. 3937, pp. 1338-1340, 1970.

[15] M. Thommes, S. Mitchell and J. Perez-Ramirez, "Surface and Pore Structure Assessment of Hierarchical MFI Zeolites by Advanced Water and Argon Sorption Studies," *J. Phys. Chem. C,* vol. 116, p. 18816., 2012.

[16] Y. P. Khitev, Y. G. Kolyagin, I. I. Ivanova, O. A. Ponomareva, F. Thibault-Starzyk, J. P. Gilson, C. Fernandez and F. Fajula, "Synthesis and Catalytic Properties of Hierarchical Micro/Mesoporous Materials based on FER Zeolite," *Microporous Mesoporous Mater.,* vol. 146, p. 201, 2011.

[17] P. I. Ravikovitch and A. V. Neimark, "Experimental Confirmation of Different Mechanisms of Evaporation from Ink-Bottle Type Pores: Equilibrium, Pore Blocking, and Cavitation," *Langmuir,* vol. 18, pp. 9830- 9837, 2002.

[18] S. Kim, Y. Jang, W.-K. K. ,. C. Oh and J. Jang, "Fabrication of Barium- and Strontium-Doped Silica/Titania Hollow Nanoparticles and Their Synergetic Effects on Promoting Neuronal Differentiation by Activating ERK and p38 Pathways," *Adv. Healthcare Mater.,* vol. 3, p. 1097–1106, 2014.

[19] S. Brunauer, L. S. Deming, W. E. Deming and E. Teller, "On a Theory of the van der Waals Adsorption of Gases," *J. Am. Chem. Soc.,* vol. 62, p. 1723–1732, 1940.

[20] S. Brunauer, P. H. Emmett and E. Teller, "Adsorption of Gases in Multimolecular Layers," *J. Am. Chem. Soc. ,* vol. 60, p. 309−319, 1938.

[21] S. Lowell, J. E. Shields, M. A. Thomas and M. Thommes, "Surface Area Analysis from the Langmuir and BET Theories," in *Characterization of Porous Solids and Powders: Surface Area, Pore Size and Density*, Springer Netherlands, 2004, pp. 58-81.

[22] I. Langmuir, "THE ADSORPTION OF GASES ON PLANE SURFACES OF GLASS, MICA AND PLATINUM," *J. Am. Chem. Soc.,* vol. 40, p. 1361–1403, 1918.

[23] J. H. Deboer, B. C. Lippens, B. G. Linsen, J. C. Broekhof, A. Vandenhe and T. J. Osinga, "T-curve of Multimolecular N2-Adsorption.," *J.Colloid Interface Sci.,* vol. 21, pp. 405-414, 1966.

[24] P. Voogd, J. J. F. Scholten and H. van Bekkum, "Use of the t-Plot-De Boer Method in Pore Volume Determinations of ZSM-5 Type Zeolites," *Colloids Surf. ,* vol. 55, p. 163−171, 1991.

[25] B. Lippens and J. de Boer, "Studies on Pore Systems in Catalysts: V. the t Method.," *J. Catal. ,* vol. 4, p. 319, 1965.

[26] W. D. Harkins and G. Jura, "Surfaces of Solids XIII a Vapor Adsorption Method for the Determination of the Area of a Solid without the Assumption of a Molecular Area, and the Areas Occupied by Nitrogen and Other Molecules on the Surface of a Solid," *J. Am. Chem. Soc. ,* vol. 66, p. 1366−1373, 1944.

[27] L. R. Fisher, R. A. Gamble and J. Middlehurst, "The Kelvin equation and the capillary condensation of water," *Nature,* vol. 290, pp. 575 - 576, 1981.

[28] M. Miyahara, H. Kanda, T. Yoshioka and M. Okazaki, "Modeling Capillary Condensation in Cylindrical Nanopores: A Molecular Dynamics Study," *Langmuir,* vol. 16, pp. 4293-4299, 2000.

[29] "Wikipedia," January 2017. [Online]. Available: https://en.wikipedia.org/wiki/Capillary_condensation. [Accessed February 2017].

[30] H. C. Zhi, K. Chanhoi, Z. Xiang-bing, H. H. Sun, J. Jyongsik and U. Goran, "Characterizing Size and Porosity of Hollow Nanoparticles: SAXS, SANS, TEM, DLS, and Adsorption Isotherms Compared," *Langmuir ,* vol. 28, pp. 15350-15361, 2012.

[31] E. P. Barrett, L. G. Joyner and P. P. Halenda, "The Determination of Pore Volume and Area Distributions in Porous Substances. I. Computations from Nitrogen Isotherms," *J. Am. Chem. Soc.,* vol. 73, pp. 373-380, 1951.

[32] R. Jhonny Villarroel, B. Deicy and S. Karim, "Improvement in the Pore Size Distribution for Ordered Mesoporous Materials with Cylindrical and Spherical Pores Using the Kelvin Equation," *Top Catal,* vol. 54, p. 121–134, 2011.

[33] B. Derjaguin and L. Landau, "Theory of the stability of strongly charged lyophobic sols and of the adhesion of strongly charged particles in solutions of electrolytes," *Acta Phys. Chim. URSS ,* vol. 14, p. 633, 1941.

[34] E. J. W. Verwey and J. T. G. Overbeek, Theory of the Stability of Lyophobic Colloids, Amsterdam: Elsevier, 1948.

[35] D. Guo, G. Xie and J. Luo, "Mechanical properties of nanoparticles: basics and applications," *J. Phys. D: Appl. Phys.,* vol. 47, pp. 013001-013025, 2014.

[36] T. Cosgrove, Colloidal Science: Principles, Methods and Applications (2nd Edition), West Sussex: John Willey & Sons Ltd., 2010.

[37] Ayouril, "Wikimedia Commons," 4 June 2011. [Online]. Available: https://commons.wikimedia.org/wiki/File%3AElectro-Steric_Stabilization.jpg . [Accessed 17 January 2017].

[38] W. H. Bragg and W. L. Bragg, "The Reflection of X-rays by Crystals," *Proc. R. Soc. Lond. A.,* vol. 88, pp. 428-438, 1913.

[39] K. Sing, D. Everett, R. Haul, L. Moscou, R. Pierotti, J. Rouquerol and T. Siemieniewska, "Reporting physisorption data for gas/solid systems with special reference to the determination of surface area and porosity," *Pure Appl. Chem. ,* vol. 57, p. 603–619, 1985.

[40] J. Broekhoff, "Mesopore determination from nitrogen sorption isotherms: Fundamentals, scope, limitations," *Stud. Surf. Sci. Catal.,* vol. 3, p. 663–684, 1979.

[41] M. Thommes, B. Smarsly, M. Groenewolt, P. I. Ravikovitch and A. V. Neimark, "Adsorption Hysteresis of Nitrogen and Argon in Pore Networks and Characterization of Novel Micro- and Mesoporous Silicas," *Langmuir,* vol. 22, pp. 756-764, 2006.

[42] M. Thommes, K. Kaneko, A. V. Neimark, J. P. Olivier, F. Rodriguez-Reinoso, J. Rouquerol and K. S. Sing, "Physisorption of gases, with special reference to the evaluation of surface area and pore size distribution (IUPAC Technical Report)," *Pure and Applied Chemistry,* vol. 87, p. 1051–1069, 2015.

[43] H. Blas, M. Save, P. Pasetto, C. Boissie`re, C. Sanchez and B. Charleux, "Elaboration of Monodisperse Spherical Hollow Particles with Ordered Mesoporous Silica Shells via Dual Latex/Surfactant Templating: Radial Orientation of Mesopore Channels," *Langmuir,* vol. 24, pp. 13132-13137, 2008.

[44] W. Peng, C. Dong and T. Fang-Qiong, "Preparation of Titania-Coated Polystyrene Particles in Mixed Solvents by Ammonia Catalysis," *Langmuir,* vol. 22, no. 10, p. 4833, 2006 .

[45] W. H. Suh, A. R. Jang, Y.-H. Suh and K. S. Suslick, "Porous, Hollow, and Ball-in-Ball Metal Oxide Microspheres: Preparation, Endocytosis, and Cytotoxicity," *Adv. Mater,* vol. 18, p. 1832–1837, 2006.

[46] M. Ce´line, P. Fre´de´ric, M. Albert, M. Martine, L. Vincent, L. Peter and C. Bernard, "Osmotic Compression and Expansion of Highly Ordered Clay Dispersions," *Langmuir,* vol. 22, pp. 4065-4075, 2006.

Chapter-3:

Quantification of the shell porosity of bare Hollow nanoparticles and upon adsorption of Polymer: A comparative study by DLS, BET and Solvent relaxation NMR

3.1 Introduction

Recent years have witnessed the massive applications of nanotechnology in medicine and more specifically drug delivery is set to spread rapidly. There is increasing optimism of using nanoparticles in pharmaceutical formulations which are under investigation for a range of healthcare product applications including drug delivery, medical devices, and controlled release systems [1] [2] [3] [4]. These formulations often present multiple challenges during their development and application stages that require a thorough understanding of the formulation in molecular level. In a nanoparticulate formulation, nanoparticles are usually dispersed in the liquid system at high volume fraction. So it is important to know the dispersion process, stability and aggregation behaviour of these particles at high concentration range in dispersion medium [5]. To understand this optimum features of the nanoparticles in the system a sophisticated characterization procedure is vital. In this particulate system, the extent of the nanoparticle interfaces is counted as the basic parameter that controls the physicochemical nature of whole system. So the measurement of the total wetted surface of the nanoparticle interfaces are vital and their interaction with dispersion medium need to be monitored and controlled [6].

Here solvent relaxation NMR technique was used to analyze the three different structured nanoparticulate dispersions, namely- silica nanoparticles, silica-titania core-shell nanoparticles (STCSNP) and silica-titania hollow nanoparticles (STHNP). Solvent NMR spectroscopy is powerful and non-invasive analytical technique with the easy operating system. It is a useful tool for investigating overall molecular structure and dynamics of the particles [6]. This technique has been extensively used to probe the interaction between the liquid system and the different inorganic and organic particle surfaces (functional group) in dispersion medium [7] [8] [9]. Solvent relaxation NMR could be also useful for investigating the relaxation behaviour of liquid in the vicinity of porous and hollow structures. Here, the water relaxation in hollow nanoparticles was studied for the first time and the completely two different surfaces are counted for water adsorption. Recently, D. Fairhurst *et al* showed the relaxation studies of different solvent in porous nanostructured carbon materials where they compare the total wetted surface area of the outer surface and an inner surface (limited to pore) with conventional surface area measurement technique [6]. For this kind of nanostructure with more than one surfaces exists, are expected to generate double-exponential decays in spectroscopy which is indicative of different morphology of the particle other than the bare surface (porous and hollow) [10].

Where the matter of adsorption of polymer on particle interfaces, the NMR relaxation measurements can provide valuable information of polymer-particle, surfactant-particle and even polymer-surfactant interaction on particle interface. Polymers are the versatile components, extensively used in the field of drug delivery system, cosmetics and detergency [11]. Adsorbed polymer in the colloidal dispersion is mostly used to control the rheology and stability [5] [12]. Here, the adsorption of different molecular weights PVP were investigated on three different synthesized nanoparticles. The adsorption of PVP on silica surface has already been described widely in the literature [7] [13] [11] [8] [14]. But polymer adsorption study with hollow nanoparticles has not done yet. In this section of the project, our key concentration was focused on water relaxation behaviour at core-shell nanoparticle and vicinity of the hollow nanoparticle. The focus was also devoted to studying of PVP adsorption on titania-coated silica nanoparticles (STCSNP) and hollow nanoparticles (STHNP) as well. In core-shell nanostructure, titania is the main adsorbing site for PVP where inner and outer surface were exposed to PVP in the case of hollow nanoparticles. Since the surfaces of the hollow nanoparticle are literally the mixture of silica-titania composite, the preferred adsorption sites for PVP on surfaces has also been investigated. Here, the light scattering technique with NMR relaxation data were combined for better understanding of polymer adsorption trend on the complex structures.

3.2 Theoretical Background

3.2.1 Theory of Nuclear Magnetic Resonance

Nuclear magnetic resonance (NMR) is a phenomenon which occurs when the nuclei of certain atoms are immersed in a static magnetic field and exposed to a second oscillating magnetic field.The basic theory of the NMR is related to the nuclei of atoms those possess a property called spin.

3.2.1.1 Nuclear spin and splitting of energy states

It is imagined that subatomic particles (electrons, protons, and neutrons) can spin on their own axis. These spins are paired against each other in many atoms and have no overall spin, for example, the most common naturally occurring isotope of carbon (^{12}C) contains 6 protons and 6 neutrons and undergoes coupling and has no net spin. However, the nucleus of some atoms (e.g. ^{1}H and ^{13}C) does possess an overall spin. There are some general rules that apply to determine the net spin of a nucleus are as follows-

- The nucleus that has the even number of both neutrons and protons, then nucleus has no spin. Examples include ^{4}He, ^{12}C, ^{16}O and ^{32}S.
- The nucleus that has the odd number of both neutrons and protons, then nucleus has a half-integer spin. Examples include^{14}N (I=1),^{2}H (deuterium, I=1), and^{10}B (I=3)
- The remaining nuclei (odd/even and even/odd) all have spins that are half-integral. Examples include ^{1}H (I=½), ^{17}O (I=3/2), ^{19}F (I=½), ^{23}Na (I=3/2), and ^{31}P (I=½).

The net spin, I, of the nucleus is important. According to quantum mechanics theory, a nucleus of spin I will possess $2I + 1$ possible orientation. Hence for the ^{1}H nucleus with $I = ½$, will have $2(½) + 1 = 2$ possible spin states. These states are commonly denoted as |+½> and |-½>, often denoted as "spin up" or "parallel" and "spin-down" or "anti-parallel" respectively. These two separate spin states for hydrogen are of equal energy in the absence of an external magnetic field. If a magnetic field is applied, then the energy levels split and each level is given a magnetic quantum number, m.

3.2.1.2 Transition and transition energy

When the nucleus faces the magnetic field, the direction of the external field is usually defined to be the z direction and the initial populations of the energy states are determined by thermodynamics that can be described by the Boltzmann distribution. This is important, and it means that the higher energy sate will have slightly less number of nuclei than the lower state. It is possible for nuclei in lower energy state to absorb electromagnetic radiation and get excited into the higher energy state. The radiation frequency needed for excitation of nuclei can be determined by the difference in energy between the energy states.

Since nucleus has a positive charge and got net spin, so it acts like a little magnet and generates a small magnetic field. Therefore the nucleus possesses a nuclear magnetic moment, m, which is proportional to its spin, *I*.

$$\mu = \frac{\gamma I h}{2\,\pi}$$

The constant,γ, is called the magnetogyric ratio and is a fundamental nuclear constant. Different nucleus has different magnetogyric ratio. h is Plancks constant.

The energy of a specific energy level is given by;

$$E = -\,\frac{\gamma h}{2\,\pi}\,m\,B°$$

where $B°$ is the strength of the magnetic field at the nucleus. The energy difference between energy states (the transition energy) can be found from-

$$\Delta E = \frac{\gamma h B°}{2\,\pi}$$

This means the energy gap between the spin states for a proton is proportional to the strength of the applied magnetic field, $B°$. It also means that if a nucleus has a relatively large magnetogyric ratio, then ΔE is correspondingly large.

3.2.1.3 .Larmor precession and absorption of electromagnetic radiation by a nucleus

When a nucleus of spin ½ face a large magnetic field, this nucleus in lower energy state align themselves with the direction of the magnetic field (Z direction) and spin on its own axis. In the presence of a magnetic field, this axis of rotation precesses about the magnetic field direction like gyroscopes. This behavior is termed as Larmor precession.

The frequency of Larmor precession is proportional to the applied magnetic field strength as defined by the Larmor frequency, $\omega_{\circ}$ (also called resonance frequency) and a relationship that is mathematically described by Larmor equation-

$$\omega_{\circ} = \gamma B°$$

where γ is the gyromagnetic ratio and $B°$ is the strength of the applied magnetic field. The Larmor frequency is identical to the transition frequency. The potential energy of the precessing nucleus is given by;

$$E = -\mu B^{\circ} cos\theta$$

where θ is the angle between the direction of the axis of nuclear rotation and the applied field. If the energy is absorbed by the nucleus, then the angle of precession, θ, will change. For a nucleus of spin 1/2, absorption of radiation flips the magnetic moment so that it opposes the applied field (the higher energy state). It is also note that, only a few numbers of target nuclei are in the lower energy state and thus can adsorb radiation. When these nuclei get excited there is a possibility that, the populations of the lower and higher energy states will become equal. If this occurs, then the spin system will be saturated which means there will be no further absorption of radiation.

3.2.1.4 Relaxation processes

Transitions between adjacent spin levels can be induced by the application of a radiofrequency (RF) pulse to the sample placed in the magnetic field. An RF pulse is a magnetic field, the direction of which is oscillating at the Larmor frequency of the specific nuclei under study. In the NMR spectrometer when the RF pulse is applied with the frequency of precession of the precessing spins, a simple rotation of the net magnetization vector results. (Rotation of magnetization into the XY plane is a "90° pulse". The dephasing of the components of magnetization in the XY plane starts to occur straight away, as does the regrowth of magnetization in the z-direction).

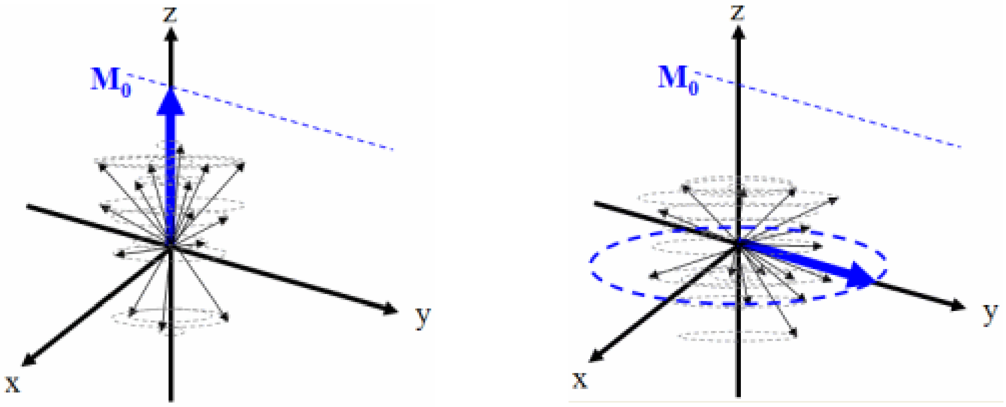

Figure 3. 1: Left: thermal equilibrium; right: immediately after a 90° RF pulse. Adapted from [15].

When RF pulse is switched off, the number of spins in each state will return to the equilibrium population in a process known as NMR relaxation. There are two major relaxation processes; spin - lattice (longitudinal) relaxation and spin - spin (transverse) relaxation.

3.2.1.4.1 Spin-lattice relaxation (T1) : Nuclei in an NMR experiment are in a sample. The sample in which the nuclei are held is called the lattice. Nuclei in the lattice are in vibrational and rotational motion, which creates a complex magnetic field. The magnetic field caused by the motion of nuclei within the lattice is called the lattice field. This lattice field has many components. Some of these components will be equal in frequency and phase to the Larmor frequency of the nuclei of under study. These components of the lattice field can interact with nuclei in the higher energy state, and cause them to lose energy (returning to the lower state). The energy that a nucleus loses increases the amount of vibration and rotation within the lattice (resulting in a tiny rise in the temperature of the sample).The relaxation time, T_1 (the average lifetime of nuclei in the higher energy state) is dependent on the magnetogyric ratio of the nucleus and the mobility of the lattice. As mobility increases, the vibrational and rotational frequencies increase, making it more likely for a component of the lattice field to be able to interact with excited nuclei. However, at extremely high mobilities, the probability of a component of the lattice field being able to interact with excited nuclei decreases.

3.2.1.4.1 spin-spin relaxation (T2) : Spin - spin relaxation describes the interaction between neighbouring nuclei with identical precessional frequencies but differing magnetic quantum states. In this situation, the nuclei can exchange quantum states; a nucleus in the lower energy level will be excited, while the excited nucleus relaxes to the lower energy state with a characteristic time of T_2. There is no net change in the populations of the energy states, but the average lifetime of a nucleus in the excited state will decrease. This can result in line-broadening. Field inhomogeneity can cause an additional dephasing of the spins, leading to an effective transverse relaxation time T^*_2. The effects of the inhomogeneity of the field on T_2 can be minimized by using specific pulse sequences to measure the relaxation time. For T_2 relaxation time the Carr–Purcell–Meiboom–Gill pulse sequence is used to reduce the constant pulse effects of diffusion.

3.2.1.5 Spin-echo, T_2 measurements, and diffusion

In a perfectly homogeneous magnetic field, the T_2 relaxation time constant can be measured directly from the free induction decay in the time domain or the full width at half height of the resonance in the frequency domain. The magnetic field, however, is never perfectly homogeneous. Each microscopic volume element of the sample resides in a slightly different magnetic field and therefore the offset frequencies of the resonance in each volume element are slightly different from one another. The net effect on the spectrum of the entire sample is that the NMR resonances are broader than what one would expect from the T_2 relaxation process alone. The distribution of offset frequencies due to magnetic field inhomogeneity is referred to as inhomogeneous broadening. In an inhomogeneous magnetic field, the FID decays faster, with a time constant T_2^* where $1/T_2^*$ has a contribution from the natural relaxation rate, $1/T_2$, of the resonance and that due to the field inhomogeneity. In other words, when a sample is in an inhomogeneous magnetic field, the resonances are homogeneously broadened by the natural T_2 relaxation process and inhomogeneously broadened by the non-uniform magnetic field. The measurement of T_2 relies on separating the homogeneous broadening from the inhomogeneous broadening.

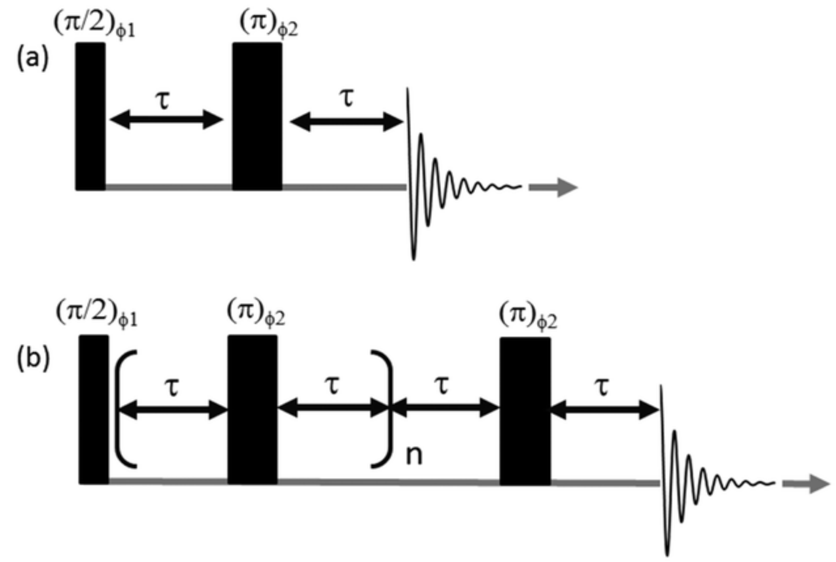

Figure 3. 2: a) Hahn spin-echo, b) CPMG sequence. Adapted from [16].

One of the first pulse sequences typically introduced in NMR is the spin echo or Hahn echo [17]. This sequence consists of a 90° pulse followed by a delay, τ, during which offsets frequencies evolve. An 180° pulse is then applied after which another period of time, τ is allowed where offsets continue to evolve, producing an echo at 2τ. The spin echo sequence has the ability to refocus the distribution of offset frequencies due to magnetic field inhomogeneity (inhomogeneous broadening) however, it cannot refocus the natural distribution of frequencies due to the T_2 relaxation process (homogeneous broadening). It would seem as if the spin echo sequence has the ability to separate out the homogeneous broadening from the inhomogeneous broadening and therefore should be able to be used to measure the T_2 relaxation time constant. But the simple Hahn echo is not always suitable for T_2 measurements as the intensity of the echo depends on the degree of inhomogeneous broadening. This is so because of molecular diffusion. During the one-second τ delays, molecules move from one volume element to another in the sample and therefore change their offset frequencies over the course of the measurement. The net result for the entire sample leads to the attenuation of the echo amplitude due to destructive interference in the time domain signal from the sum of all volume elements. The loss in echo intensity is worse the more inhomogeneous the field. The simple Hahn echo would be expected to work as a means to measure T_2 only in cases where the diffusion is insignificant with respect to τ. To reduce this problem, the Carr Purcell Meiboom Gill (CPMG) sequence was introduced for T_2 relaxation time measurement with the negligible effect of diffusion. In the CPMG sequence [18] [19], a train of Hahn echoes is used where the τ delays for each echo are chosen sufficiently short such that diffusion is not a problem. The T_2 is calculated from a series of spectra collected as a function of the number of echoes in the train based on the overall time between the initial 90° pulse and the collection of the signal.

3.2.1.6 Relaxation Mechanism

Spontaneous T_1 relaxation of spin ½ nuclei, i.e., relaxation in the absence of external influences, is essentially absent. For T_1 relaxation to occur there must be magnetic field fluctuations in the XY direction. Such fluctuations are most effective when they occur at the Larmor precession frequency. T_1 relaxation is thus field dependent since frequency varies with the field. T_2 relaxation is caused by fluctuations in any direction.

The principal source of fluctuating magnetic fields in most molecules is molecular motion. There are several physical processes by which molecular motions can influence nuclear relaxation:

- Direct interactions with nearby magnetic nuclei (Dipole-dipole relaxation)
- Chemical shift effects
- Quadrupole-electric field gradient interaction (Electric-quadrupole interaction)

- Rapid modulation of *J*-coupling (Scalar relaxation).
- Spin-rotation interaction

Below are the summary of the 2 principal relaxation mechanism those we will use in this chapter -

3.2.1.6.1 Dipole-Dipole Relaxation: Coupling between magnetic nuclei is of two types: the scalar (*J*) coupling is the result of polarization of the electrons by the nuclear spins. The direct dipole-dipole coupling interaction is very large (often kilohertz) and depends principally on the distance between nuclei and the angular relationship between the magnetic field and the internuclear vectors. This coupling is not seen in mobile solutions because it is averaged to zero by tumbling of the molecule. However, as the molecule tumbles in solution the dipole-dipole coupling is constantly changing as the vector relationships change. This creates a fluctuating magnetic field at each nucleus. To the extent that these fluctuations occur at the Larmor precession frequency, they can cause nuclear relaxation of nearby nuclei. Since the proton has the highest magnetic dipole of common nuclei, it is the most effective nucleus for causing Dipole-Dipole Relaxation. It is the principal relaxation pathway for protons in molecules containing contiguous protons, and for carbons with directly attached protons.

3.2.1.6.2 Quadrupolar Relaxation: This mechanism operates for spin >½ nuclei only, and only for nuclei which are not at the center of tetrahedral or octahedral symmetry. Spin ½ nuclei can be considered to have spherical charge distributions, but for spin >½ nuclei the charge distribution has the shape of an oblate or prolate spheroid. Electric field gradients in such molecules exert a torque on the quadrupolar nuclei. Tumbling of the molecule can then initiate transitions among the spin states (there is ‘friction’ between the nucleus and the surrounding electrons, the ‘quadrupole coupling constant’). The effectiveness of this relaxation mechanism is critically dependent on this coupling. If the electric quadrupole moment of a quadrupole nuclei is small (as for ^{2}H and ^{6}Li, both with $I = 1$) the nucleus behaves almost like a spin ½ nucleus (i.e. there is only a small deviation from spherical symmetry), if it is large the nucleus can have very short T_1, and observation can be very difficult, and spin-spin splitting to the nucleus cannot be observed. Quadrupolar relaxation of a nucleus can also have effects on nearby magnetic nuclei since rapid relaxation can either broaden or entirely remove *J*-coupling between the two nuclei.

3.2.2 Solvent relaxation NMR

In a relaxation measurement, the proton of the water molecule in a particulate dispersion undergoes fast exchange between a bound water molecule on the surface of the particle and an unbound state in free solution. The relaxation rates in these two different environments are different due to the mobility of the water molecule; and the presence of nuclei of different magnetic behaviour [8]. Typically, the proton in the bound state undergoes faster relaxation (R_{2bound}) than the proton in the free state (R_{2free}). As long as fast exchange occurs between two environments, the total relaxation rate of the system is the average relaxation rate of the proton weighted by the time fraction the proton spends in each environment. Thus, the single relaxation rate, R_2, for such fast exchange limit is calculated from the following equation:

$$R_2 = R_{2bound} \cdot p_b + R_{2free}(1 - p_b) \tag{1}$$

here, p_b is the time-averaged probability of randomly chosen proton on the particle surface. This is called 'bound fraction probability' and is related to the fraction of proton at both environments. For the sake of simple presentation of relaxation data, the specific relaxation rate, R_{2SP}, is normalized to the relaxation rate of the background solvent ($R_2°$) to enhance the relaxation rate change in the system (R_2) [7].

$$R_{2SP} = \frac{R_2}{R_2^{\circ}} - 1 \tag{2}$$

In the case of bare particles, an increase in R_{2SP} means that there is a greater percentage of bound water (i.e. more efficient relaxation behaviour of water nuclei). During polymer adsorption, the enhancement in R_{2SP} arises from the fact that more water becomes trapped between the polymer-particle interfaces, thereby and decreasing the mobility of the water molecules, or increasing their retention time at the interfaces [11].

3.3 Experimental Section

3.3.1 Materials

Polymers: The poly (vinyl pyrrolidone) (PVP) samples used in this project had average molecular weights of 4×10^4 and 36×10^4 g/mol and were purchased from Polysciences Inc. and Sigma-Aldrich respectively. All polymers were used as supplied. Stock PVP solutions were prepared with deionized water having a resistivity of 18MΩ cm^{-1} and mixed overnight with Haul mixer before further dilution. For a polymer adsorption study, known amounts of PVP, particles, and water were mixed to give specific particles and polymer concentration. The mixtures were then allowed to equilibrate for a minimum of 12 hours through Haul mixer before taking NMR measurements.

Particles: Silica, silica-titania core-shell (STCSNP) and silica-titania hollow nanoparticles (STHNP) used here were synthesized at University of Greenwich. Silica nanoparticles were prepared from tetraethyl orthosilicate through the sol-gel process in presence of ammonium hydroxide. Silica-titania core-shell nanoparticles (STCSNP) were prepared from silica nanoparticles through sol-gel reaction of titanium isopropoxide (TTIP) on the silica surface.

Table 3. 3: The Size distribution and surface area of silica, silica-titania core-shell nanoparticles and silica-titania hollow nanoparticles.

Particles	**Silica NPs**	**Core-shell NPs**	**Hollow NPs**
Surface area (m^2/g)	90 ± 5.7136	180 ± 6.6475	295 ± 7.0231
Particle size, (nm)	30 ± 0.043	50 ± 0.062	50 ± 0.067

Then silica-titania hollow nanoparticles (STHNP) were synthesized upon sonication of core-shell particles in presence of dilute ammonium hydroxide solution. The details of the synthesis have been discussed in chapter 2. All samples were dialyzed for 3 consecutive days with deionized water (18MΩ cm^{-1}) and filtered through glass wool before using for polymer adsorption study. During PVP adsorption study, the STCSNP samples with PVP were needed to shake before taking NMR measurement. The size and surface area measurements of three different structured nanoparticles are listed in Table 3.1.

3.4 Characterization

3.4.1 Solvent relaxation NMR

The NMR spectrometer (Acorn Drop™) used here is a temperature controlled bench-top device supplied by Xigo Nanotools, Inc., Bethlehem, USA. Acorn Drop™ operates at 13 MHz with 90° pulse length of 5.9 µs and 11.2 µs for 180° were used for all measurements. The spin-spin relaxation time of water was measured using the CPMG (Carr–Purcell–Meiboom–Gill) [18] [19] pulse sequence with a spacing of 1 ms between 180° pulses (i.e., τ = 0.5). The recycle delay of at least 5T_1 (spin-lattice relaxation) was maintained between 4 consecutive scans for full recovery of magnetization. The transverse relaxation time (T_2) was calculated from each magnetization relaxation decay curve, $M_y(t)$, where each curve was fitted against time t to the following equation using a nonlinear least-squares algorithm:

$$M_y\,(t) = M_y(0)e^{-(\frac{t}{T_2})} \qquad (3)$$

Where, $M_y(0)$ denotes the immediate transverse magnetisation after 90° pulse sequence and t is the relaxation interval.

For hollow nanoparticles, where the two surfaces are exposed to the liquid medium, the measured NMR signal will be the sum of the signal of water from the inner surface of the hollow cavity, the outer surface of the particle and the signal from the free water in bulk. Here, it is assumed that the inner and outer volumes are not exchanging on the NMR timescale but that the water with these volumes is in the fast exchange between surface and bulk. Hence the magnetization decays will be double exponential.

$$M(t) = M_{outer}\exp(-R_{outer}t) + M_{inner}\exp(-R_{inner}t) \qquad (4)$$

where $M(t)$ denotes the total signal. R_{inner} and R_{outer} are the average relaxation rate for the inner and outer surfaces of hollow nanoparticles respectively. M_{inner} is the signal from the inner surface and M_{outer} , from the outer surface.

3.5 Result and Discussion

3.5.1 Relaxation behaviour of particles in aqueous environment

To understand the relaxation behaviour and surface properties of bare silica, silica-titania core-shell (STCSNP) nanoparticles and silica-titania hollow nanoparticles (STHNP), transverse relaxation time, more specifically, specific relaxation rate (R_{2SP}) were measured.

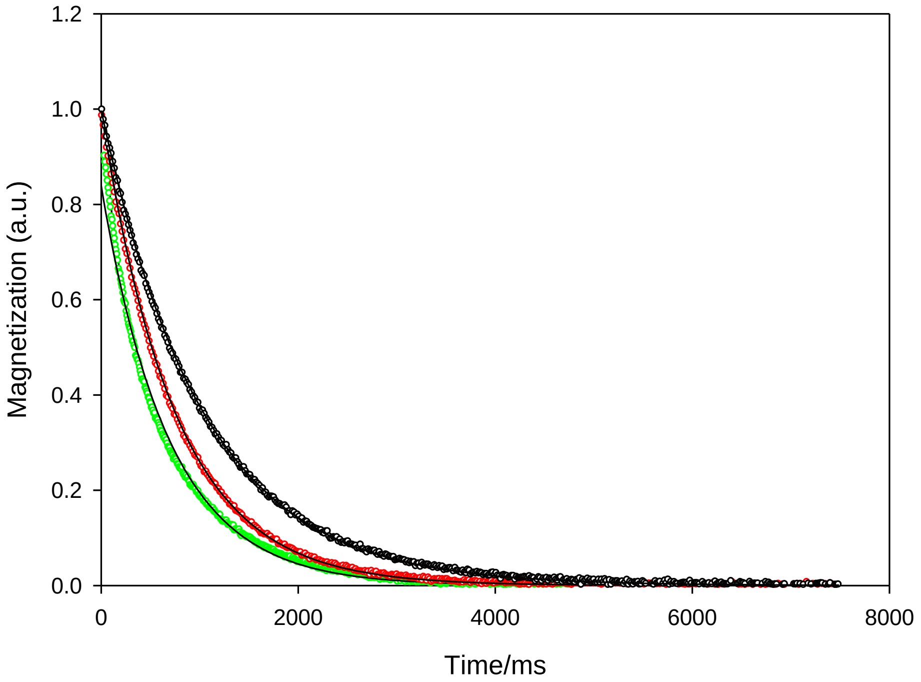

Figure 3. 3: CPMG decay curves for Silica (●), STCSNP (●), STHNP (●) at fixed volume fraction of 0.0024.

Figure 3.3 shows the normalized CPMG decay curves for three different colloidal dispersions (silica nanoparticles, STCSNP and STHNP dispersed in water) together with the fits from the eq 3. The hollow and core-shell nanoparticles cause the magnetization to decay slower than the silica nanoparticles due to the increased number and correlation time of water molecules associated with the particle surface [7]. Therefore the relaxation time follows as; silica>STCSNP>STHNP and is calculated by eq 3. It is also noted that the CPMG curve of hollow nanoparticles has the distinguishing feature than the core-shell and silica nanoparticles, that means the black fit did not go through the experimental data points very well for hollow nanoparticles. For better presentation, the data from the CPMG curve of hollow nanoparticles were fitted in the semi-log scale (3.5-3.8). The raw experimental data was not adequately described by single exponential fit (figure 3.5 and 3.6), but was substantially better when analyzed in terms of a double exponential fit to eq 4 (Figure 3.7 and 3.8). Therefore it is concluded that the two components arise from the water adsorbed at the inner and outer surfaces of the hollow nanoparticles. The fitting parameters for a double exponential fit are listed in Table-3.2. Figure-3.4 shows the respective R_{2A} and R_{2B} values based on the best fitting for hollow nanoparticle samples as a function of concentration. Surprisingly, the double exponential fit was only required for hollow nanoparticle dispersions at low concentrations.

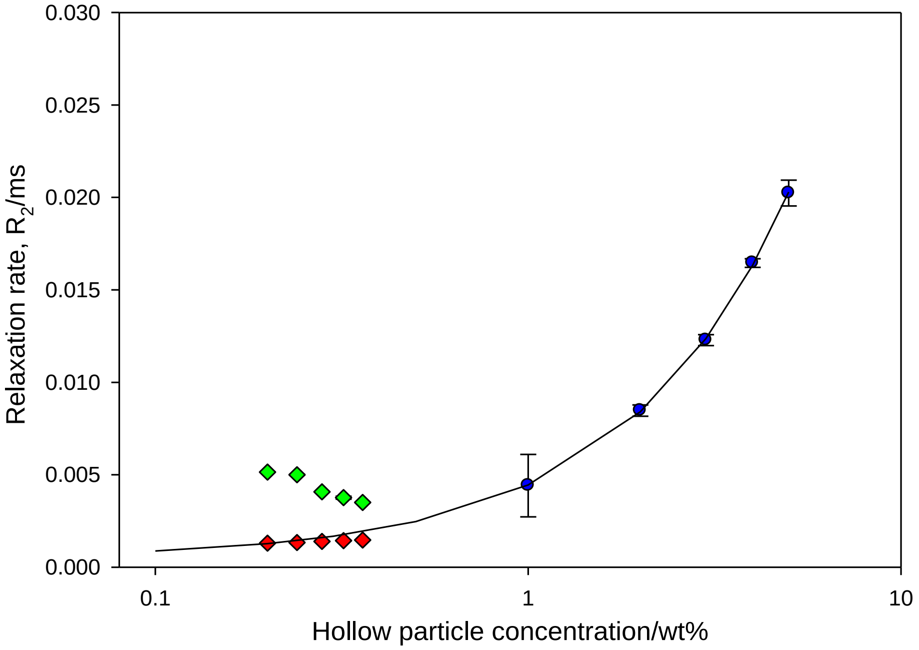

Figure 3. 4: Variation in R2 (●) components for hollow nanoparticles; (◆) fast rate T2A, increase with volume fraction (◇) slow rate T2B, decrease with volume fraction. (——), Linear prediction.

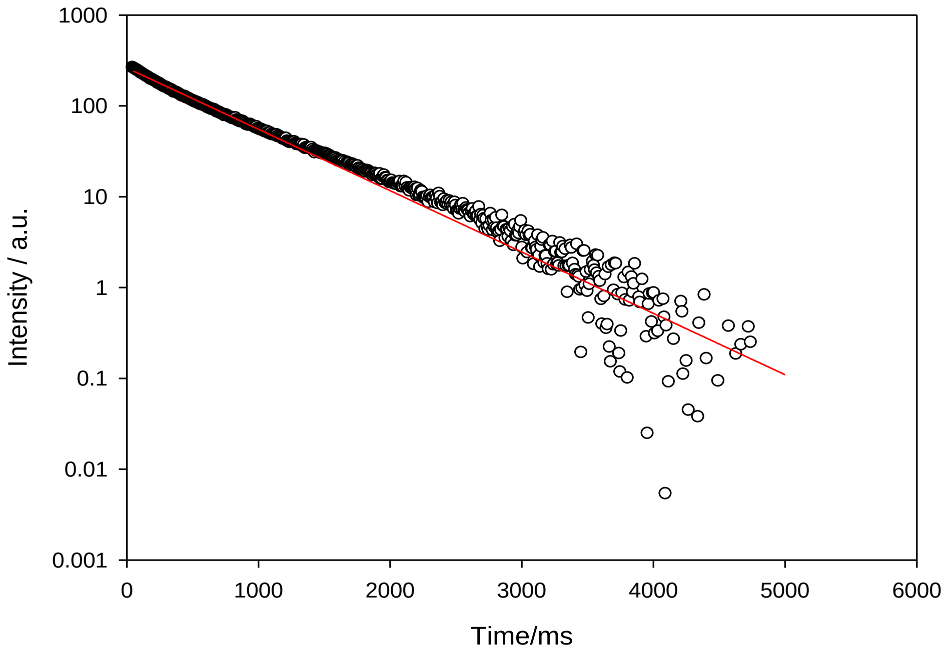

Figure 3. 5: Relaxation decay curve for the hollow nanoparticle. The solid line (red) through the experimental data (O) is the single exponential fit.

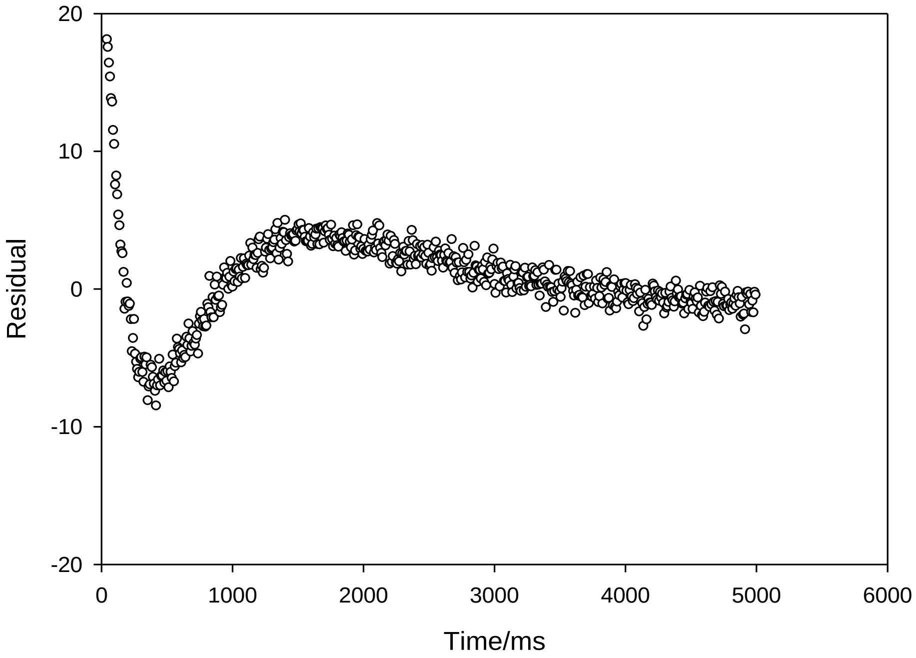

Figure 3. 6: Residual (O) plot for the hollow nanoparticle calculated from the single exponential fit. The difference between fit and the data.

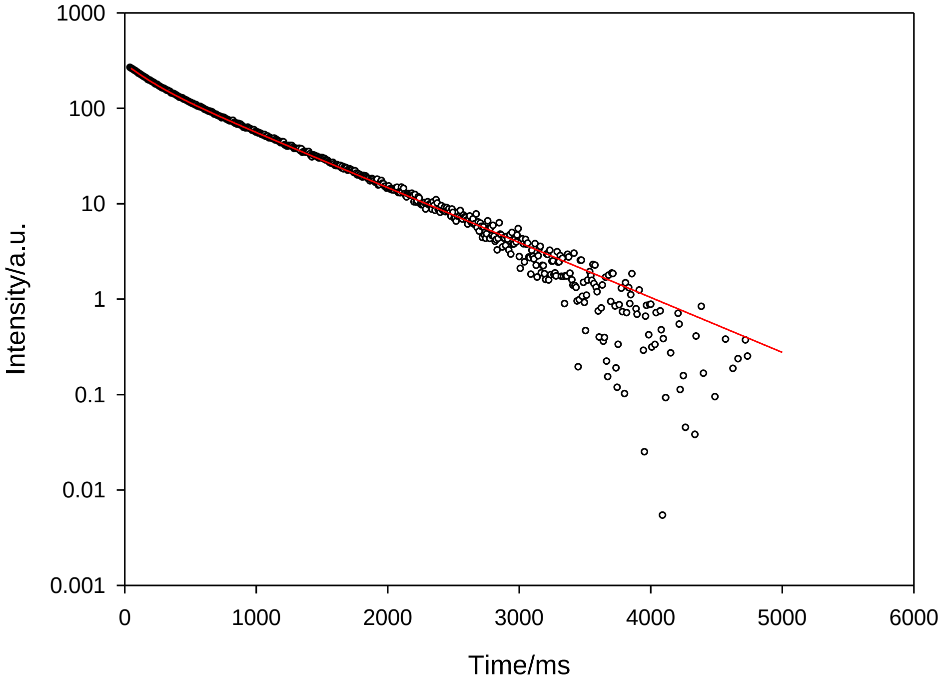

Figure 3. 7: Relaxation decay for hollow nanoparticles. The solid line (red) through the experimental data (O) is the double exponential fit.

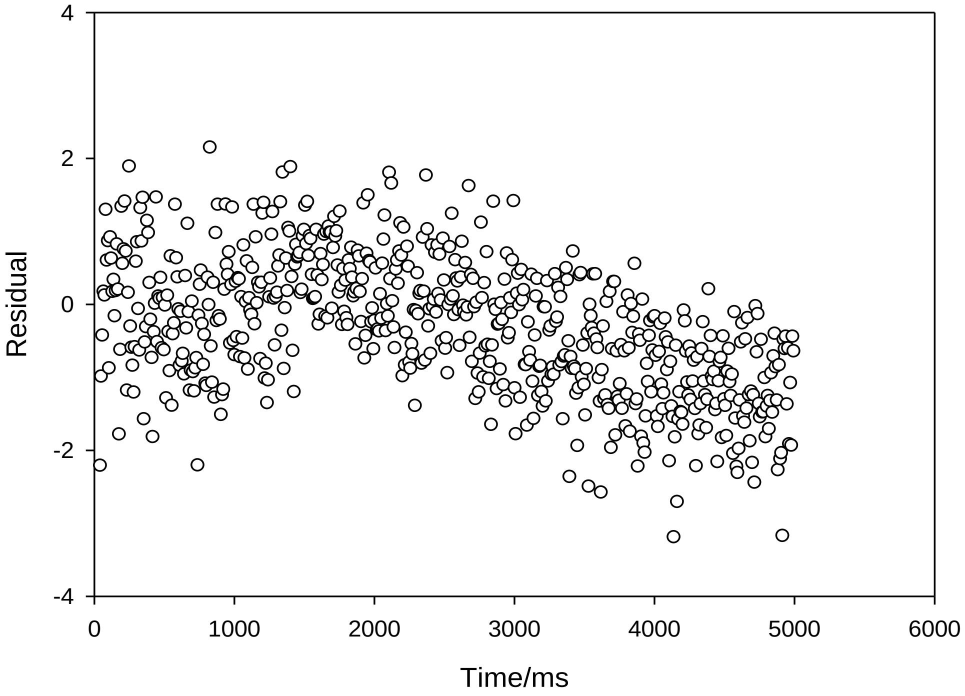

Figure 3. 8: Residual (O) plot for the hollow nanoparticle calculated from the double exponential fit. The difference between fit and the data.

Table 3. 4: T2 relaxation data of silica-titania hollow nanoparticles at fixed volume fraction of 0.0024.

Parameters	T_{2A}	Y_A	T_{2B}	Y_B
Hollow nanoparticle dispersion in water	748.9356 ± 2.7E-06	209.6668 ± 0.6	199.9433 ± 2.3E-05	92.89645 ± 0.9

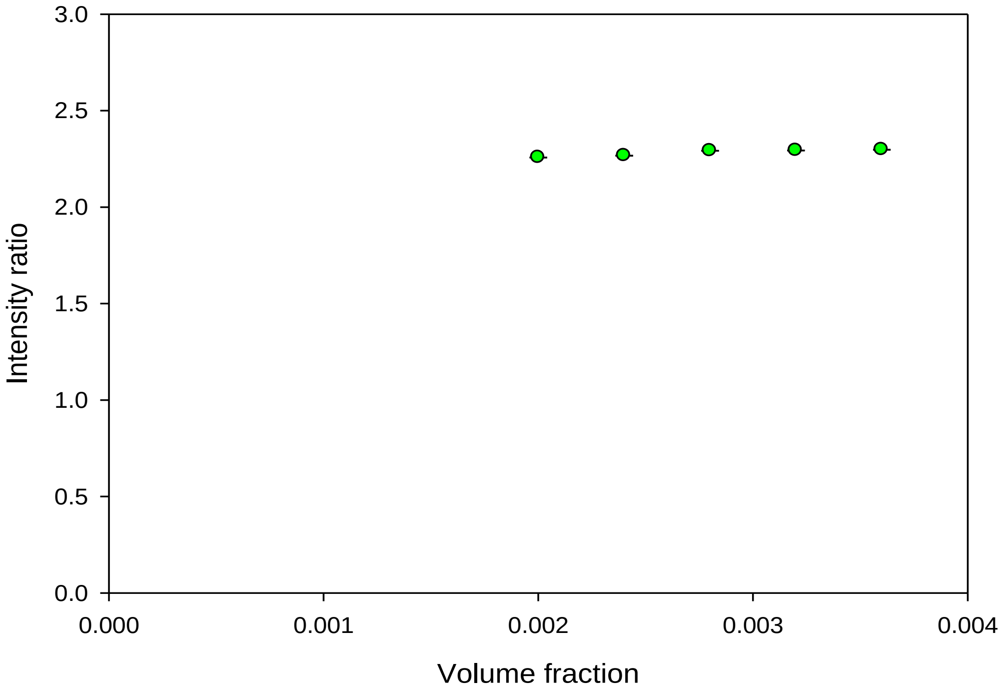

Figure 3. 9: Intensity ratio differences as the function of volume fraction.

The intensity ratio for these two components was found to be constant at low volume fraction, i.e. to not vary with surface area (Figure 3.9). At higher concentration, the components (R_{2A} and R_{2B} values) of the double exponential fit appear to coalesce into an effective, single exponential decay (fig 3.4). This is an unexpected observation, and is most likely associated with the rate of exchange between the water molecules constrained within the pore, adsorbed to the outer surface and the bulk phase. Clearly, this is not fully understood and further work is required to characterize this interesting observation.

Turning the attention to higher volume fraction (concentration) dispersions the observed behaviour is less challenging to interpret. In Figure-3.10, R_{2SP} for three different structured nanoparticles are shown as a function of weight percentage of particles in aqueous dispersion, whereas Figure-3.11 shows the R_{2SP} of three colloidal particle surfaces as a function of the particle surface area. Surface area for three different colloidal particles was calculated from the average particle radius (measured from scanning-transmission electron microscopy) and volume fraction. In both figures, relaxation rate for the deionised water was used for R_2° value in eq 2 to calculate the R_{2SP} value. Over the concentration range studied, the linear relationship can be seen for each nanoparticulate system which validate the fast exchange model of eq 1 demonstrating the fast proton exchange between bound and unbound water molecules [20] [7] [14].

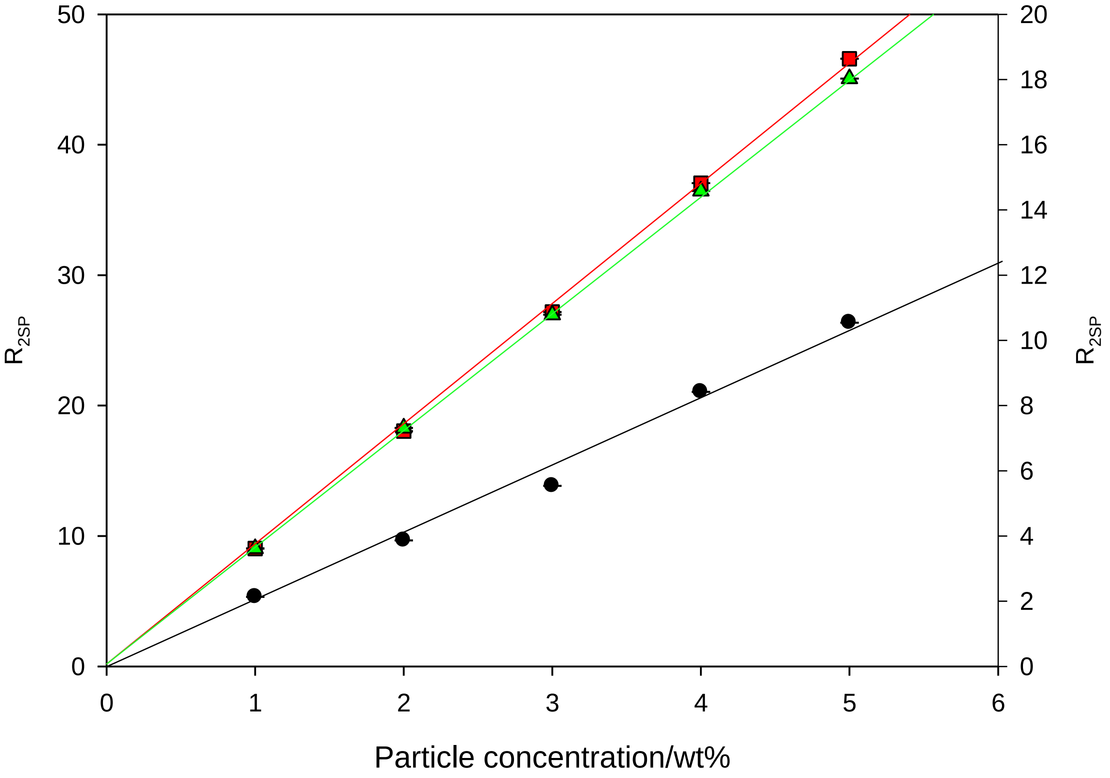

Figure 3. 10: Relaxation rate of silica (●), STCSNP (🟥) and STHNP (▲) normalized with deionized water in absence of PVP.

Moreover, in Figure-3.11, the slope of the R_{2SP} as a function of surface area is large in the case of core-shell and hollow nanoparticles and smaller that of the bare silica nanoparticles. According to T. Cosgrove *et al* this increasing trend of the slope due to increasing amount of bound water molecule in the nanoparticles surfaces per unit area or increasing immobility of bound water molecules. Furthermore, it indicates the hydrophilic nature of three different nanoparticles where core-shell and hollow nanoparticles are more hydrophilic than bare silica particles. This surface hydrophilicity could be the consequences of surface chemistry and porosity of the different nanoparticles [7]. Table-3.1 presents the nitrogen physisorption data of these three different colloidal particles. From the table 3.1, it can be seen that hollow and core-shell nanoparticle have more surface area than silica nanoparticles which mean more available surface for water molecule on the surfaces. It is worth to say, though hollow nanoparticles have more surface area than core-shell particles, but both particles have got an almost same increasing trend of slope and R_{2SP} enhancement. It may be due to the presence of

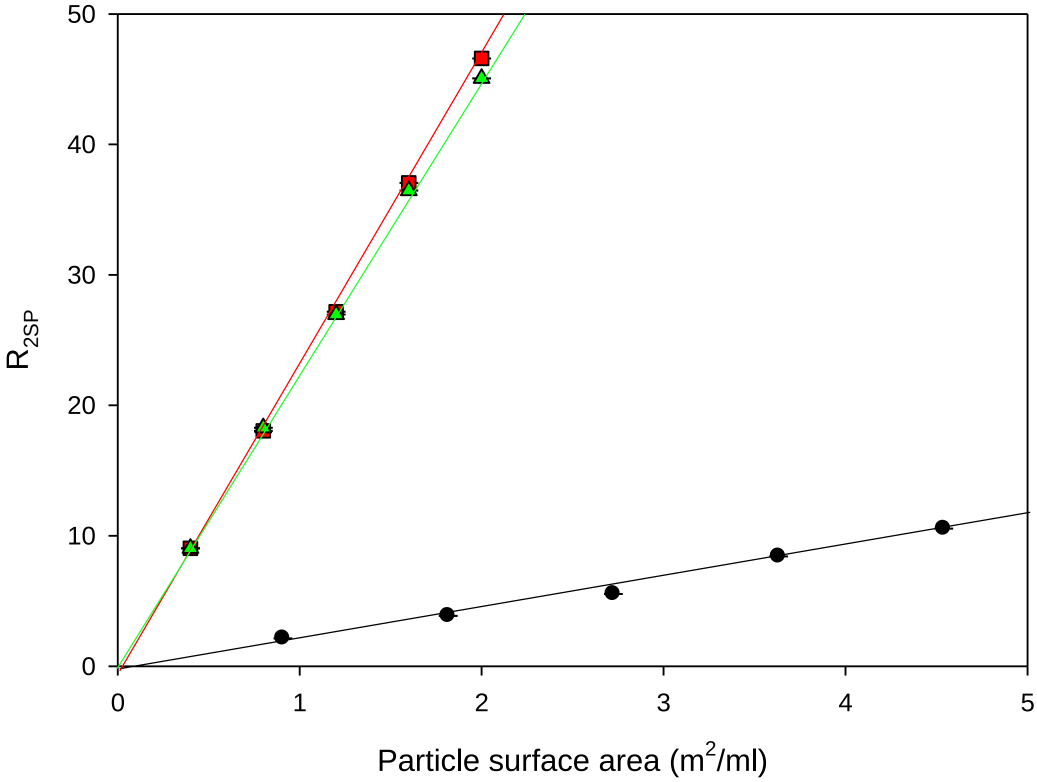

Figure 3. 11: R2SP was measured for water dispersion of silica (●), STCSNP (🟥) and STHNP (▲) as the function of particle surface area. The surface area used for three different colloidal particles were calculated from the average particle radius (measured from scanning-transmission electron microscopy) and the volume fraction.

large hollow cavity of hollow nanoparticles with the association of large pore size and presence of quadrupole nuclei of titanium on core-shell particle surface and mixed silica-titania shell on the hollow nanoparticle surface. In the case of hollow nanoparticles, the water molecule can be adsorbed on two different surfaces, namely inner and outer surfaces, which allow more and more water molecules to adsorb in the vicinity of hollow nanoparticle and increase the overall relaxation rate. On the other hand, quadrupole nucleus of Ti on the titanium layer of core-shell particles create electric quadrupole moment and cause the rapid quadrupole relaxation with the dipolar solvent [21] [22]. And dipole-dipole coupling constant is usually less prominent than dipole-quadrupole coupling constant which leaves us to consider quadrupole relaxation mechanism plays a key role here [8]. And another reason for increasing trend of slope in core-shell structure may be due to the presence of small pores (suggested by nitrogen physisorption data) on their surfaces available for water molecules.

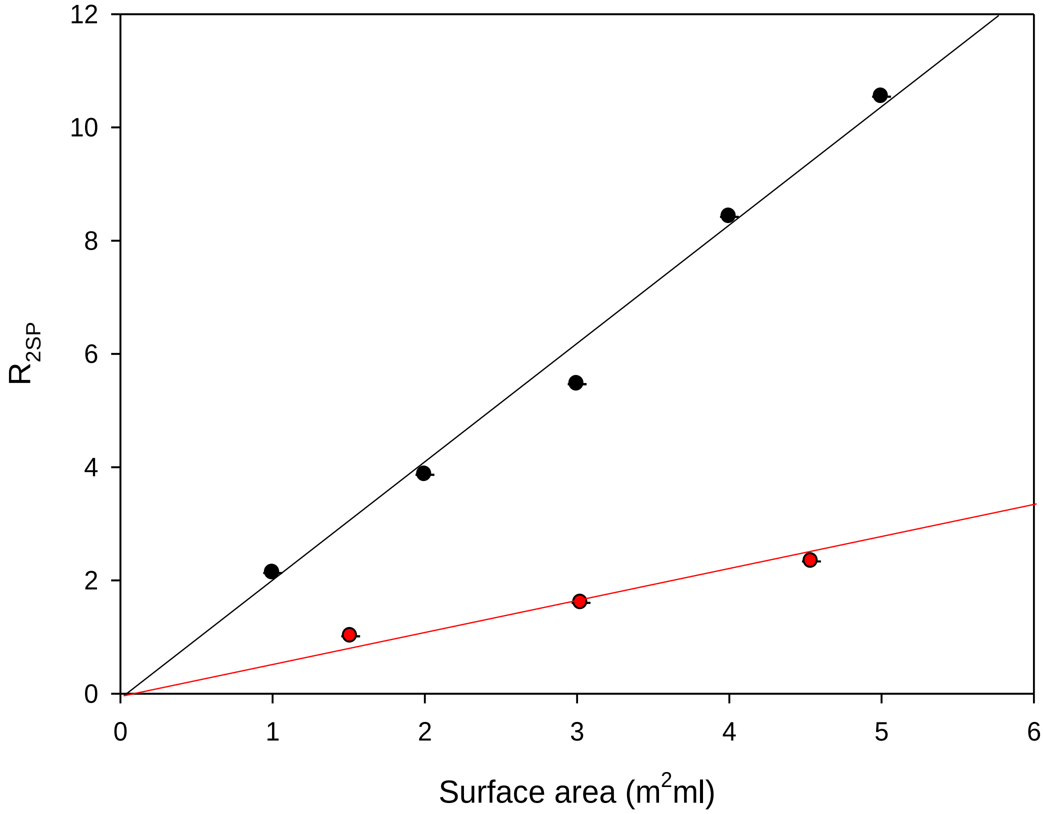

Figure 3. 12: R2SP measurement of silica (●) and Ludox TM-50 (●) normalised with deionized water.

Figure-3.12 shows the difference in relaxation enhancement of laboratory synthesized silica nanoparticles and marketed product Ludox TM-50 colloidal silica dispersion in water. Though both silica samples show a linear dependence of R_{2SP} upon the surface area available in the dispersion, the lab synthesized silica nanoparticles have higher relaxation rate enhancement. This may be again due to the presence of mesopores in lab synthesized silica surfaces offering more spaces for the water molecule.

3.5.2 PVP adsorption on particle surfaces:

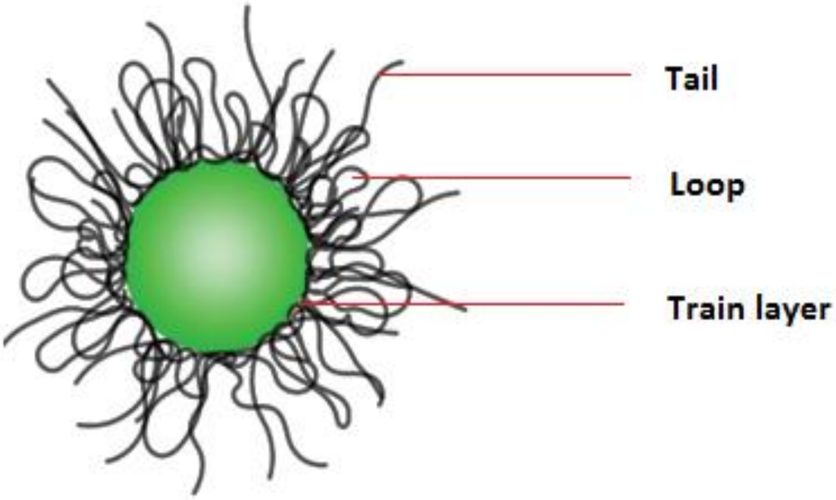

Figure 3. 13: Schematic representation of different conformations of adsorbed polymer at adsorption site. Adapted from [11].

Adsorption of PVP onto bare silica, silica-titania nanoparticles (STCSNP) and silica-titania hollow nanoparticles (STHNP) were examined by solvent relaxation NMR and light scattering technique. These two techniques have different sensitivity to a different layer of the adsorbed polymer (Figure 3.13). Dynamic light scattering (DLS) is a hydrodynamic technique that counts the fluid that flows around a particle. Upon polymer adsorption, the tails region of the polymer conformation is the main site on the particle surface that restricts the liquid flow. So DLS technique is most sensitive to the hydrodynamic size of an entire particle-polymer system where loops, but mainly tails of the polymer conformation are counted [23]. On the other hand solvent relaxation NMR counts only polymer train layer which is directly linked to the particle surface [24]. The NMR samples for the experiment were made by fixing the initial particle concentration at 3wt% and by varying the PVP amount ranging from 0.2-3 mg/particles unit area. For light scattering measurement, samples were diluted and subjected to sonication for 3 minutes before taking the measurement. Figure-3.14 shows NMR measurement for the PVP adsorption onto three different structured nanoparticles surfaces where R_{2SP} was normalized by the relaxation rate of particle dispersions of constant concentration (3wt%).

Figure 3.15 shows the NMR and light scattering measurement upon adsorption of PVP on the bare silica surface. The feature of adsorption isotherm for silica on this graph is similar to that described by Cattoz *et al* apart from the saturation point found at 1.5 mg/m^2 where they found it at 1.1 mg/m^2 of polymer added [11]. This value indicates the saturation point of polymer train

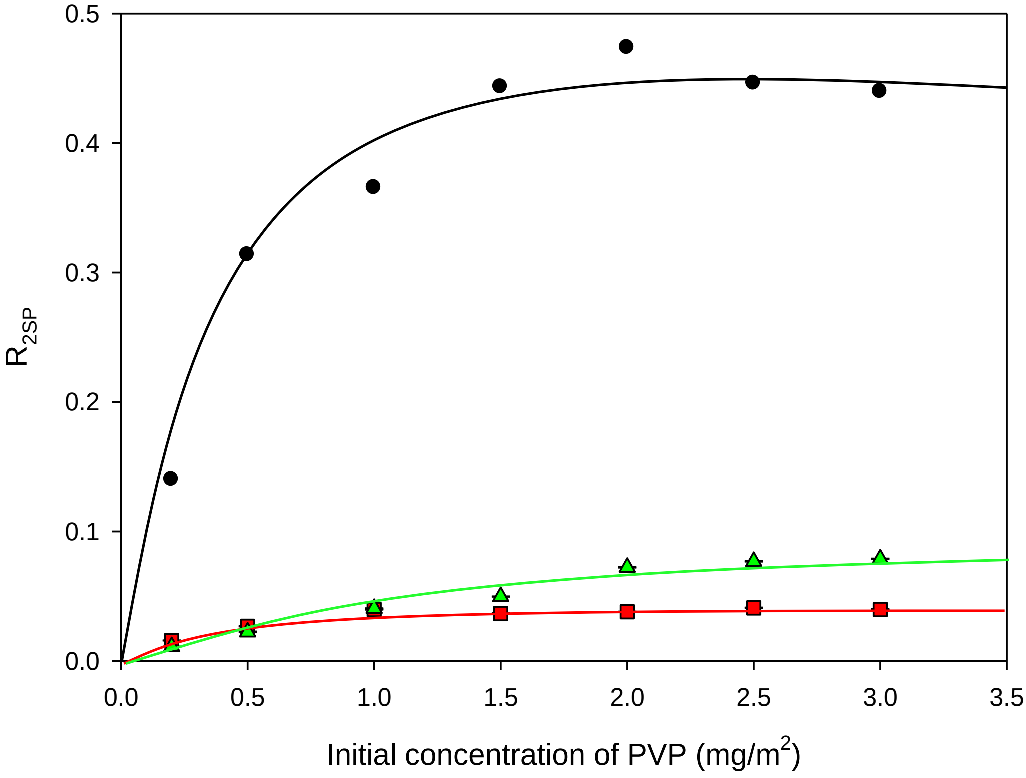

Figure 3. 14: Adsorption isotherm of PVP-40 on silica (●), STCSNP (■) and STHNP (▲). R2SP was normalized with particle concentration. Lines are a guide to the eye.

layer on the particle surfaces after that loops and tails of polymer segments developed upon further polymer addition. When the polymer is introduced to a particle dispersion, the polymer train adsorbed predominantly on the particle interfaces associate with water molecules in their vicinity and restricts the water mobility which ultimately increases the overall relaxation rate. Due to sensitivity to only near surface water molecule, NMR technique is showing sharp relaxation rate enhancement at low added polymer amount until saturation of train layer achieved, after what it gives rise to plateau value (Figure-3.15). That means there is not enough surface available in plateau level for polymer train layer formation. The layer thickness at lower PVP concentration is almost same and also proving the initial polymer adsorption in a train-like configuration. Upon addition of further polymer amount (Figure-3.15), the layer thickness increased sharply after saturation point which is

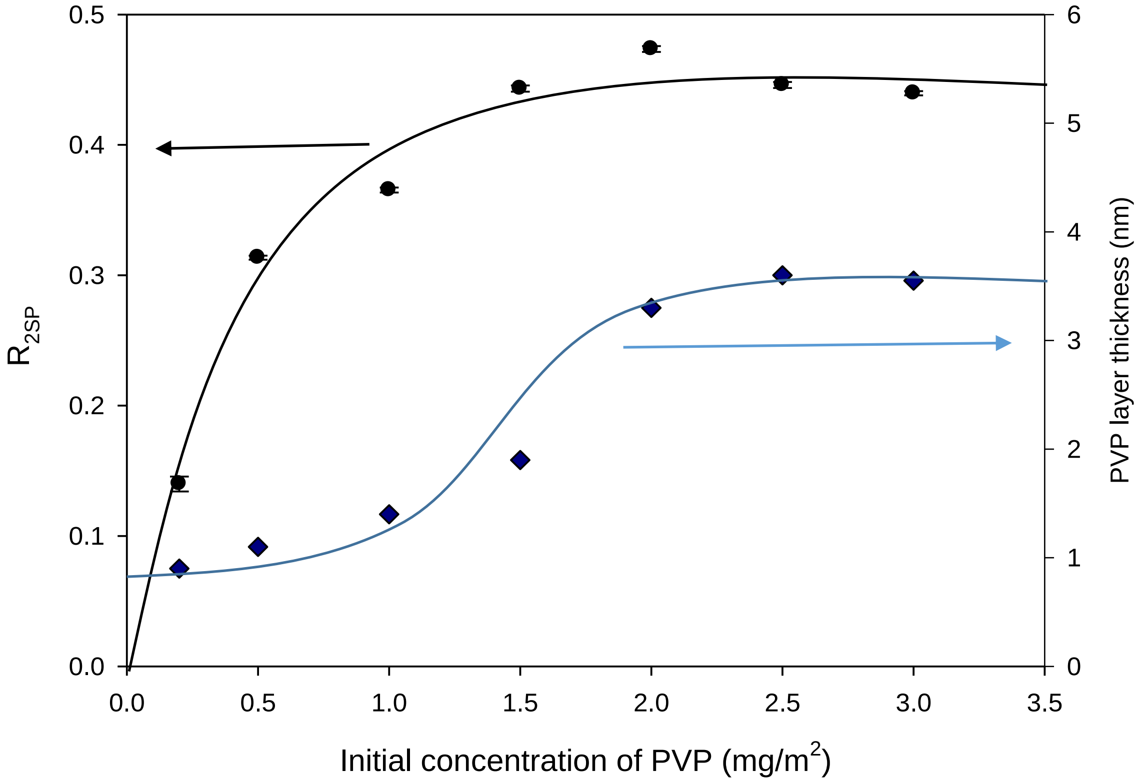

Figure 3. 15: Adsorption of PVP-40 on bare silica measured by relaxation NMR (●) (only sensitive to near surface train layer) and layer thickness (◆) (sensitive to the entire polymer-particles system) on right axis measured by light scattering technique. Lines are a guide to the eye.

an indication of the presence of access polymer to form different polymer configuration on silica surfaces (development of loops and tails). However, there may be some polymer segment exist as a unadsorbed form in the solution. Since R_{2SP} is independent of homopolymer like PVP (due to the flexibility of polymer chain), there is no significant contribution from PVP in R_{2SP} change [8]. This confirmative experiment for free polymer samples with water was also performed by solvent Relaxation NMR for verification and only slight R_{2SP} change was observed.

Figure-3.16 shows the NMR and light scattering measurements for silica-titania core-shell nanoparticles upon PVP adsorption. It indicates that R_{2SP} change upon PVP adsorption on titania surfaces is negligible which is limited to 0.01-0.04. This negligible change could be the resulted from nothing but the unadsorbed PVP at a bulk solution which means PVP was not adsorbed on titania surface. This was also revealed from noisy data of light scattering technique which is not consistent with relaxation data. This weaker affinity of PVP on titania rich surface

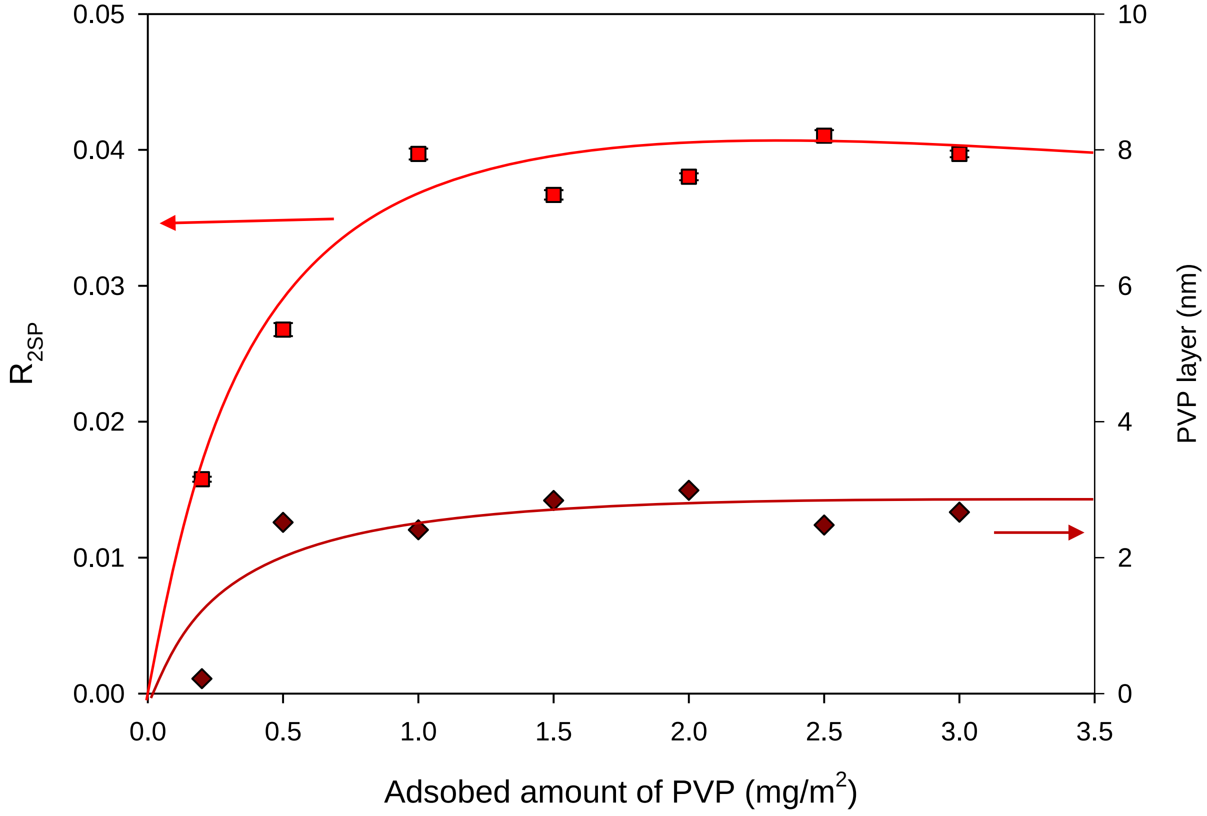

Figure 3. 16: Adsorption of PVP-40 on STCSNP measured by relaxation NMR (🟥) (only sensitive to near surface train layer) and layer thickness (◆) (sensitive to the entire polymer-particles system) on right axis measured by light scattering technique. Lines are a guide to the eye.

could be the consequences of three important facts. Firstly, it may be due to the strong hydrophilicity of PVP molecule and it is hard for titania on STCSNP surface to attract PVP from water system [25]. Secondly, in the system of polymer-water-titania surfaces, titania acts as a weak Lewis acid site for carbonyl group (Lewis base) on the pyrrolidone ring of PVP, thus have the weaker strength to attract/rarely attract PVP. On the other hand, silanol group of silica can act as a strong Lewis acid sites for a carbonyl group, thus bind with more and more PVP in their vicinity [26]. Thirdly, the presence of the quadrupoles in the titanium nuclei interferes to the overall measured dipole relaxation thus screening the effect of polymer adsorption [8]. If the R_{2SP} change between silica and core-shell particles is compared, it is also observed from the Figure 3.15 and 3.16 that, R_{2SP} enhancement for core-shell particles upon PVP adsorption is much lower than silica particles (around 0.1-0.5 for silica and 0.01-0.04 for core-shell particles over the range of PVP adsorption studied). This is again the indication of no PVP

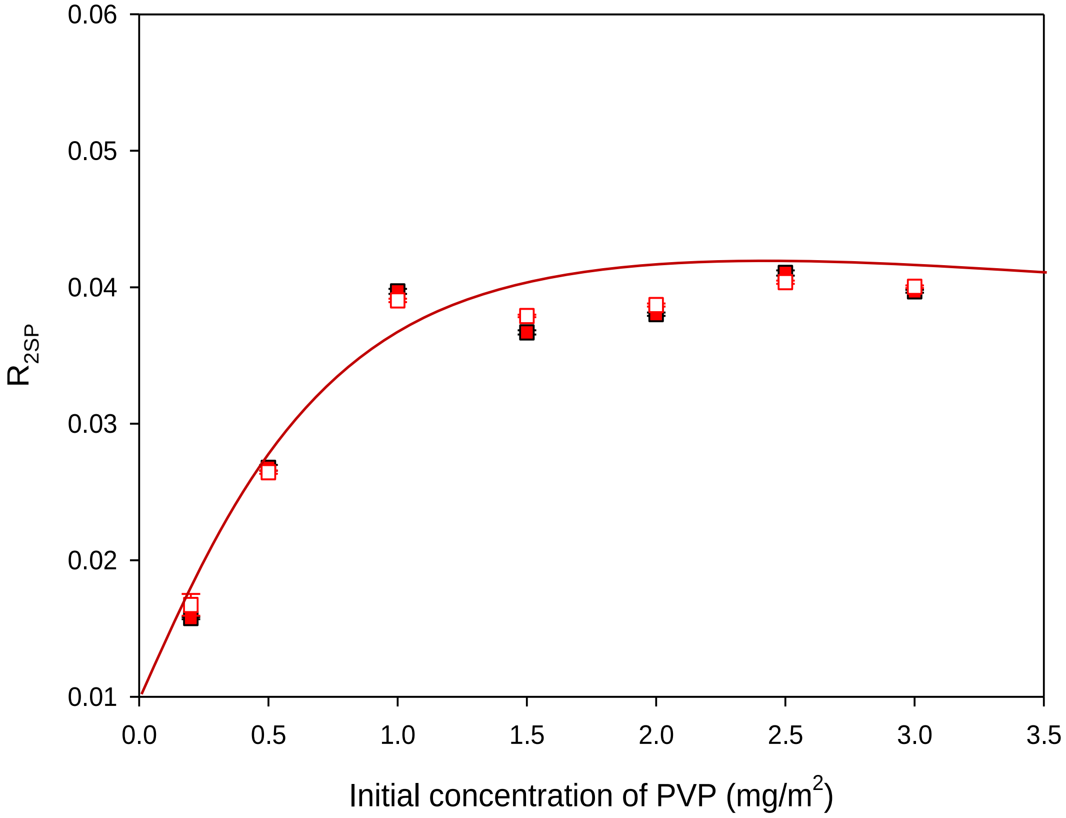

Figure 3. 17: Comparison of PVP-40 (■) and PVP-360 (□) adsorption on STCSNP surface. R2SP was normalized with STCSNP concentration. The line is a guide to the eye.

adsorption on the surface of the STCSNP. The experiment of PVP adsorption on core-shell particles was also conducted with high molecular weight PVP-360 (Figure-3.17). Figure-3.17 shows also no significant change in relaxation rate enhancement in case of PVP-360 which is consistent with the PVP-40 adsorption study with core-shell particles. This result is well matched with the agreement of Cooper et al. where it was stated that relaxation rate is not dependent on the polymer of different molecular weight at same concentration [27].

Figure-3.18 illustrates the light scattering and NMR measurement of PVP adsorption on silica-titania hollow nanoparticles. Although there is also no significant effect observed on R_{2SP} change upon PVP adsorption but a slight increase in R_{2SP} rather than core-shell structure can be seen (around 0.02-0.1 R_{2SP} value, over the range of PVP adsorption studied). This slight change could result from very little adsorption of PVP. From the analysis of STCSNP and STHNP shell chemistry, it has been confirmed that STCSNP has pure titania on the surface.

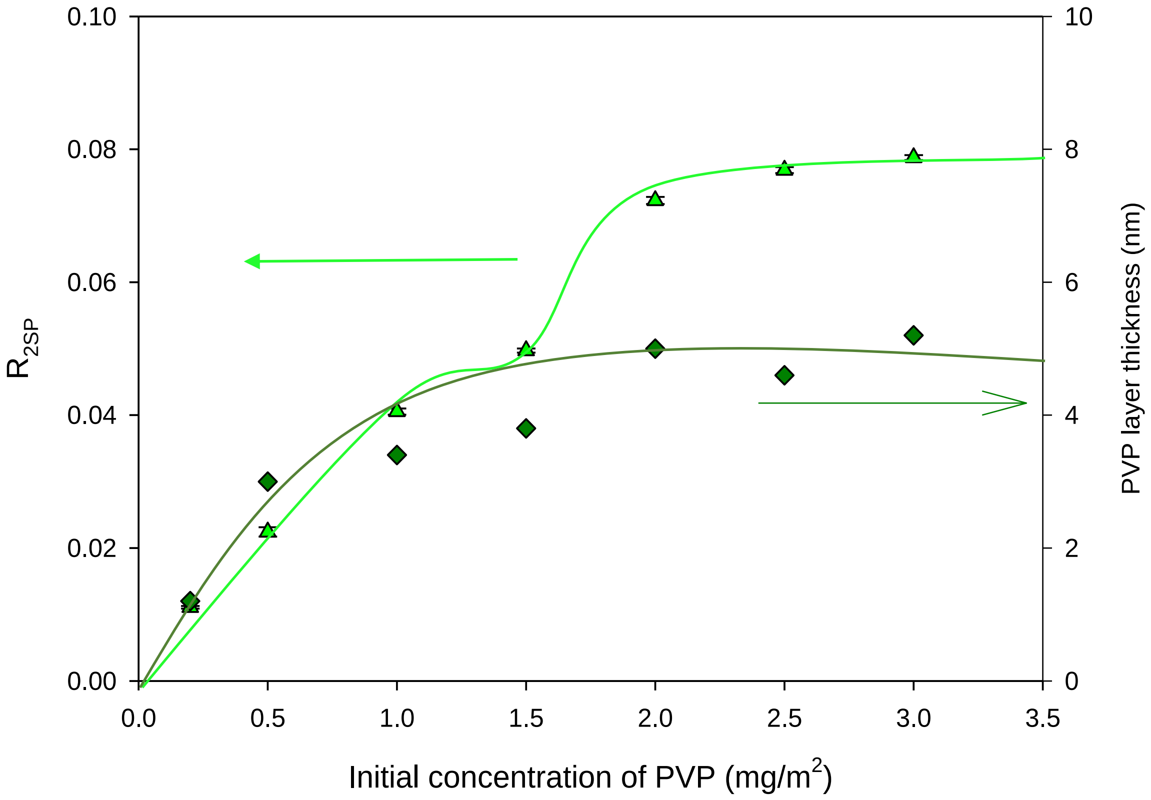

Figure 3. 18: Adsorption of PVP-40 on STHNP measured by relaxation NMR (▲) (only sensitive to near surface train layer) and layer thickness (◆) (sensitive to the entire polymer-particles system) on right axis measured by light scattering technique. Lines are a guide to the eye.

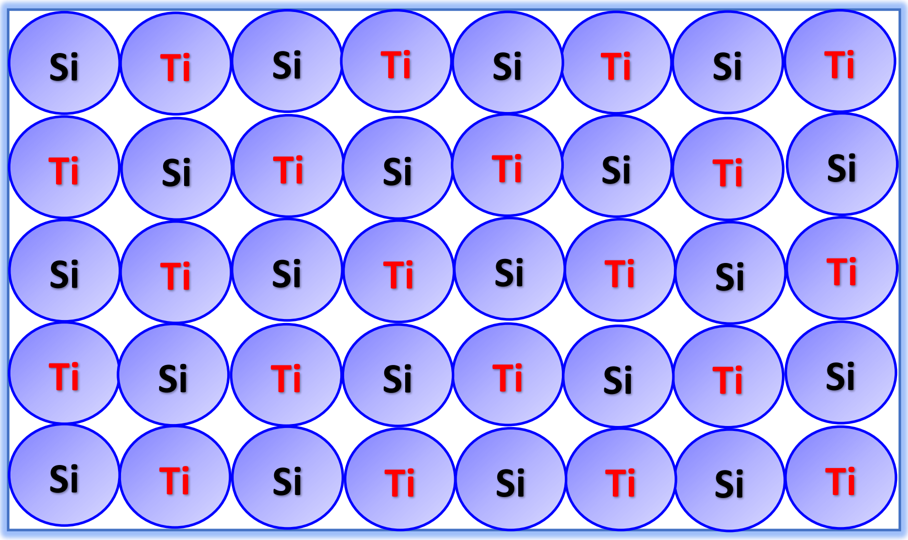

Figure 3. 19: Schematic representation of shell chemistry of hollow nanoparticles.

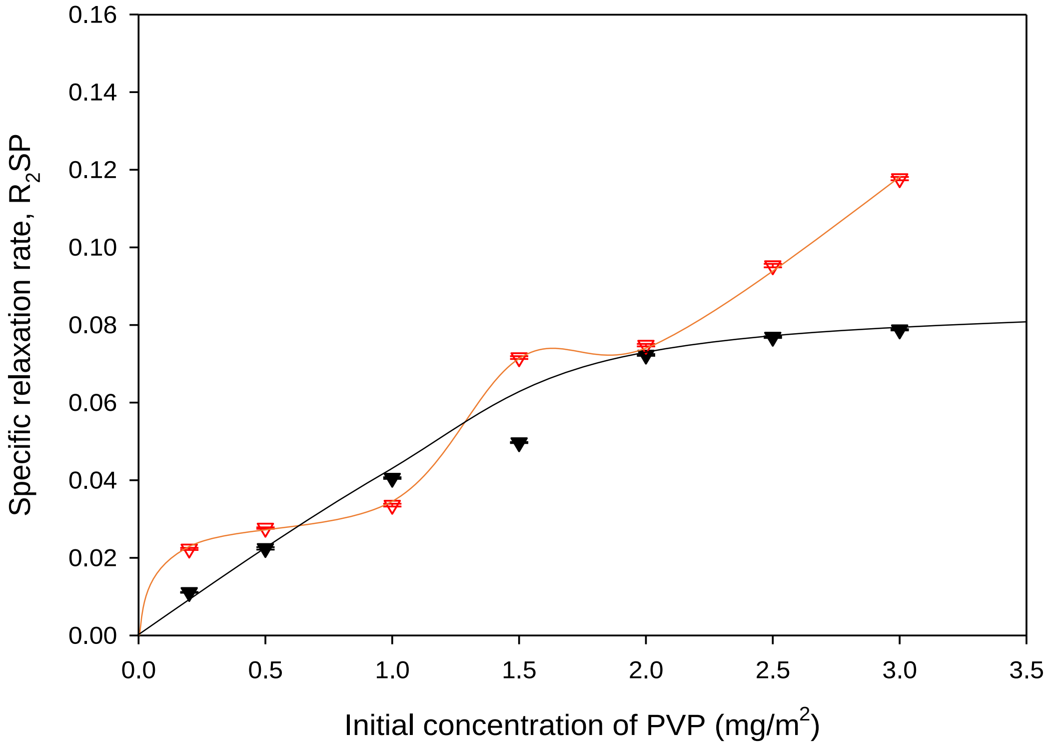

Figure 3. 20: Comparison of PVP-40 (▼) and PVP-360 (▽) adsorption on STHNP surface. R2SP was normalized with STHNP concentration. Lines are a guide to the eye.

On the other hand, STHNP has little bit complex chemistry of silica and titania on the outer surface (Figure-3.19). During hollow nanoparticles formation, completely etched core silica and partially etched titania shell released into the solution under the experimental condition. Here titania was not etched that much due to its chemical stability. These etched species (mostly etched silica) then re-deposited on titania shell through condensation reaction to form the mixed silica-titania shell at the outer surface of the hollow nanostructure (suggested by STEM-EDX data). This etching and re-deposition process is continued until the formation of a hollow cavity. So, it could be assumed that the slight increase in R_{2SP} compares to core-shell particles may be resulted from little adsorption of PVP on silica at the mixed shell of a hollow cavity or there is no PVP adsorption at all since titania species is dominating on the shell surface with its quadrupole nuclei. Figure-3.20 also shows the very negligible change in R_{2SP} upon high molecular weight PVP-360 adsorption. This negligible effect was expected since R_{2SP} is independent of the molecular weight of the same polymer.

3.6 Conclusion

There has been an extensive use of solvent relaxation NMR for studying a variety of colloidal particles in liquids. Here this technique was used to study the bare silica nanoparticle, STCSNP (core-shell nanoparticles) with compact titania shell and STHNP (hollow nanoparticles) with hollow cavity covered by the mixed silica-titania shell. Relaxation rates for these three different nanostructures were measured. STCSNP and STHNP surfaces had a stronger impact on the solvent relaxation compared to silica due to the presence of quadrupole nuclei on the surface of STCSNP and STHNP. The NMR data were also plotted as the function of surface area of three different particles and relaxation enhancement in term of surface area was compared. The most interesting relaxation data were found from the hollow nanoparticles at low concentrations where two relaxation rates from the inner and outer surfaces were calculated from double exponential decay. That means it could be possible to calculate the porosity of the complex structure like porous and hollow. Although porosity of porous carbon nanostructures has already been studied recently, here the particle with a hollow cavity has been studied for the first time by solvent relaxation.

Polymer adsorption on these three different nanostructures was also investigated by relaxation NMR. Although adsorption of polymer on silica nanoparticles have extensively detailed in literature, the non-adsorption of PVP onto titania and silica-titania mixed surfaces has been confirmed by solvent relaxation here for the first time. These data could be valuable for further polymer and polymer-surfactant study on mixed silica-titania interfaces.

Bibliography

[1] S. K. Misra, F. Ostadhossein, E. Daza, E. V. Johnson and D. Pan, "Hyperspectral Imaging Offers Visual and Quantitative Evidence of Drug Release from Zwitterionic-Phospholipid-Nanocarbon When Concurrently Tracked in 3D Intracellular Space," *Adv. Funct. Mater,* vol. 26, p. 8031–8041, 2016.

[2] D. Ren, "Protein Nanoparticle as a Versatile Drug Delivery System in Nanotechnology," *J Nanomed Res ,* vol. 4, p. 1, 2016.

[3] Y. Yang and C. Yu, "Advances in silica based nanoparticles for targeted cancer therapy.," *Nanomedicine,* vol. 12, no. 2, p. 317–332, 2016.

[4] X. She, L. Chen, Z. Yi, C. Li, C. He, C. Feng, T. Wang, S. Shigdar, W. Duan and L. Kong, "Tailored Mesoporous Silica Nanoparticles for Controlled Drug Delivery: Platform Fabrication, Targeted Delivery, and Computational Design and Analysis," *Mini Rev Med Chem.,* vol. 16, no. 18, pp. 1-14, 2016.

[5] T. Cosgrove, Colloid Science: Principles, Methods and Applications, 2nd Edition, New Jersey: Wiley-Blackwell, 2010.

[6] D. Fairhurst, T. Cosgrove and W. S. Prescott, "Relaxation NMR as a tool to study the dispersion and formulation behavior of nanostructured carbon materials," *Magn. Reson. Chem. ,* vol. 54, p. 521–526, 2016.

[7] T. Cosgrove, K. S. Jack, N. Green, T. M. Obey and M. Wood, "NMR Solvent Relaxation Studies on Concentrated Particulate Dispersions," *ACS Symposium Series, Supramolecular Structure in Confined Geometries, Chapter 10,* vol. 736, pp. 153-168, 1999.

[8] C. L. Cooper, T. Cosgrove, J. S. v. Duijneveldt, M. Murray and S. W. Prescott, "Colloidal Particles in Competition for Stabilizer: A Solvent Relaxation NMR Study of Polymer Adsorption and Desorption," *Langmuir,* vol. 28, p. 16588−16595, 2012.

[9] T. Cosgrove and K. Ryan, "N.m.r. relaxation studies on poly(ethylene oxide) terminally attached at the polystyrene/water interface," *J. Chem. Soc., Chem. Commun.,* pp. 1424-1426, 1988.

[10] T. Cosgrove, C. Roberts, T. Garasanin, R. G. Schmidt and G. V. Gordon, "NMR Spin-Spin Relaxation Studies of Silicate-Filled Low Molecular Weight Poly(dimethylsiloxane)s," *Langmuir ,* vol. 18, pp. 10080-10085, 2002.

[11] B. Cattoz, T. Cosgrove, M. Crossman and S. W. Prescott, "Surfactant-Mediated Desorption of Polymer from the Nanoparticle Interface," *Langmuir,* vol. 28, p. 2485−2492, 2012.

[12] P. C. Griffiths, A. Y. F. Cheung, J. A. Davies, A. Paul, C. N. Tipples and A. L. Winnington, "Probing interactions within complex colloidal systems using PGSE-NMR," *Magn. Reson. Chem.,* vol. 40, p. S40–S50, 2002.

[13] T. Cosgrove and P. C. Griffiths, "Nuclear magnetic resonance studies of adsorbed polymer layers," *Advances in Colloid and Interface Science,* vol. 42, pp. 175-204 , 1992.

[14] A. Nelson, K. S. Jack, T. Cosgrove and D. Kozak, "NMR Solvent Relaxation in Studies of Multicomponent Polymer Adsorption," *Langmuir,* vol. 18, no. 7, p. 2751, 2002.

[15] D. HIGGINS, "ReviseMRI.com," 2003-2017. [Online]. Available: http://www.revisemri.com/questions/creating_an_image/rf_pulse. [Accessed 20 01 2017].

[16] M. Leskes and C. P. Grey, "Finite pulse effects in CPMG pulse trains on paramagnetic materials," *Phys. Chem. Chem. Phys.,* vol. 17, pp. 22311--22320, 2015.

[17] E. L. Hahn, "Spin Echoes," *Phys. Rev,* vol. 80, pp. 580-594, 1950.

[18] H. Y. Carr and E. M. Purcell, "Effects of Diffusion on Free Precession in Nuclear Magnetic Resonance Experiments," *Phys. Rev.,* vol. 94, pp. 630-643, 1954.

[19] S. Meiboom and D. Gill, "Modified Spin-Echo Method for Measuring Nuclear Relaxation Times," *Rev. Sci. Instrum.,* vol. 29, p. 688−691, 1958.

[20] G. P. van der Beek, M. A. Cohen Stuart and T. Cosgrove, "Polymer Adsorption and Desorption Studies via lH NMR Relaxation of the Solvent," *Langmuir,* vol. 7, pp. 321-334, 1991.

[21] A. NARATH, "Nuclear Spin-Lattice Relaxation in Hexagonal Transition Metals: Titanium," *Physical Review,* vol. 162, no. 2, pp. 320-332, 1967.

[22] H. J. Osten and J. C. Jameson, "Quadrupolar spin relaxation due to electric field gradients induced by vibrations and collisions," *Molecular Physics,* vol. 57, no. 3, pp. 553-571, 1986.

[23] A. Nelson and T. Cosgrove, "Dynamic Light Scattering Studies of Poly(ethylene oxide) Adsorbed on Laponite: Layer Conformation and Its Effect on Particle Stability," *Langmuir ,* vol. 20, pp. 10382-10388, 2004.

[24] T. Cosgrove, P. C. Grifiths and P. M. Lloyd, "Polymer Adsorption. The Effect of the Relative Sizes of Polymer and Particle," *Langmuir,* vol. 11, pp. 1457-1463, 1995.

[25] C. MA, "Adsorption from Mixed Solutions of Poly(vinyl pyrrolidone) and Sodium Dodecyl Sulfate on Titanium Dioxide," *Colloids and Surfaces,* vol. 16, pp. 185-191, 1985.

[26] M. Pattanaik and S. K. Bhaumik, "Adsorption behaviour of polyvinyl pyrrolidone on oxide surfaces," *Materials Letters ,* vol. 44, p. 352–360, 2000.

[27] C. L. Cooper, T. Cosgrove, J. S. v. Duijneveldt, M. Murray and S. W. Prescott, "Competition between Polymers for Adsorption on Silica: A Solvent Relaxation NMR and Small-Angle Neutron Scattering Study," *Langmuir,* vol. 29, no. 41, p. 12670–12678, 2013.

Chapter-4

Conclusion and recommendation for future work

4.1 Conclusion

The nanoparticles used here in this project, with their size, structure and different surface chemistry, provide very convenient systems on which different characterization methods can be thoroughly tested. And, the possibility of hollow nanoparticles as a drug delivery system, due to the hollow cavity and porous shell, was also studied.

Initial experiments were focused on the synthesis of monodispersed hollow nanoparticles. The SMER method (Sonication Mediated Etching and Re-deposition) was used for hollowing the core-shell nanoparticles. Titania was used here for its inert chemical stability to form a compact shell during the hollowing process which was finally turned into a mixed shell of silica-titania (around 50:50) after sonication. This results in a highly porous shell with well-defined mesopores (around 5nm), where drug dissolution within the hollow cavity is likely useful for drug delivery applications. Nitrogen physisorption data revealed the large surface area (295 m^2/gm) and specific volume (0.39) for hollow nanoparticles which offer more volume for therapeutic loading compared to the bare nanoparticles at the same concentration.

The work then focused on the NMR relaxation experiments of silica, STCSNP, and STHNP where water relaxation in the three different nanoparticles was observed. The titania surfaces of STCSNP and mixed silica-titania surfaces of STHNP show higher R_{2SP} enhancement compared with the bare silica surfaces. This high relaxivity of water on pure titania and silica-titania mixed surfaces was likely due to the presence of the quadrupole nuclei of titanium and the high surface area of core-shell and hollow nanoparticles. For the hollow nanoparticles, two different relaxation rates were observed likely from the inner cavity and outer shell surface.

Exposing PVP to the three different structured nanomaterials revealed no significant adsorption on the titania surfaces (STCSNP and STHNP) but did so for the silica ones. For the silica surfaces, solvent relaxation and dynamic light scattering techniques were used to understand the polymer adsorption. Relaxation NMR was sensitive to train conformation of polymer adsorbed on the particle surfaces. Further polymer addition started to form loops and tails conformation on the particle surfaces and the total hydrodynamic thickness was measured by the light scattering technique. For silica, the saturation point of PVP adsorption was found around at 1.5 mg/m^2 of PVP amount added. On the other hand, there was no significant polymer adsorption observed on the titania and mixed silica-titania surfaces, however, the slight change on R_{2SP} was observed in the case of mixed surfaces (hollow nanoparticles) compare to the pure titania surfaces (core-shell nanoparticles). This may be due to the presence of silica on the mixed silica-titania shell of hollow nanoparticles.

4.2 Future work

The work in this thesis was based on the hypothesis of finding a quick and thorough characterisation technique for hollow nanoparticles to understand their potential as a drug delivery system. These experiments have opened up the possibility of measuring the porosity of hollow nanoparticles by NMR spectroscopy, which could be further extended to the point where it is possible to compare or contrast the porosity data with traditional porosity measurement techniques (nitrogen physisorption, neutron scattering). Future work can include further NMR investigation of hollow nanoparticles at higher particle concentration to see if the two relaxation rates will be observed, as a function of the mole ratio of mixed silica-titania shell surfaces forming the hollow nanoparticles. Additionally, the research could be extended to the adsorption of different polymers, to investigate the effect of surfactant on polymer adsorption for the non-adsorbing surfaces of STCSNP and STHNP.